UNIVERSITY OF CALIFORNIA, SAN DIEGO

Diffusion, trapping, and isotope exchange of plasma implanted deuterium in ion beam damaged tungsten

A dissertation submitted in partial satisfaction of the requirements for the degree

Doctor of Philosophy

in

Engineering Sciences (Engineering Physics)

by

Joseph Lincoln Barton

Committee in charge:

Professor George R. Tynan, Chair
Professor Farhat N. Beg
Professor Nasr M. Ghoniem
Professor Vitali F. Nesterenko
Professor Kevin B. Quest

2016

The Dissertation of Joseph Lincoln Barton is approved, and it is acceptable in quality and form for publication on microfilm and electronically:

_____

_____

_____

_____

_____

Chair

University of California, San Diego

2016

Dedication

To my wife Ryan and my son Jack

Table of Contents

List of Figures

List of Tables

Acknowledgements

As I approach this pinnacle of academic achievement, I would like to acknowledge and thank those who have helped me reach this goal. First and foremost, my academic advisor George Tynan could not be a better advisor. His creative inputs, insightful discussions, and thoughtful criticisms of my work helped me become a better scientist, and he will continue to be a role model for me to aspire. After these years of graduate study under his advisory, I feel I am now well prepared to contribute to mankind's quest for scientific truth.

My "unofficial" advisor, Russ Doerner, deserves much acclaim for his contributions to my research. His knowledge and physical intuitions on plasma-material interactions illuminated aspects of this field that are complex and interesting, which ultimately inspired me to pursue this work. He was often available to offer an invaluable sanity check to any of my unorthodox research questions and debate the cause of seemingly odd results from experiments.

The PISCES staff provided much needed support throughout the years. Learning how to operate and troubleshoot the complex plasma devices in the PISCES lab would have been impossible without the help of Matt Baldwin. If there was ever any questions I had concerning diagnostic calibrations, measurement procedures, or general lab operations, then Ray Seraydarian was my guy. He is a walking encyclopedia of physics diagnostics. Karl Umstadter, while our paths only temporarily crossed, delegated some educational engineering projects to me that

widened my experimental repertoire using lasers to simulate transient heat effects on materials that are simultaneously exposed to plasma. Timo Dittmar's meticulous approach to experiments showed me how a true professional operates. His systematic procedures for even the most seemingly unimportant tasks are copied in my lab book and are often referenced. Discussions with Timo about the thermal desorption spectroscopy diagnostic was also very useful in my research. In a very realistic sense, the isotope exchange project would not have existed without insight from Thomas Schwarz-Selinger, although he was technically a collaborator from the Max Plank Institute for Plasma Physics. These isotope exchange experiments were initially his idea, and I want to thank him for allowing me to pursue this project independently.

The unsung heros of our lab are the technical staff. Tyler Lynch was always available to help me in the machine shop to polish samples or to teach me how to manufacture parts or tools needed in my experiments. Leo Chousal was a valuable resource for troubleshooting equipment failures. Rollie Hernandez's expertise has helped me solve problems with the lab's various electronics on a number of occasions, and as a result, has improved my knowledge on the subject.

Our collaboration with Los Alamos National Laboratory was an integral part of my research. Yongqiang Wang provided a unique education on the operation of ion accelerators and assisted with all ion beam experiments in this work. I am greatful for the effort and attentiveness he put into this research and for his hospitality during my visits to Los Alamos. Joe Tesmer is a leading ion beam experimentalist, who has long since retired, but is still very active in the lab. That, in itself, was an inspriation to me. Joe was also happy to answer questions and gave me a deeper understanding of ion beam physics that was invaluable.

The administrative staff in the CER, MAE and at LANL were very helpful

and kind. Sandy Rosas, Brandi Pate, and Sandra de Sousa I would like to thank in particular for handling the traveling reimbursements and other finances. I would like to acknowledge Linda McKamey and Lydia Ramirez for making my graduate experience run smoothly, helping me handle all of the deadlines and administrative checks with ease. The staff at LANL, primarily Esther Palluck, were very hospitable and helpful, making travel to Los Alamos a breeze.

My peers have been a great sounding board for my research ideas and provided much needed moral support during my years as a graduate student. Jordan Gosselin was not only my office-mate but also a close friend. Our conversations in the office led to many thoughtful and productive discussions about our research projects, which were distinctly different, and about science in general. I will dearly miss these conversations after our careers move forward. David Eldon is also a close friend of mine that not only challenged my intelect but also showed me that it is possible juggle being a new father and be a successful graduate student simultaneously. Mike Simmonds has recently joined our research group focusing on radiation damaged materials and has been an excellent peer, providing creative and critical insights to my research and this work in general. Davis Brigman has not directly influenced this project but has been a peer of mine since high school. He has provided much needed ecouragement and motivation to finish my degree.

I would like to finally thank my family for all the support they have provided me. My wife, first of all, is the greatest person on this planet. I wanted to pursue my professional career on the west coast of this continent, but she had commitments on the east coast. Without encouragement from her to chase my dream this would not have been possible, and happily, she was able to join me in these final years. Of course, my parents have been a constant pillar of support. Their love and patience could not be acknowledged enough.

Chapter 4, including text and data, is in part a reprint of the material as it appears in J. L. Barton, Y. Q. Wang, T. Schwarz-Selinger, R. P. Doerner, G. R. Tynan, Isotope exchange experiments in tungsten with sequential deuterium and protium plasmas in pisces, J. Nucl. Mater. 438 (2013) S1183-S1186. The dissertation author was the primary investigator and author of this paper.

Chapter 5, including text and data, is a reprint of the material as it appears in J. L. Barton, Y. Q.Wang, T. Dittmar, R. P. Doerner, G. R. Tynan, Deuterium retention in tungsten after heavy ion damage and hydrogen isotope exchange in pisces, Nucl. Instrum. Methods Phys. Res., Sect. B 332 (2014) 275279. The dissertation author was the primary investigator and author of this paper.

Chapter 6, including text and data, is a reprint of the material as it appears in J. L. Barton, Y. Q.Wang, R. P. Doerner, G. R. Tynan, Development of an analytical diffusion model for modeling hydrogen isotope exchange, J. Nucl. Mater. 463 (2015) 1129-1133. The dissertation author was the primary investigator and author of this paper.

Chapter 7, including text and data, has been submitted to Nuclear Fusion for publication. The authors are J. L. Barton, Y. Q.Wang, R. P. Doerner, and G. R. Tynan. The dissertation author was the primary investigator and author of this paper.

Vita

2016	Ph.D., Engineering Physics, University of California, San Diego
2009-2016	Graduate Student Researcher, Center for Energy Research, University of California, San Diego
2011	Teaching Assistant, Department of Mechanical and Aerospace Engineering, University of California, San Diego
2011	M.S., Engineering Physics, University of California, San Diego
2009	B.S., Physics, North Carolina State University

PUBLICATIONS

J. L. Barton, Y. Q. Wang, R. P. Doerner, G. R. Tynan, Plasma implanted hydrogenic diffusion and trapping in ion beam damaged tungsten, submitted (March 2016) to Nuclear Fusion

J. L. Barton, Y. Q. Wang, R. P. Doerner, G. R. Tynan, Development of an analytical diffusion model for modeling hydrogen isotope exchange, J. Nucl. Mater. 463 (2015) 1129-1133

E. Dechaumphai, J. L. Barton, J. R. Tesmer, J. Moona, Y. Q. Wang, G. R. Tynan, R. P. Doerner, R. Chen, Near-surface thermal characterization of plasma facing components using the 3-omega method, J. Nucl. Mater. 455 (2014) 5660

J. L. Barton, Y. Q. Wang, T. Dittmar, R. P. Doerner, G. R. Tynan, Deuterium retention in tungsten after heavy ion damage and hydrogen isotope exchange in pisces, Nucl. Instrum. Methods Phys. Res., Sect. B 332 (2014) 275279

J. L. Barton, Y. Q. Wang, T. Schwarz-Selinger, R. P. Doerner, G. R. Tynan, Isotope exchange experiments in tungsten with sequential deuterium and protium plasmas in pisces, J. Nucl. Mater. 438 (2013) S1183-S1186

FIELDS OF STUDY

Major field: Engineering Sciences (Engineering Physics)

Studies in Nuclear Fusion: Plasma-Material Interactions
Professor George R. Tynan

ABSTRACT OF THE DISSERTATION

Diffusion, trapping, and isotope exchange of plasma implanted deuterium in ion beam damaged tungsten

by

Joseph Lincoln Barton

Doctor of Philosophy in Engineering Sciences (Engineering Physics)

University of California, San Diego, 2016

Professor George R. Tynan, Chair

Tritium accumulation in nuclear fusion reactor materials is a major concern for practical and safe fusion energy. This work examines hydrogen isotope exchange as a tritium removal technique, analyzes the effects of neutron damage using high energy copper ion beams, and introduces a diffusion coefficient that is a function of the concentration of trapped atoms.

Tungsten samples were irradiated with high energy (0.5 - 5 MeV) copper ions for controlled levels of damage - 10^{-3} to 10^{-1} displacements per atom (dpa) - at room temperature. Samples were then exposed to deuterium plasma at constant temperature ($\sim$380 K) to a high fluence of $\geq 10^{24}$ ions/m^2, where retention is at is maximized (i.e. saturated). By then subsequently exposing these samples to fractions of this fluence with hydrogen plasma, isotope exchange rates were observed. The resulting deuterium still trapped in the tungsten is then measured *post mortem*. Nuclear reaction analysis (NRA) gives the depth resolved deuterium retention profile with the ^{3}He(D,p)^{4}He reaction, and thermal desorption spectroscopy (TDS) gives the total amount of deuterium trapped in the tungsten by heating a

sample in vacuum up to 1200 K and measuring the evaporated gas molecules with a residual gas analyzer.

Isotope exchange data show that hydrogen atoms can displace trapped deuterium atoms efficiently only up to the first few microns, but does not affect the atoms trapped at greater depths. In ion damaged tungsten, measurements showed a significant increase in retention in the damage region $\propto \text{dpa}^{0.66}$, which results in a significant spike in total retention, and isotope exchange in damaged samples is still ineffective at depths greater than a few microns. Thus, isotope exchange is not an affective tritium removal technique; however, these experiments have shown that trapping in material defects greatly affects diffusion.

These experiments lead to a simplified diffusion model with defect densities as the only free parameter. After examining the rate limiting processes, it is observed that trapped and solute atoms reach equilibrium concentrations before atoms diffuse further. This ultimately leads to the derivation of a diffusion coefficient that has a non-linear dependence on the concentration of trapped atoms, and this new coefficient can resolve discrepancies of diffusivity measurements in the literature.

Chapter 1

Introduction

1.1 Nuclear fusion as an energy source

One of the most abundant sources of energy in our universe comes from nuclear fusion, and harnessing its power would solve many of mankind's energy concerns. Nuclear fusion occurs in the core of stars where atomic nuclei are under so much pressure and heat that they can fuse together. The energy released from fusion keeps stars shining bright for billions of years. Comparing our current energy sources to the energy produced by the sun, they are neither as long-lasting nor as reliable.

Since the dawn of the Industrial Age, producing energy in large quantities has been of critical importance to sustaining our ever growing population and economy. Burning oil, coal, and natural gas have historically been the most reliable forms of energy. Unfortunately these energy resources may soon no longer be available. The proven fossil fuel reserves at current consumption rates will last about 50 years for oil, 55 years for natural gas, and 110 years for coal [1]. One alternative to burning fossil fuels is renewables, such as solar and wind power, and have been gaining in popularity. Although these sources are effectively inex-

haustible and supplement traditional power plants, they are intermittent due to weather conditions and often inaccessible by many populated regions on the globe. Another alternative is nuclear fission, which is a reliable and long-lasting energy source, but political and social concerns due to nuclear weapon proliferation and population safety have prevented fission from being more widely adopted.

Nuclear fusion as an energy source has none of the shortcomings of other energy sources and has other benefitial side-effects. The main ingredient of fusion - an isotope of hydrogen called deuterium - can be found in seawater, so fusion is essentially an inexaustible resource. This will end humanity's dependence on fossil fuels, and as a consquence, will reduce political conflicts over energy. An "unlimited" energy source can allow an increase in desalination plants, providing drinkable water to all coastal populations. The fusion of hydrogen isotopes produce no atmospheric pollutants. A catastrophic event to the reactor would not permanently damage the surrounding environment. Fusion products cannot be proliferated and turned into weapons. Power plants do not have geographical limitations and are not effected by the weather. Therefore fusion energy is convenient, safe for the environment, and virtually unlimited. If fusion energy technology is obtained, then humanity's energy needs can be met for the forseeable future.

In this chapter, the basic technologies of nuclear fusion and its current challenges are summarized. Since magnetically confined fusion is the most promising and more developed reactor design to date, discussion will be limited to only the Magnetic Fusion Experiment (MFE) concept. There are a few engineering hurdles that will be summarized, but among the many challenges needed to achieve a working reactor, the issues raised by plasma-material interactions (PMI) will be emphasized because it is the focus of this dissertation.

1.2 Controlled fusion reactor environment

Nuclear fusion occurs when the nuclei of two atoms are close enough so that they overcome Coloumb repulsion and the nuclear strong force fuses them together to form a heavier nucleus. This newly formed nucleus is in an excited state and is unstable; therefore, the nucleus decays into a energetically stable state, transfering its stored energy to the reaction products. The energy of the reaction products is proportional to the rest mass energy defined by Einstein in his famous equation $E = mc^2$. Energy from a fusion reactor will be a result of the following fusion reactions due to their large collision cross-sections [2]

$$ {}^{2}_{1}\mathrm{D} + {}^{3}_{1}\mathrm{T} \rightarrow {}^{4}_{2}\mathrm{He}(3.5\ \mathrm{MeV}) + \mathrm{n}^{0}(14.1\ \mathrm{MeV}) \tag{1.1} $$

$$ {}^{2}_{1}\mathrm{D} + {}^{2}_{1}\mathrm{D} \rightarrow {}^{3}_{1}\mathrm{T}(1.01\ \mathrm{MeV}) + \mathrm{p}^{+}(3.02\ \mathrm{MeV}) \tag{1.2} $$

$$ {}^{2}_{1}\mathrm{D} + {}^{2}_{1}\mathrm{D} \rightarrow {}^{3}_{2}\mathrm{He}(0.82\ \mathrm{MeV}) + \mathrm{n}^{0}(2.45\ \mathrm{MeV}) \tag{1.3} $$

$$ {}^{2}_{1}\mathrm{D} + {}^{3}_{2}\mathrm{He} \rightarrow {}^{4}_{2}\mathrm{He}(3.6\ \mathrm{MeV}) + \mathrm{p}^{+}(14.7\ \mathrm{MeV}) \tag{1.4} $$

Equation (1.1) is the most promising fusion reaction for energy production has been demonstrated by experiments in the U.S. [3] and in Europe [4] by magnetically confining a hot, dense plasma made up of deuterium (D) and tritium (T). The reaction in (1.1) produces an energetic 14.1 MeV neutron, and a future power plant will harness this energy into steam to turn turbines and generate electricity.

In order for fusion reactions to occur with sufficient reliability, the plasma ions must have a sufficient density n, have a very high temperature T, and be confined long enough for reactions to occur τ_{E} (i.e. the energy confinement time). In a D-T plasma for the reaction (1.1), sufficient values for these parameters must

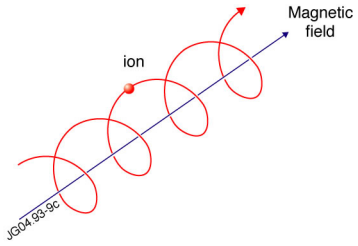

Figure 1.1: An ideal case of a single ion confined in a uniform magnetic field without an applied electric field [7].

satisfy the triple product [5]

$$nT\tau_{\mathrm{E}} \geq 3 \times 10^{21} \text{ keV s/m}^3, \tag{1.5}$$

based on the work done by Lawson [6]. Energy confinement time is defined by how quickly the system loses energy to its surroundings. Typically τ_{E} is quantified by the ratio of the total stored energy of the system W to the energy loss rate P_{loss}: $\tau_{\mathrm{E}} = {}^{W}/_{P_{\mathrm{loss}}}$. For reference, the minimum plasma temperature required for continuous self-heating (i.e. reactions providing energy to the plasma) in a D-T plasma is over 10 keV (100 million degrees C), and realistic plasma densities are above 10^{19} m^{-3}. Thus confinement times need to be on the order of 10 seconds or higher. At any rate, experimental reactors study the physics that will allow satisfaction of this criterion to produce energy from fusion.

The way charged particles are confined by magnetic fields can be seen in figure 1.1. The ion has an orbit perpendicular to the field direction and is confined; however, the ion is not confined in the directions parallel to the field. This can be seen in a simplified equation of motion for a particle with mass m, charge q, and velociy $\vec{v}$ balanced by the Lorentz force in a uniform magnetic field $\vec{B} = B\hat{z}$ and no electric field

$$m\frac{d\vec{v}}{dt} = q\vec{v} \times \vec{B}. \tag{1.6}$$

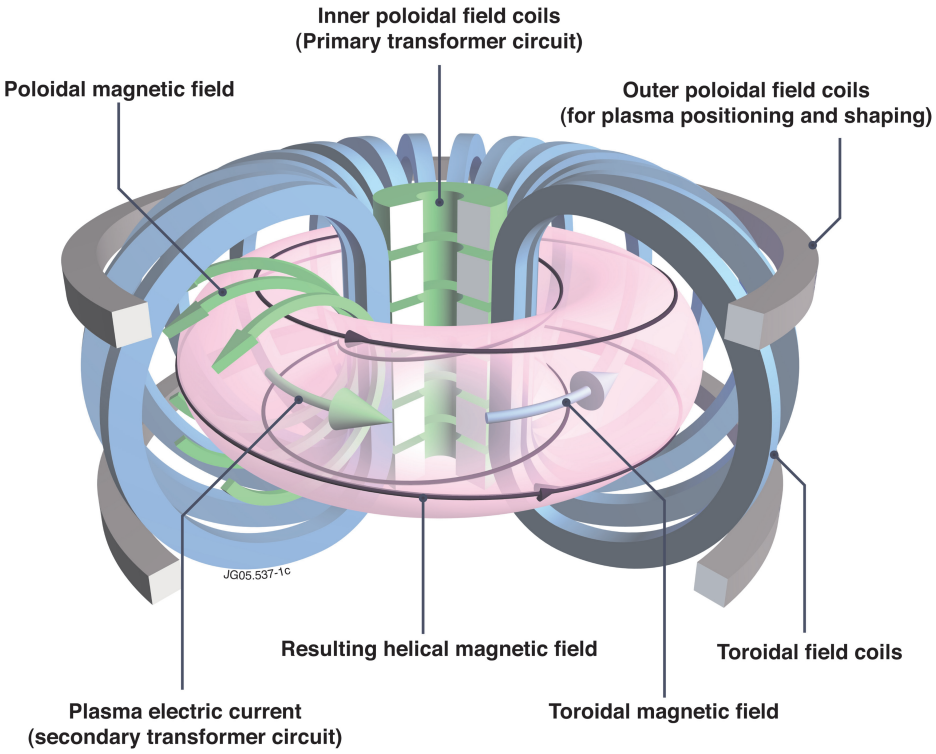

Figure 1.2: Principle schematic of magnetic field geometry in a tokamak with the magnetic field directions indicated by the arrows [7].

The nonzero components of the force are in the x and y directions, confining the velocity to orbit around the field lines at the cyclotron frequency

$$\omega_c = \frac{|q|B}{m}. \tag{1.7}$$

However in the $\hat{z}$ direction, the particle is not confined. In order to confine the plasma parallel to the magnetic field, the field lines are bent around in a torroidal shape so that they close on themselves.

The most highly developed and most promising technique for using magnetic fields to confine plasma is in a machine called a tokamak [8]. Figure 1.2 is a schematic of the field line geometry of a tokamak. The toroidal field coils produce the magnetic fields that close along the toroidal axis (round blue arrow), and the

poloidal field coils along with the plasma current produce the magnetic fields that close along the poloidal direction (flat green arrows). However, there is only a finite radius where the poloidal field lines are closed, and the open field lines have to intersect the vacuum vessel materials. In large MFE experiments, open field lines are directed to a region in the tokamak called the divertor by the poloidal field coils. To get a more realistic picture of what a tokamak looks like, figure 1.3(a) is a cut-away of the flagship tokamak device, ITER, that is being built in Cadarache, France, and the divertor is at the bottom of the poloidal cross-section of the ITER vacuum chamber 1.3(b). Figure 1.4 is a poloidal cross-section of a tokamak that illustrates these field lines, called "magnetic flux surfaces". The last closed flux surface (LCFS) defines the boundary, called the separatrix, between the core plasma and the plasma along open field lines, called the scrape-off layer (SOL). Although it may seem from equation (1.6) that closed magnetic field lines may be enough to confine the core plasma, the reality is that the SOL is continuously supplied by particles from the plasma core that drift perpendicular to these field lines. Plasma in the SOL will either be guided to the divertor along the field lines or will diffuse out to the first wall [9]. In either case, plasma will interact with solid materials.

The physics that allow core plasma to drift out into the SOL can be seen by examining other forces in the system. There are velocity components perpendicular to the magnetic field, even when the field is straight and uniform. The fluid momentum equation of a plasma species with mass m, number density n, charge q, and velociy $\vec{v}$ is

$$mn\frac{d\vec{v}}{dt} = qn\left(\vec{E} + \vec{v} \times \vec{B}\right) - \nabla p, \tag{1.8}$$

where the plasma feels forces from the Lorentz force with electric field $\vec{E}$ and magnetic field $\vec{B}$ and a pressure gradient ∇p. To show the component of velocity

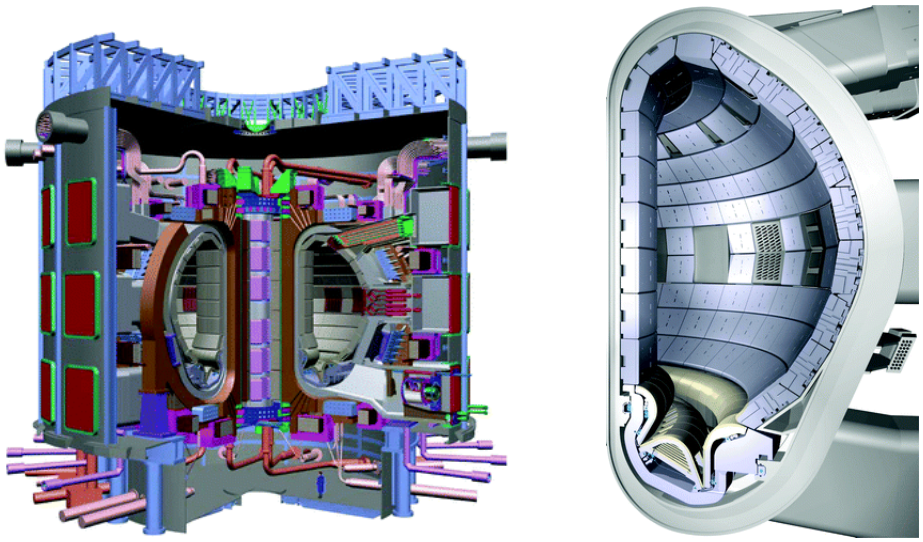

(a) (b)

Figure 1.3: Drawing of the flagship fusion test reactor ITER (a) and a corresponding poloidal cross-section of the vacuum chamber (b), illustrating the plasma facing walls and divertor [10].

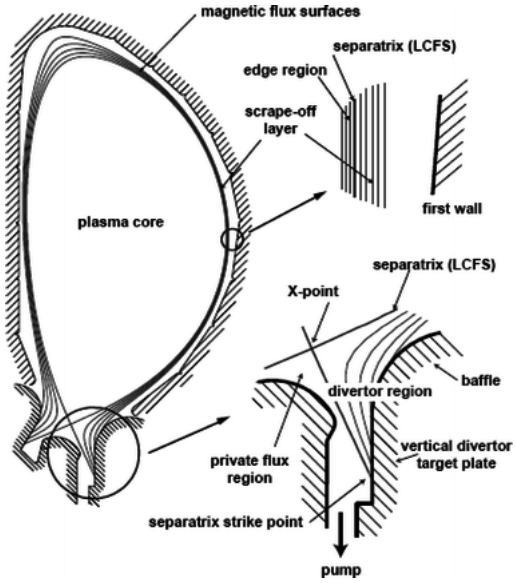

Figure 1.4: Poloidal cross-section of a typical tokamak, illustrating the open magnetic field lines in the scrape-off layer (SOL) region [11].

perpendicular to the magnetic field, let us cross (1.8) with $\vec{B}$ and solve for the component $\vec{v}_\perp$

$$\vec{v}_\perp = \frac{\vec{E}\times\vec{B}}{B^2} - \frac{\nabla p\times\vec{B}}{qnB^2} \pm \frac{1}{\omega_c B}\frac{d\vec{v}_\perp}{dt}\times\vec{B}, \tag{1.9}$$

where $\vec{v}_\perp$ is defined as the drift velocity perpendicular to the magnetic field and the $\pm$ is for either a postive or negative charge, respectivly. In tokamaks, the first term on the right hand side of is dominant [5], so that $\frac{d\vec{v}_\perp}{dt} \approx \frac{d}{dt}\left(\frac{\vec{E}\times\vec{B}}{B^2}\right)$. Substituting in for $\frac{d\vec{v}_\perp}{dt}$ in equation (1.9), assuming $\vec{B}$ does not vary in time, we obtain

$$\vec{v}_\perp = \frac{\vec{E}\times\vec{B}}{B^2} - \frac{\nabla p\times\vec{B}}{qnB^2} \pm \frac{1}{\omega_c B}\frac{d\vec{E}_\perp}{dt}, \tag{1.10}$$

where $\vec{E}_\perp$ is the electric field perpendicular to $\vec{B}$. The first term is a drift velocity arising from the existance of an electric field and is independent of charge and mass. The second term, called the diamagnetic drift, is a fluid velicity showing that when there is pressure gradient, more particles are gyrating in one direction through a side of a reference surface than the other, causing a net fluid drift. The third term is a particle drift due to electric fields perpendicular to $\vec{B}$ arising from charge polarization in the plasma, which can ultimately lead to fluid instabilities since this velocity is in opposite directions for ions and electrons.

The physical picture becomes even more complicated in a tokamak, where additional forces can effect the perpendicular velocity. The centrifugal force is $\vec{F}_{\rm cf} = mv_\parallel^2\frac{\vec{R}_c}{R_c^2}$ arising from curved magnetic field lines, where $v_\parallel^2$ is the average square of the random thermal velocity along the magnetic field lines and R_c is the radius of curvature. We can find the perpendicular velocity due to $\vec{F}_{\rm cf}$ by using the equation of motion and taking the cross product with $\vec{B}$ to obtain the curvature drift

$$\vec{v}_R = \frac{mv_\parallel^2}{qB^2}\frac{\vec{R}_c\times\vec{B}}{R_c^2}. \tag{1.11}$$

When the magnetic field strength is stronger on one side of the particle's orbit than the other, then a particle drift can arise due to ∇B because the particle's orbit is larger on the weaker field side. This means that after averaging over the particle's orbit, the net force felt by the particle is calculated to be $\langle \vec{F} \rangle = \mp q \frac{v_\perp^2}{2\omega_c} \nabla B$, and the resulting perpendicular velocity is

$$\vec{v}_{\nabla B} = \pm \frac{v_\perp^2}{2\omega_c} \frac{\vec{B} \times \nabla B}{B^2}, \tag{1.12}$$

where the constant $v_\perp$ is determined by the initial conditions on the equation of motion. More details about drift velocities can be found in plasma physics textbooks [5, 12].

The plasma leaving the core and interacting with the walls and divertors is the issue that has motivated this research, but there are certiainly other challenges to obtain fusion energy. The core and edge/SOL plasma is subject to turbulent dynamics, and as a result, heat, particle and power transport occurs from the hot core plasma out to the edge and SOL region [13]. The energy of the plasma in the SOL can be affected by injecting neutral gas or changing the magnetic field geometries near the divertor [9]. But ultimately, the plasma imposes severe heat flux and particle fluxes on the first wall and divertor targets, resulting in engineering issues affecting practical implementation of fusion technology. The structural materials of a reactor - the first wall, divertor target, vacuum vessel, and blanket - will be under intense structural loads, high temperatures, and/or significant neutron fluxes. Thus, the challenges are to optimize the strength and tensile properties of materials effected by the cyclical temperature extremes of a pulsed fusion device and to understand the impact of microstructural damage effects in neutron irradiated materials [14] on material thermomechanical properties and on the interaction and retention of D, T, and He. In particular, one of the biggest science and engineering

challenges for a practical fusion energy device is the interaction of the edge/SOL plasma with the first wall and divertor target materials.

1.3 Engineering issues with plasma material interactions

Plasma-material interactions (PMI) is a subject of very active research because the materials need to withstand extreme conditions and affect the plasma as little as possible. Although plasma in the SOL has very different properties from the core plasma with reletively low temperature ($\sim$ 10 eV) and density ($> 10^{18}$ m^{-3}), these plasma conditions can majorly affect the materials, which in turn, will affect the plasma as well.

What makes PMI research interesting is the multiscale and synergistic physics that govern each phenomena one wants to study. Here is a short overview of these challenges. Plasma significantly increases the temperatures of the divertor and first wall materials. It is expected in ITER that the W divertor will operate in the range 800 to 1200 K with a heat load greater than 10 MW/m^2, and the Be first wall can expect temperatures greater than 500 K [10]. This heat can change bulk properties such as tensile strength, but the material's ability to reliably conduct heat to the coolant is of great concern. Thus there is a need for active study on the issue of thermal conductivity in this environment [15]. Plasma ions cause the materials to sputter neutral atoms into the plasma. If these atoms become ionized, then they can possibly poison the core plasma or be re-deposited elsewhere in the chamber. The implanted plasma ions can accumulate in the material surface, causing stresses and morphological changes to the material interface. In some instances, like the He induced nano "fuzz" structures that can form on W surfaces, the change

of morphology greatly changes the material properties on the surface [16]. Some implanted atoms can diffuse deeper into the materials and be trapped in material defects. This is an issue regarding the retention of radioactive H isotopes, which is a safety issue and can affect the tritium (T) fuel cycle. Complicating these issues further, high energy neutrons colliding with the materials cause damage cascades in the material lattice, increasing the number of defects that can trap T as well as changing bulk properties of the material. Releasing high energy particles from the core due to turbulent instabilities add transient fluxes of heat and plasma to the complicated PMI repertoire. Current research on these issues is summarized in the next chapter to show the current status of relevant PMI research and to identify key issues for further study.

Chapter 2

Previous experimental research on plasma material interactions

2.1 Basic Processes

This chapter explores the current landscape of plasma-material interactions (PMI) research. There are many topics of interest to the PMI field because it is a complex, synergistic, and multiscale problem. The simple picture of a ballistic ion impacting the surface of a perfectly ordered crystal does not explain all the phenomina observed in plasma-material interactions (figure 2.1). On the micrometer to milimeter scale, the plasma-facing component (PFC) surface and plasma can encounter many different physical processes. Some PFCs can react chemically with H isotopes and be chemically eroded. For instance, a C material can form methane by bonding to implanted H atoms. Low energy ions can be reflected by the material surface, transfering some of its energy to the lattice and picking up an electron. Physical sputtering of lattice atoms also occurs and can inject impurity atoms into the SOL and edge plasma. There the impurities can be excited by the plasma, which removes energy from and cools the plasma, be ionized by

the plasma, move through the plasma, and then be redeposited elsewhere on the surface. This redeposition can occur over relatively long ranges. In some cases, redeposited PFC atoms can form amorphous layers and be co-deposited with H isotopes. Implanted H isotopes on the surface can recombine into molecules and evaporate back into the plasma. Once in the plasma, the molecules can dissociate, re-ionize, and either be implanted again or be recycled back into the plasma. All of these processes can happen in fusion environment, making it very difficult to conduct systematic experiments focusing on one phenomina.

These are the processes that occur on the surface, which is only half of the problem! At the atomic to micrometer scale, the physics of implanted plasma atoms are an important topic of study due to inventory build up in the material, and this inventory can also affect the bulk properties of the PFCs. Figure 2.2 shows a potential energy diagram of an H isotope in a material, like W, where thermal energy is required for an atom to migrate through the lattice (i.e. in solution with W) by overcoming various potential wells. To initially enter solution the ion must be implanted with an energy $\geq E_{\mathrm{S}} + E_{\mathrm{D}}$, overcoming the potential barrier at the surface. Once this occurs, H/D/T (hydrogen/deuterium/tritium) fuel in solution with the PFC can saturate this implant region, which is defined by the ion stopping depth due to the inelastic collisions with electrons (i.e. near the Bragg peak). Atoms that acquire the activation energy for diffusion (E_{D} in figure 2.2), by thermal vibrations, can jump to another lattice site. If the atom jumps into a defect site, such as a lattice vacancy or void where the potential well (i.e. E_{T}) is much greater than E_{D}, then the atom requires more energy to jump to another lattice site. This is why some atoms become trapped in defects and can accumulate there, as illustrated by the "fuel trapping at defects" schematic shown in figure 2.1. In this way, implanted atoms can accumulate in large amounts to

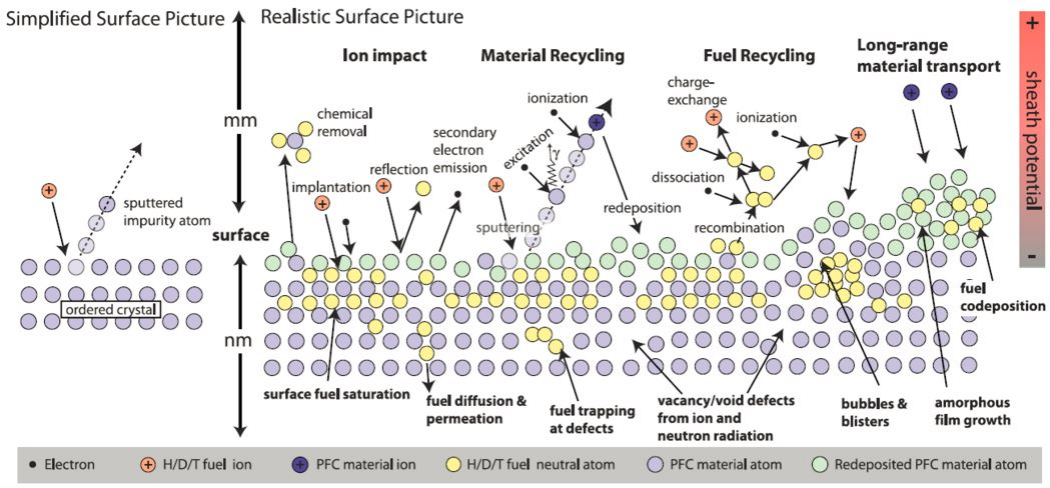

Figure 2.1: Schematic of the complex, synergistic material interface exposed to plasma, where the simplified ion-atom interaction is not sufficient to explain the multiscale physics of plasma-facing components (PFCs) [17].

form bubbles and blisters in the lattice. PFC defect densites can increase with irradiation from fusion neutrons causing damage cascades in the lattice, which in turn can provide more trapping sites for H isotopes.

The leading PFC candidates, W and Be, have been chosen primarily because of their material properties when exposed to the plasma environment. Be is a good candidate is because it has great O_2 gettering abilities, presents low core plasma contamination risks because it is a low Z material, and will retain low T inventory. W is a good candidate because it has a very low sputtering yield and high sputtering threshold energy, does not chemically sputter with H isotopes, does not co-deposit with H isotopes, and has very low T retention properties [11]. Since the divertor and first wall materials of the flagship nuclear fusion test reactor ITER will be comprised of W and Be [10], the focus of this chapter will be mainly on the PMI experiments with these materials. The experiments in the following chapters only use W samples because, unlike Be, it is non-toxic, which is experimentally more accessible. However, note that other materials such as C composites or steel have been extensively studied, so relevant results from these materials may also be

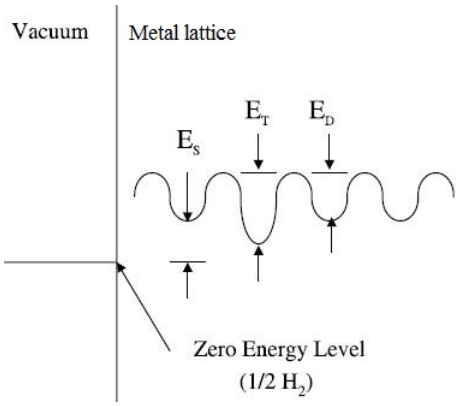

Figure 2.2: Potential energy diagram for H in an endothermic material, where the implanted atom's thermal energy is requried to jump over the potential barriers between lattice sites. E_{S} is the solubility activation energy, E_{D} is the activation energy for diffusion, and E_{T} is the activation energy to escape a trap due to a material defect [18].

included in this section.

2.2 Erosion of materials due to plasma exposure

The conditions in a fusion plasma environment are sufficient for the plasma to effect the structure of the plasma facing material from the atomic level up to macroscopic levels. At the atomic level, energetic ions can cause the material to eject a lattice atom into the plasma, a phenomenon called sputtering. Implanted atoms can stress the lattice enough to change its structure, creating nano and micro scale morphology changes, and in some cases, these small features can continue to grow so that they effect macroscopic material properties. This section will review the plasma and material conditions for various morphological effects to occur.

Erosion of the divertor and first wall materials caused by physical sputtering needs to be avoided. Not only is erosion an issue but also the sputtered atom can ionize, which could effect properties of the core plasma as well as effect other materials in the vacuum vessel. In ITER, energetic plasma ions bombard the walls

with projected energies of 100-500 eV and the divertor with energies on the order of 1 eV [11]. Physical sputtering yields are a function of the mass ratios of the incident particle to the surface atom and the binding energy of an atom in the surrounding lattice, so yield is reduced in materials with higher mass. Figure 2.3 shows measurements of the sputtering yields versus ion energy in Be, C, and W. The yields are calculated by weight loss measurements. W has the highest resistance to sputtering, having yields less than 10^{-3} atoms/ion for fusion relevant plasma ion energies. Be not only has higher yields ($> 10^{-2}$) but also has a lower sputtering threshold; therefore, erosion is one of the biggest disadvantages for using Be. The data for the sputtering yields for C do not match the theoretical prediction because of chemical erosion effects with D and O [19]. From weight loss measurements the net erosion is really what is observed. Under realistic divertor conditions, the neutral surface atom ejected into the divertor plasma can be ionized and redeposited approximately within the length of the gyroradius [20], reducing the net erosion. However, sputtered atoms have been observed to contaminate the core plasma [21] causing radiative energy losses and possibly disruptions. To reduce core contamination from heavy ions like W, ITER is planned to have a W divertor and use Be as the first wall material [22]. The JET tokamak has observed that Be can mix with other plasma facing materials after sputtered Be atoms are ionized and redeposited on C [23]. Looking at figure 2.4, the baking temperature of the mixed materials must exceed 623 K to remove the excess trapped hydrogen isotopes [24], so mixed co-deposits on plasma facing materials resulting from sputtering is an active research area.

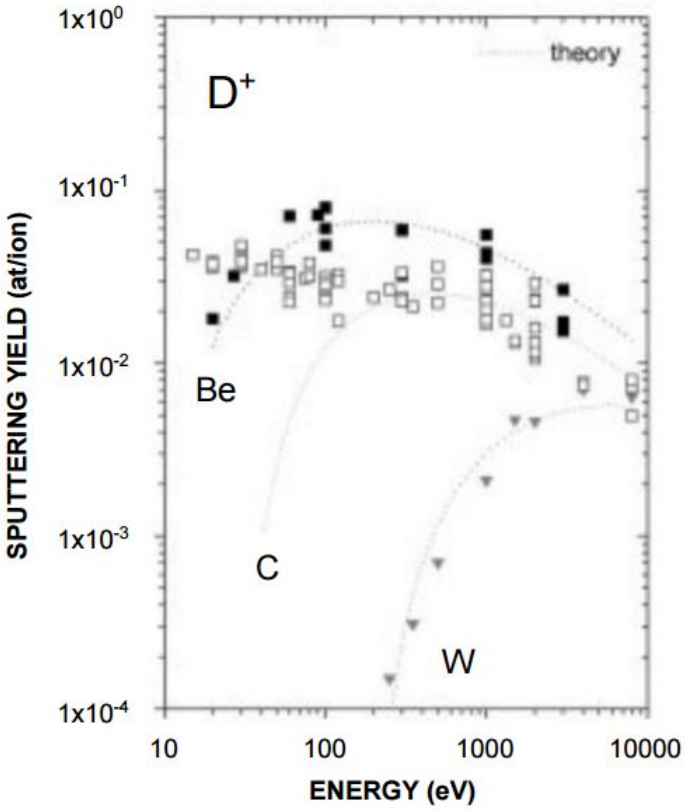

Figure 2.3: Measured (points) and theoretical (lines) physical sputtering yields on Be (filled squares), C (open squares), and W (upside-down triangles) due to D plasma bombardment [19].

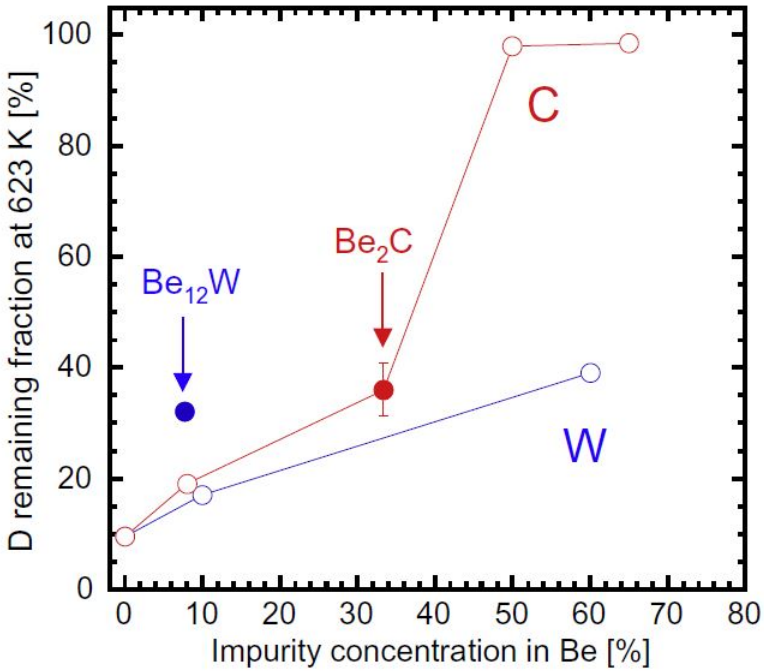

Figure 2.4: D remaining after baking samples at 623 K in Be-containing samples as a function of each impurity (W or C) concentration in Be [24].

2.3 Surface Morphology Evolution

Over the range of material temperatures that plasma facing materials can have, D plasmas have been shown to change the surface features of various materials. Plasma ions that are implanted in the surface of materials can find lattice defects and be trapped in the material, where accumulation of D atoms in the defect can stress the lattice. When this stress becomes large enough, these cavities can grow into larger cavities creating dislocations, which in turn can then capture more D atoms. When these D filled cavities populate across the material surface, they can become interconnected and coalesce, forming visible blisters on the surface and can even lead to exfoliation of the overlaying layers [11]. Figure 2.5 shows the resulting morphology change to a W sample exposed to 100 eV D plasma in a divertor simulator device called PISCES-B, where the W sample is at nearly room temperature and 673 K. Blistering in W has been observed to occur in a wide

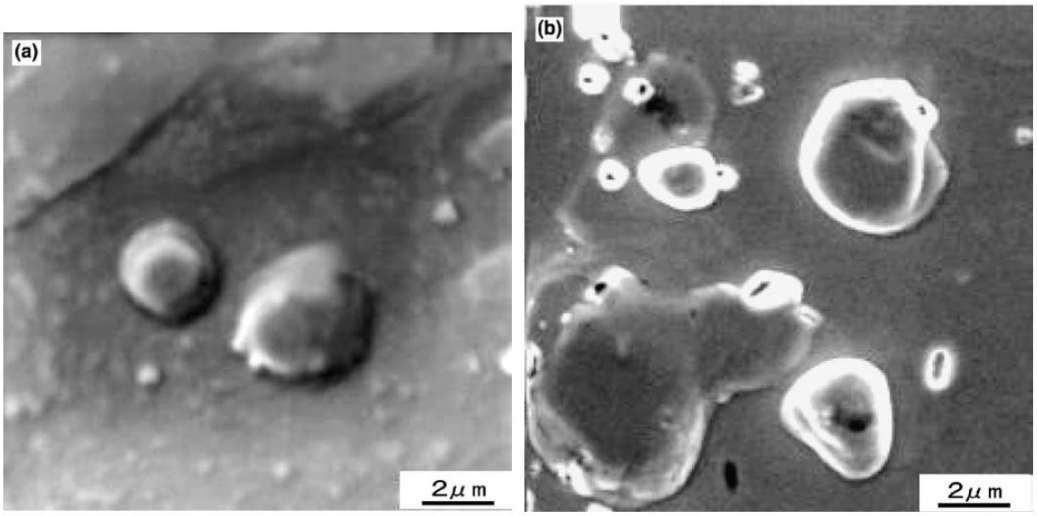

Figure 2.5: SEM images of blistered W with 100 eV D^+ ions at 333 K (a) and 673 K (b), taken from experiments in [26].

range of temperatures from about room temperature to 873 K [25]. Blister density is significantly lower at lower temperatures and also can be affected by the way the W samples are created [26]. Above 873 K, the retention of D atoms in W is reduced, preventing the nucleation of D atoms to form blisters. Blister formation in Be and stainless steel have also been observed, where ideal temperatures for formation are less than 500 K for Be [27] and less than 150 K for stainless steel [28]. At any rate, blistering will inevitably occur in the W divertor in ITER due to the anticipated high temperatures. Simulations in [29] (see figure 2.6) have predicted that blisters will accumulate over tens of centimeters along the divertor.

He is a product of the D-T reaction in a fusion environment, and therefore PMI due to He and D-He mixed plasmas must be understood. The effect that He plasma has on materials has produced a vast amount of experimental interest, namely due the drastic morphology changes shown to happen in W and Be. Under the right material temperature and plasma conditions, He plasma implanted in the surface can nucleate in defects, stress the lattice, and introduce unique surface

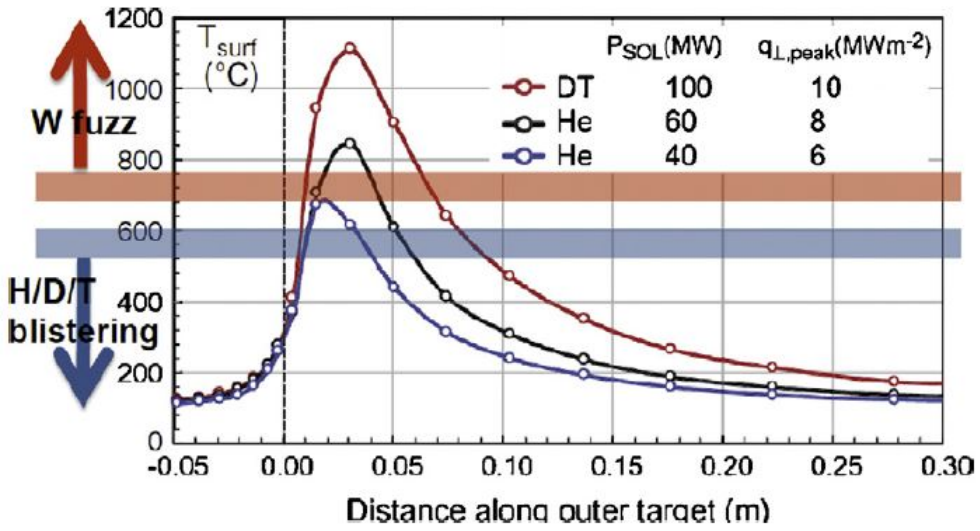

Figure 2.6: Simulation results of temperature distributions on the W divertor in ITER [29], where the conditions for H isotope blistering and He induced "fuzz" are labeled [25].

features. In the case of W, He nucleates to form bubbles under the surface, and after some threshold fluence of plasma, nanometer sized tendril-like structures begin to form on the surface, often called W "fuzz" [16, 30]. The requirements for fuzz to form span the temperature range 900-2000 K and ion energy greater than 20 eV, for a sufficient dose of He plasma. These structures are expected to appear over a significant portion of the ITER divertor (see figure 2.6). Fuzz thickness can exceed several microns as seen in figure 2.7(a). Above roughly 2000 K, W nears its recrystalization temperature, and He filled cavities can burst, leaving pits and holes on the surface. In either case, He induced structures leave W with poor thermal conductivity and mechanical properties [25]; however, the advantage of fuzz is that it significantly reduces H isotopes from entering into the bulk of W, reducing T inventory [31]. Be also forms nano-sized structures on its surface. These nearly identical cone-like formations appear on Be with a wide range of temperatures 300-770 K due to He and even D plasmas with ion energies around roughly 100 eV [32] (see figure 2.7(b)). The complicated physics of the origin and growth of these

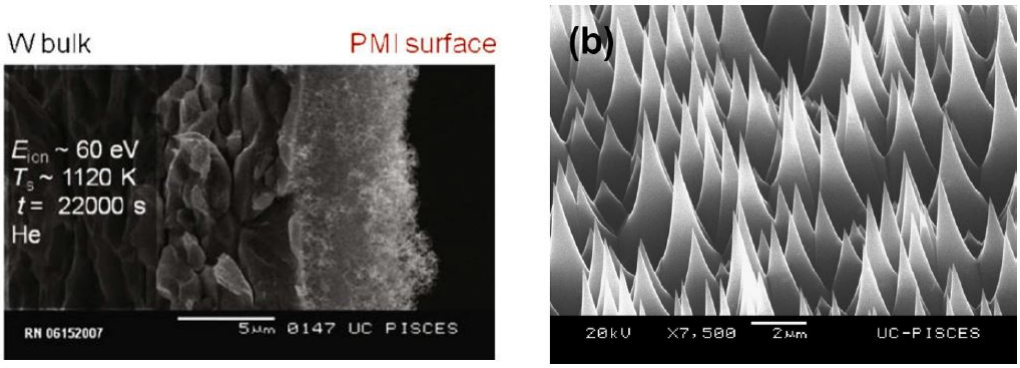

(a) (b)

Figure 2.7: SEM images of He induced W "fuzz" [33] (a) and He induced Be cone structures [32] (b).

structures are still not well understood, but the conditions for occurence have been well documented and are a contining active area of research.

2.4 Retention of hydrogen isotopes in tungsten

This section will review the general results of D retention in W. Retention in other materials has also been extensively studied [34]. However, retention in W is the primary material for this dissertation, so the scope of the discussion here will be narrowed to primarily discuss the research progress on this material.

The retention of the radioactive tritium (T) isotope in the materials of a fusion device create important concerns regarding practicality and safety. For practical operation of a fusion facility, any sinks to the T fuel cycle need to be mitigated, and the primary sink of H atoms in a tokamak are from accumlating inside plasma facing materials. Since T is radioactive, there are governmental safety guidlines that also need to be addressed. A limit of 1 kg of irremovable T is imposed on the future ITER device in order to avoid a catastrophic incident requiring the evacuation of the population around the facility. Therefore, a 700 g measurement of T

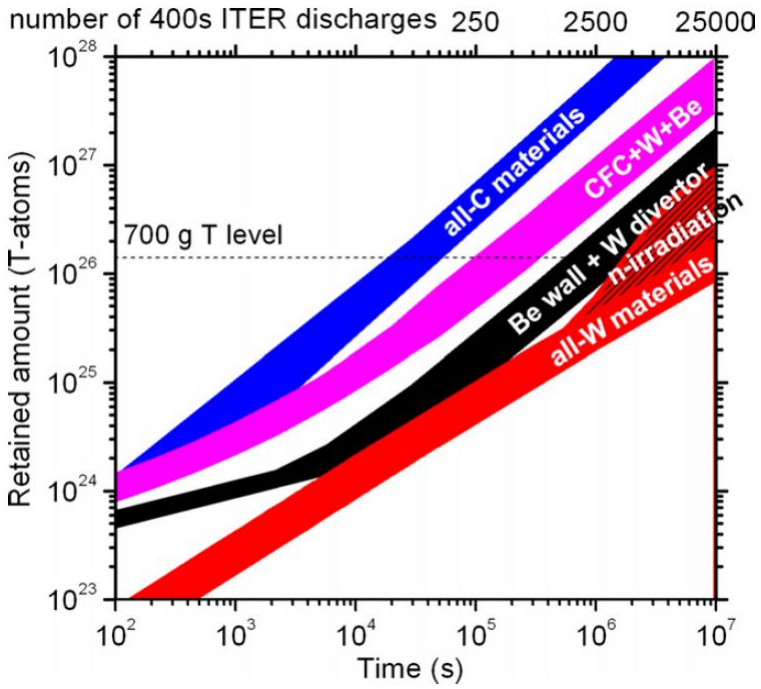

Figure 2.8: Predicted T inventory in ITER for various plasma facing materials with the 700 g administrative T limit indicated by the dashed line [34].

is the likely administrative limit due to measurement uncertanties. Accounting for some T mitigation, this limit will be reached in W after an estimated 25,000 ITER discharges that last about six minutes each (figure 2.8), or much less, if the materials are heavily damaged by fusion neutrons. Thus, understanding and mitigating T retention is a great engineering problem that needs to be solved for practical power plant operation. Current research progress on the basic retention features of W, the development of T removal techniques, and the effect neutrons have on H isotope retention in W will be discussed. Note that many experiments use the D isotope instead of T. This is because handling activated materials is difficult, T is not widely available, and since they have the same number of protons in their nucleus, they interact with electric potential wells similarly and therefore have the similar trapping properties [35, 36, 37].

2.4.1 Significant variation in retention measurements

Hydrogenic retention can vary over a wide variety of material and plasma parameters. The plasma fluence (i.e. total dose), the material temperature, the material composition and lattice structure, and even the ratio of different plasma species all play a role in the amount of atoms that are ultimately retained. Comparing the dose of plasma (i.e. fluence) to the amount of atoms retained, there appears to be a saturation limit in W. Depending on the temperature, this saturation can range 10^{20}-10^{22} atoms/m^2 [38]. However, increased temperature introduces morphology effects to the W, shown in the previous section. Figure 2.9 displays a non-monatonic behavior across temperature, looking at the measurements resulting from various plasma devices. Some measurements increase to a maximum with exposure temperatures around 500-600 K, where enhanced blister growth could explain the increase in retention. The retention values from all experiments then tend to decrease with W temperatures greater than 673 K, where blisters can still occur, but the thermal energy of the system may reduce the effectiveness of atomic trapping in defects. Figure 2.9 also shows the wide variance in retention measurements, making it quite a challenge to create accurate predictive models. One of the drawbacks to having Be as plasma facing material is its ability to accumulate co-deposits around the tokamak [23]. Fortunately, H isotopes do not appear to be accumulated in redeposited W, and therefore does not add to the trapped inventory via a codeposition mechanism [11]. However there has been research that has studied possible W-Ta alloys to reduce the W material's brittleness. The alloy's retention is lower than in pure tungsten, possibly due to the alloy's abililty to prevent blister growth [39], but implimentation of an alloy in ITER or a next step device still requires further research [40]. The creation of transmutants like Re and Os from fusion neutrons also reduce retention, possibly due to a reduction in H

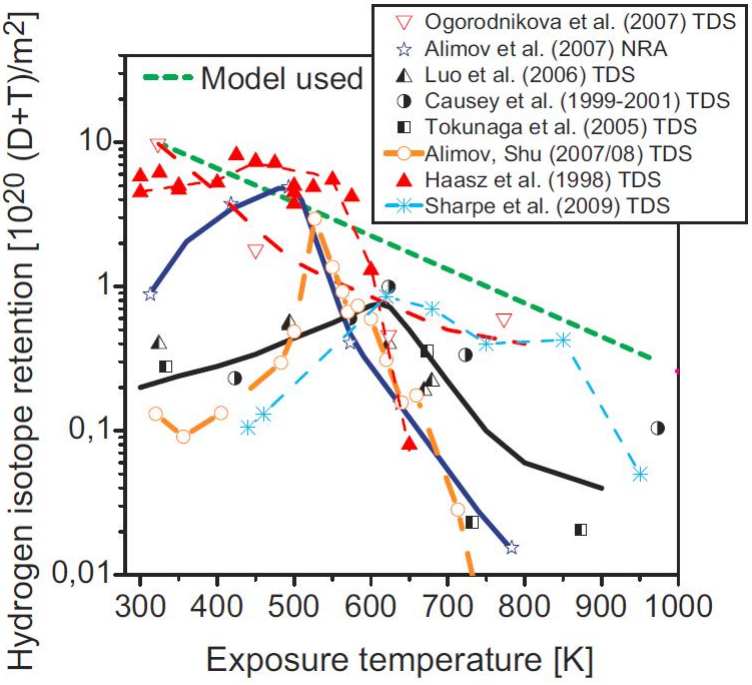

Figure 2.9: Temperature dependence of hydrogenic (either D or T) retention in W, measured after exposure to ions at various fluxes and fluences [38].

trapping defects in a W-Re alloy [41]. Realistically, He ash will form a significant fraction of the ion population in a burning fusion plasma. Implanted He atoms have been shown to reduce the effectiveness of D atoms diffusing into the bulk of W, reducing the trapped D inventory [42]. This is all somewhat good news for mitigating retention, but again, there is still significant difficulty in incorporating these effects into a predictive model of retention.

2.4.2 Tritium removal techniques

During the lifetime of ITER or a future working reactor, the T inventory limit will certainly be reached (figure 2.8) unless effective T recovery techniques are implemented. Several techniques have been proposed that can slow the build up of T in the walls and divertors. However, it is yet to be seen how effective some of these removal strategies will be in real fusion reactor conditions. There is also a

fine balance weighing the technique's ease of T removal against its impact on the overall energy efficiency of the reactor.

To get the T out of the plasma facing materials, an array of methods have shown to reduce trapped inventory. The JET tokamak introduced T in an experimental campaign and tested several conditioning techniques after its conclusion [43]. These included running plasma shots with D and H plasmas, pressurizing the vaccum chamber with D gas to "soak" the vessel overnight, and baking tiles with exposure to N_2 and air during venting procedures so that molecular recombination on the material surfaces would be enhanced, increasing evaporation. Be co-deposits will consequently be the largest storehouse of trapped T in the machine. To remove T from these co-deposits, experiments at JET show efficient removal of D from co-deposits by baking the tiles at 673 K in an O_2 rich environment [44]. With W being the only plasma facing material, there will be no co-deposits, and a lower baking temperature of about 500-550 K could be sufficient [45]. This is, however, not taking into account the effect of neutron damage, which increases the defect density in W, so this baking technique requires further validation in a more realistic fusion environment. Unfortunately, heating up the tiles to sufficiently high temperatures may be difficult. Localized heating from lasers can ablate co-deposited layers [46] as well as high T accumulated regions in the divertor [47] has shown it that in principle it can extract a significant amount of T in a tokamak. However, a very significant hardware development effort would be needed to implement a laser that can scan across the entire inner and outer divertor in order to remove T. Flash lamps have also been used to heat slightly larger regions approximately 15 cm^2 with reasonable T removal rates [48], but again, large scale implementation is still a significant hurdle.

Isotope exchange is a proposed technique that is neither localized to small

regions in the tokamak nor as energetically wasteful as baking the wall and divertor tiles. This technique could be implemented in a tokamak as a part of their wall conditioning protocals after a D-T plasma campaign. Isotope exchange has been studied by sequentially exposing D then H ion by way of ion beam [49] or a linear plasma device [50] and measuring the resulting D retained. During D ion exposure, the implanted D atoms can diffuse into the W and accumulate in traps. Then the D ion source is turned off, and the pure H ion source bombards the sample. In this H plasma phase, the implanted H atoms compete for available trapping sites with the D atoms that have been released from traps due to the thermal vibrations of the lattice. To achieve a significant amount of isotope replacement in the material, equal or greater fluences of the exchanging plasma species is required (figure 2.10). The general conclusion, unfortunately, is that isotope-exchange is ineffective at replacing trapped inventory at depths greater than a few microns. However, isotope exchange does lend itself to interesting basic retention studies that can provide benchmarks for simulation. In this work, isotope exchange experiments were carried out in W samples that were subjected to ion beam displacement damage, and used the results to develop and test a model of hydrogenic diffusion, trapping, and exchange.

2.4.3 Retention after displacement damage from energetic neutrons

The fusion reaction will produce 14.1 MeV neutrons that are not only essential for energy production but also an engineering nuisance due to its impact on reactor materials. Unlike plasma ions, the paths of neutrons cannot by controlled by magnetic fields, and therefore the entire device will be bombarded with neutrons. To quantify the damage that is produced in materials by energetic par-

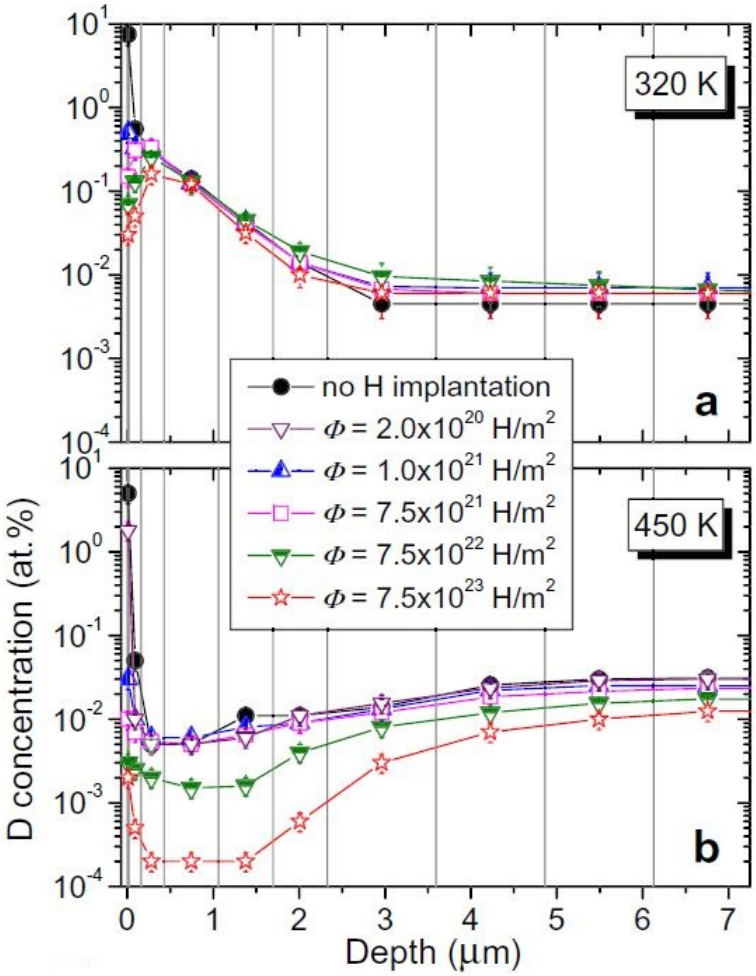

Figure 2.10: D concentration depth profiles with W temperatures of 320 K (a) and 450 K (b). Each curve shows the D remaining after a given H plasma fluence [50].

ticles, the displacements per atom (dpa) unit is used, where it is a measure of the fraction of lattice atoms that have been displaced from their initial lattice site. It is projected that over the lifetime of the ITER device the divertor will suffer 0.6 dpa, and the first wall will suffer 1 dpa [51]. Here, 1 dpa means that 100 percent of atoms will have been displaced from their original lattice site at least one time. Each time a neutron collides with a lattice atom it induces a damage cascade in which the displaced atom has so much energy that it can then collide and displace other atoms. Binary-collision models have shown that energetic particles cause a chaotic sequence of collisions due to recoiling atoms causing additional collisions [52], and molecular dynamic (MD) simulations show that a liquid-like zone can form in the center of a collision cascade [53] that quenches to form an amorphous structure [54]. The result of an MD damage cascade can be seen in figure 2.11, which is an MD simulation of $\sim$180 Cu ions with 50 keV impinging on a Cu lattice [55]. Even with this small dose of energetic ions, this result qualitatively shows how disordered the lattice structure can become. The response of damaged materials to tokamak plasma conditions is clearly an issue that needs to be addressed for long term operation of a reactor, when damage reaches large dpa values. A summary of results regarding the W material will be given here.

Neutron induced displacement damage creates additional defects in the material that changes material properties and enhances the retention capacity for T. The biggest material property change observed in n-irradiated W samples is embrittlement. The ductile to brittle transition temperatures (DBTT) were significantly reduced under irradiation [56]. The work by [57] argued that swelling was not an issue and that there is not a sufficient amount of work to discount the effects of the changes to thermal conductivity. Recent studies have shown, however, that thermal conductivity is significantly reduced after displacement damage

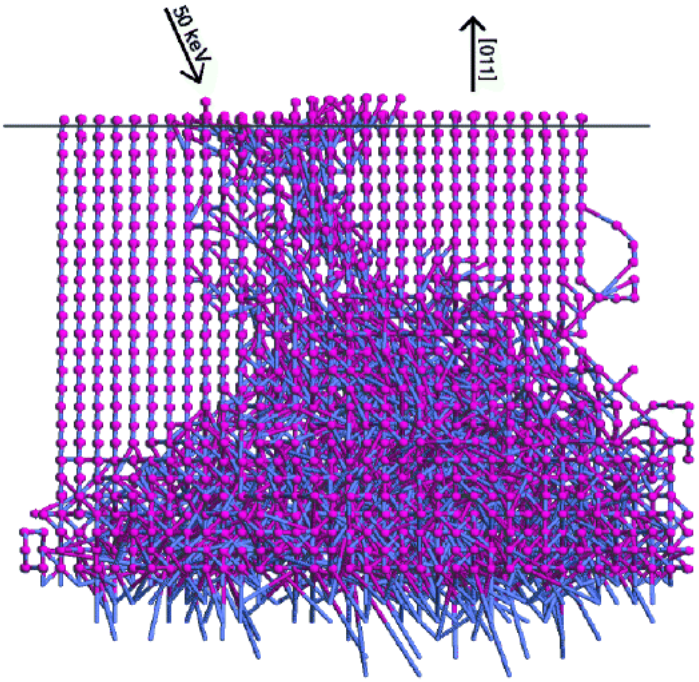

Figure 2.11: MD simulation of 50 keV Cu ions on a Cu lattice. The purple spheres are Cu atoms and the blue lines connect the initial and final position of one atom [55].

[15]. Additionally, work done by [57] showed that pure W embrittles much less than W-10%Re alloys, which have been preferred due to their low retention properties. The dominant defect introduced by neutron damage at relevant material temperatures is point defect vacancies [58]. These new vacancies are distributed uniformly throughout the lattice and provide more trapping sites for T, increasing the retention capacity of W [59].

Neutrons produce samples that are activated, which are difficult to obtain and handle. However, the use of high energy high Z ions have been used as fusion neutron surrogates. At the damage levels studied here, the effects of transmutations should be fairly small [58], so the effects of retention and some mechanical property changes can be mimmicked by heavy ion damage cascades. Ions have much higher stopping power in materials and can only affect the near surface. However D retention profiles from the surface in to the peak of the computed ion

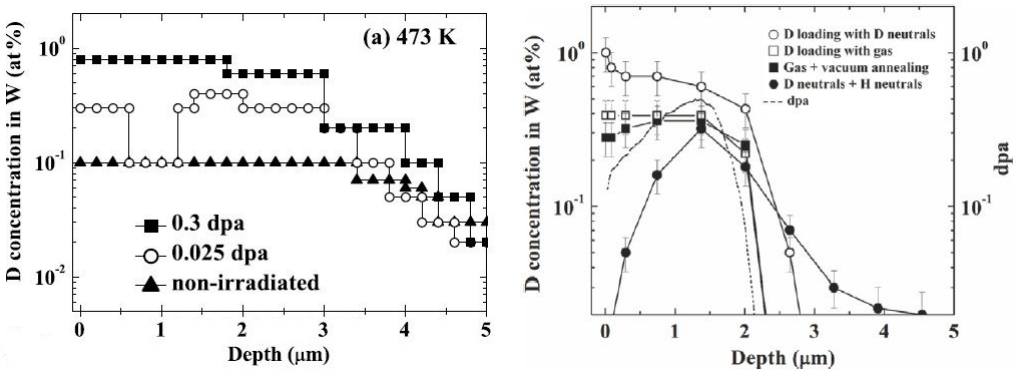

(a) (b)

Figure 2.12: D concentration depth profiles in W with neutron induced damage up to 0.3 dpa (a) and with ion induced damage at 0.5 dpa (b). Retention of the 0.3 dpa neutron damage data - black squares in (a) - is comparable to the 0.5 dpa ion damage data - open circles in (b) - up to the depth where peak ion damage is reached, $\sim 1.5\mu m$, indicated by the dashed line in (b). The neutron irradiated samples were exposed to D plasma at 473 K, and the ion irradiated samples were treated with D neutrals at 473 K. Experimental details of neutral D adsorption can be found in [59], where these figures were obtained.

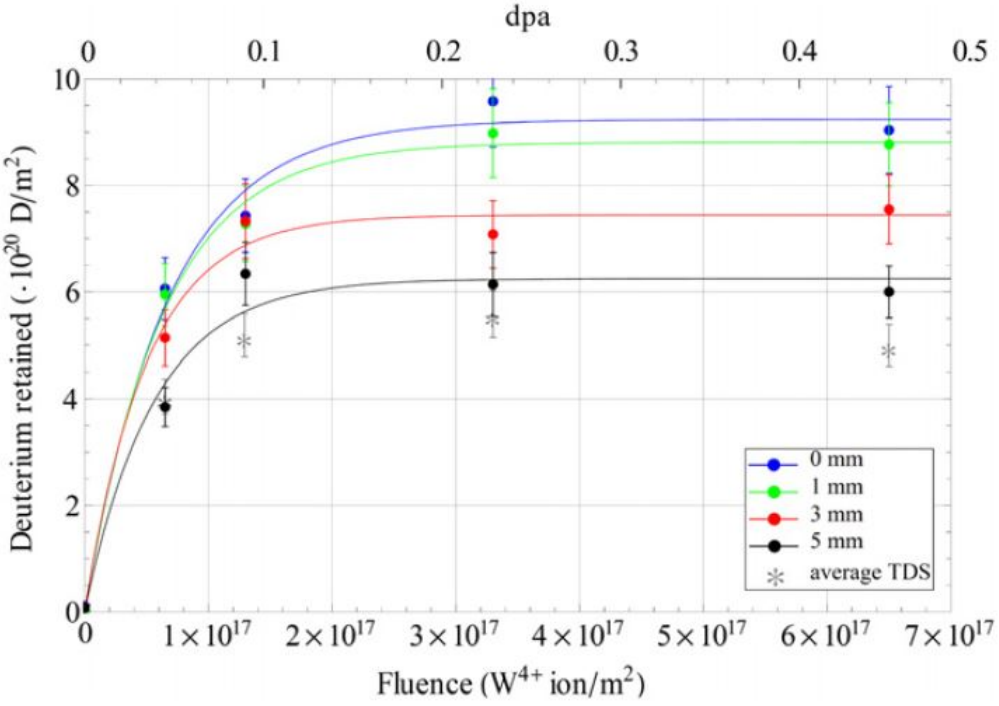

Figure 2.13: D retention in W for increasing levels of W ion induced damage, where retention saturates beyond 0.2 dpa [60].

damage profile compares well with n-irradiated samples with similar dpa values (figure 2.12). Also, the change in plasticity is very similar to the n-irradiated case [61]. For these reasons heavy ion irradiation has become an acceptable means to study displacement damage. There are a few other drawbacks to using heavy ions, but are managable under certain experimental controls. For instance, the effect of contamination by using ion species, such as Fe [62] or Si [63] instead of W, could affect measurements, but this can be mitigated by keeping the added impurity content at or below the intrinsic level of impurities present from manufacturing. The effect of damage saturation, seen in figure 2.13, shows that damage over 0.2 dpa may not change the retention capacity in W. This phenomena has yet to be confirmed with neutron damage, which introduces transmutants and damages uniformly in the material. However, damage levels below this value are still of concern for ITER and other nuclear-grade fusion devices. Therefore in this dissertation, heavy ions were used to induce displacement damage, keeping these limitations in mind.

2.5 Impact of tritium retention in PFCs on the tritium fuel cycle

In order to put the importance of T (tritium) retention into perspective, we can estimate the probability for an injected T atom to become trapped in the device and compare that to the impact this has on the regulatory T inventory limits for ITER. Referring to figure 2.14, the mass balance at the wall of the device can be defined as

$$\dot{M}_{\mathrm{T}}^{\mathrm{inj}} = \dot{M}_{\mathrm{T}}^{\mathrm{burn}} + (1 - R)\,\dot{M}_{\mathrm{T}}^{\mathrm{wall}}, \tag{2.1}$$

where $\dot{M}_{\mathrm{T}}^{\mathrm{inj}}$ is the rate of T mass injection into the plasma, $\dot{M}_{\mathrm{T}}^{\mathrm{burn}}$ is the total T mass burn-up rate from fusion reactions, R is the recycling coefficient, which is the probability that a T atom will be recycled back into the plasma from the wall, and $\dot{M}_{\mathrm{T}}^{\mathrm{wall}}$ is the rate of total T mass arriving at the divertor and first wall. Equation (2.1) says that each T atom injected into the plasma will either be burned up or will ultimately be move into the wall or pumping system. In the core plasma, the mass balance can be written as

$$p_{\mathrm{burn}}\eta_{\mathrm{fuel}}\dot{M}_{\mathrm{T}}^{\mathrm{inj}} = \dot{M}_{\mathrm{T}}^{\mathrm{burn}}, \tag{2.2}$$

where p_{burn} is the probability that a T atom will fuse before being lost from the plasma and η_{fuel} is the T fueling efficiency defined as the ratio of the rate of T^{+} production in the core normalized by $\dot{M}_{\mathrm{T}}^{\mathrm{inj}}$. If the tritium breeding ratio (TBR) is greater than one, meaning that more T is being made in the blankets than is burned up, then the rate of T mass production, $\Delta\dot{M}_{\mathrm{T}}$, is given as

$$\Delta\dot{M}_{\mathrm{T}} = (\mathrm{TBR} - 1)\,\dot{M}_{\mathrm{T}}^{\mathrm{burn}}. \tag{2.3}$$

Now we seek to estimate the maximum allowable trapping probability of an injected T atom and still have TBR>1. This probability can be written as

$$p_{\mathrm{trapped}} = \frac{\dot{M}_{\mathrm{T}}^{\mathrm{trapped}}}{\dot{M}_{\mathrm{T}}^{\mathrm{wall}}}, \tag{2.4}$$

where $\dot{M}_{\mathrm{T}}^{\mathrm{trapped}}$ is the rate at which T is trapped in wall/divertor material surface and substrates and $\dot{M}_{\mathrm{T}}^{\mathrm{wall}}$ has been defined above. For TBR>1 we obviously require that $\dot{M}_{\mathrm{T}}^{\mathrm{trapped}} \ll \Delta\dot{M}_{\mathrm{T}}$. Using this definition of p_{trapped} and the expression for $\Delta\dot{M}_{\mathrm{T}}$,

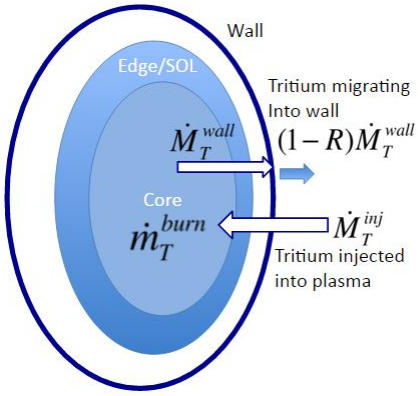

Figure 2.14: Schematic cross-section of a tokamak plasma where locations of the tritium mass rates are indicated [64].

we can write

$$p_{\text{trapped}}\dot{M}_{\text{T}}^{\text{wall}} \ll (\text{TBR}-1)\,\dot{M}_{\text{T}}^{\text{burn}}. \tag{2.5}$$

We proceed by solving equation (2.2) for $\dot{M}_{\text{T}}^{\text{inj}}$ and use the result in equation (2.1). After re-arranging terms we then have

$$\frac{\dot{M}_{\text{T}}^{\text{burn}}}{(1-R)}\left(\frac{1-p_{\text{burn}}\eta_{\text{fuel}}}{p_{\text{burn}}\eta_{\text{fuel}}}\right) = \dot{M}_{\text{T}}^{\text{wall}}. \tag{2.6}$$

Substituting this expression into the inequality given by equation (2.5) and re-arranging terms, we can then write that, for TBR>1, we require that

$$p_{\text{trapped}} \ll (TBR-1)\,(1-R)\,\frac{p_{\text{burn}}\eta_{\text{fuel}}}{1-p_{\text{burn}}\eta_{\text{fuel}}}. \tag{2.7}$$

We can estimate $TBR \sim 1.05$, $R \sim 0.99-0.999$, $p_{\text{burn}} \sim 0.05$, and $\eta_{\text{fuel}} \sim 20-30\%$ to give $p_{\text{trapped}} \sim 10^{-6}-10^{-7}$ [64]. With an expected $\sim 10^{24}$ ions/m^2/s T flux to the ITER divertor with an exposure area of ~2-10 m^2 [65], an expected 10^{5-6} kg of T will have impacted divertor materials after one year of plasma exposure. In other words, the 1 kg T inventory limit will be reached in one year of operation if $p_{\text{trapped}} \sim 10^{-6}$. This is of course assuming that once a T atom is trapped it will

never diffuse back out of the material, which is why understanding trapping and diffusion in PFCs are so very important to fusion science.

This probability calculation motivates the need to study retention because it is a the first major hurdle to overcome T inventory restrictions in next step fusion devices. The experiments in this dissertation reflect this need to understand the basic governing principles behind retention and the physical processes that affect it. Therefore the following experiments attempt to control some the interrelated complexities on the material surface and focus on understanding the key physics of trapping and diffusion. For instance, in most experiments in the chapters that follow, the temperatures of the W samples during plasma exposure will be much lower than relevant fusion PFCs, since we see that surface morphology changes can cause significant variation in retention measurements and introduce additional parameters affecting trapping and diffusion that complicate modeling. Isotope exchange and ion induced displacement damage experiments were done to tease out additional features of trapping physics, like how atoms compete for traps and how defect densities effect diffusion. With focused experiments, a simple model is created in order to build a predictive framework that can illuminate empirical measurements and determine what can be predicted with only a small number of free parameters (i.e. defect densities). The model is benchmarked against the control samples and extrapolated to understand the phenomena observed in isotope exchange and ion induced displacement damage experiments.

The rest of the dissertation is organized in the following way. Chapter 3 describes the experimental tools and methods used to gather retention data. Chapters 4-7 are publications (ch. 7 is currently being submitted) that display each incremental step in the process to create a simplified diffusion model. The first experiments (ch. 4-5) are retention studies with W having temperatures relevant to

first-wall and divertor temperatures. Some of the samples were irradiated with high energy ion beams to create displacement damage, then these samples were exposed to D plasma or sequential D then H plasmas for H-D isotope exchange studies. In these experiments we not only produced novel results for isotope exchange in the face of displacement damage but also learned that high material temperatures present modeling difficulties. This then motivated subsequent studies discussed in chapters 6-7, which present plasma exposures at low material temperatures ($\sim$370 K), where the temperature is high enough for significant H isotope diffusion but low enough to avoid the impact of surface morphology effects such as blistering or erosion from physical sputtering. Chapter 6 briefly introduces a simplified diffusion model and extrapolates predictions to isotope exchange measurements with qualitative agreement with the data. Chapter 7 presents experiments on the diffusion and trapping of D in low-temperature W that is subjected to ion-beam displacement damage. This chapter then presents the derivation of a diffusion model suitable for damaged W, which can reproduce the observed trapping in ion damaged samples. Finally, chapter 7 presents a model that can account for the descrepancies in measured diffusion coefficients across a range of temperatures. Finally, chapter 8 will summarize all of the findings in this work and discuss future experiments and modeling studies.

Chapter 3

Experimental methods and data acquisition

3.1 Tungsten materials and sample preparation

The polycrystalline W samples used in our experiments were purchased either from the PLANSEE Composite Materials GmbH manufacturer in Germany [66] with above 99.97 % purity or from Midwest Tungsten Services, Inc. with 99.95 % purity. PLANSEE is currently the same manufacturer for the divertor for the ITER project [67]. To optimize the thermal and mechanical properties, PLANSEE (and Midwest Tungsten Services, Inc.) uses the powder metallurgy process for W. The W powder comes from hydrogen reduction of the WO_3 raw material with temperatures above 973 K. Sintering of the fine grain powder occurs at 2273 - 2773 K, well below the W melting point (3695 K), and is pressed in a mold. These sintered blanks are then drawn into bars at temperatures around 1873 K. The 9.5 mm diameter bars are then cut and shaped.

Our samples are machined according to the specifications in figure 3.1, where the units in the figure are in inches. These W "buttons" have a leading edge

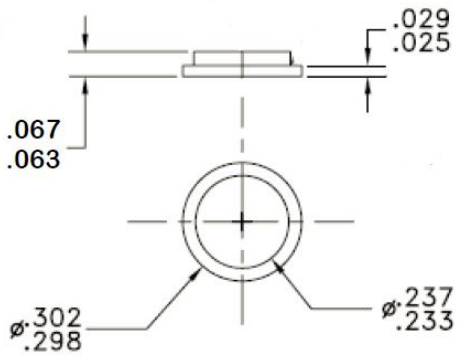

Figure 3.1: Drawing of the machining specifications for the W samples, where the units in the figure are in inches. Looking at the side view of the drawing (upper figure), the sample has a total thickness of 1.7 mm and the leading edge is 0.69 mm. The cross-section (lower figure) shows that the diameter of the plasma exposed surface is 6 mm, and the total diameter that includes the leading edge is 7.6 mm. Machining errors are ± 0.05 mm.

that is held down by the sample holder in our plasma device, so that the inner diameter of the sample (i.e. the plasma exposed surface) is approximately flush with sample holder. The samples are cut to specification with the electron-beam machining (EBM) technique, where high velocity electrons heat and vaporize hard refractory metals with high accuracy.

The machined button sample is then polished mechanically and cleaned to produce a uniform plasma facing surface. An automated grinder-polisher is used to polish the all of the samples simultaneously with three grades of sand paper up to 1200 grit. The result is a mirror-like surface. Using a scanning tunneling microscope at Los Alamos National Laboratory, we observe that the root mean squared surface roughness is 140 nm after polishing. Samples are then chemically cleaned to remove the dust particles and water from the polished surface and the acrylic resin remaining on the back of the samples that was used to attach the samples to the polishing stage. First the samples are placed in an ultrasonic bath of acetone for five minutes, which removes the resin. Then the samples are put in

an ultrasonic bath of an ethanol solution for five minutes to clean off any other oils or particles on the surface. Finally, we anneal the samples at 1273 K for one hour to remove additional impurities remaining from the machining process, such as Cu impurities on the surface from the EBM technique, and ethanol adsorbed on the surface. The samples were held in vacuum with base pressure 4×10^{-6} Pa and heated with infrared lamps outside the quartz tube vacuum chamber. The temperature was measured with a thermocouple inside the vacuum chamber next to the samples.

3.2 Plasma-material experiments simulating a fusion reactor environment

This section will present the experimental devices and procedures for ion beam irradiation, plasma exposure, and isotope exchange. Each experimental campaign included various combinations of heavy ion beam specifications for displacement damage and various combinations plasma exposure conditions. However, the experimental procedures were the same. There are four stages in each campaign that was repeated in the experiments presented in the following chapters. Samples were first damaged with high Z ions at the Ion Beam Materials Laboratory at Los Alamos National Laboratory (LANL). Then plasma exposure was conducted at the UC San Diego PISCES laboratory. Returning to LANL, the plasma exposed samples were analyzed with nuclear reaction analysis (NRA). Finally, thermal desorption spectroscopy (TDS) was conducted back at UCSD. There was about a week of time for travel between San Diego and Los Alamos for each stage of the experiment.

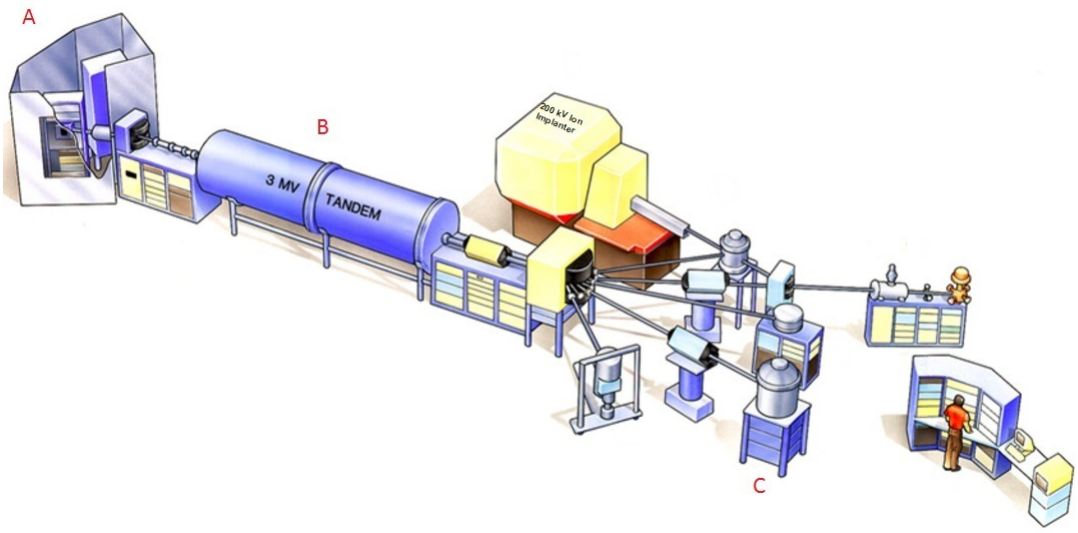

Figure 3.2: Ion Beam Materials Laboratory at LANL. Two sources chambers (A) for either gas or sputtered ion sources are accelerated with the 3 MV tandem (B) and irradiate samples in the general purpose analysis chamber (C).

3.2.1 Tandem ion accelerator

An ion accelerator facility at LANL was used in our experiments to simulate neutron displacement damage and to measure D concentration profiles in W. This Ion Beam Materials Laboratory is a user facility that supports various experiments dedicated to the characterization and modification of materials with ion beams. In our experiments, we used the 3 MV NEC tandem accelerator for both heavy ion irradiation and ^{3}He NRA. Ion energies can range from keV to 9 MeV for ^{3}He or 18 MeV for heavy ions, with beam currents up to a few mA. Figure 3.2 is a schematic of the ion beam laboratory. There are two ion source chambers (fig. 3.2-A) from a gas or sputtered source that share the same tandem beam line (fig. 3.2-B). Multiple endstations are available in this facility for a series of ion beam analysis techniques, but only the general purpose chamber (fig. 3.2-C) was needed for this work.

The tandem ion accelerator accelerates ions electrostatically by using the

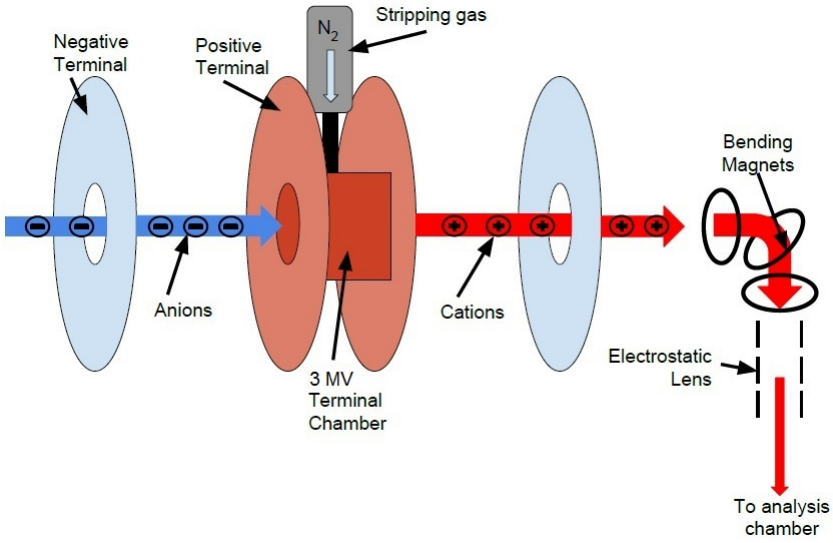

Figure 3.3: Simple schematic of the ion accelerator. The ion is accelerated twice, first as a negative ion and then as a positive ion after electrons are stripped off by colliding with N_2 gas. Then the beam is steered to the analysis chamber.

same electric potential twice (fig. 3.3): firstly on the negative anion and secondly, after stripping electrons off the anion, on the positively charged cations. Anions accelerate to the high voltage terminal impinging on N_2 gas, where electrons are stripped off and proceed towards the second terminal. The anions in both the ^{3}He and heavy ion experiments have a -1 charge state, so the energy of the ions emerging from the tandem is $E = (1 + q)\,V$, where q is the charge state after two or more electrons are stripped off the anion and V is the electrostatic potential energy. These energetic ions are then focused with an Einzel lens and guided to the analysis chamber with magnetic fields.

Both the gas and sputtering sources are used for these experiments, but the irradiation procedures were similar in either case. For the high Z ion beam irradiations, the sputtering source is used to produce the anions. In this source, Cs^+ plasma ions are accelerated towards a Cu (or W) cathode and sputter negative Cu (or W) ions directly. This Cu^- (or W^-) ion is then accelerated through the tandem

via the process described above. The beam spot size is about 3-6 mm^2, which is smaller than the 28 mm^2 area of our samples. We therefore rastered the high Z ion beam across the samples at 512 Hz in the x direction and 64 Hz in the y direction to obtain a relatively uniform exposure to the ions. For the ^{3}He ion beam irradiations, a ^{3}He plasma produced from a radio frequency (rf) source is extracted into a Ru vapor chamber. A small fraction of ^{3}He ions gain electrons through charge exchange by colliding with Ru to form $^3He^-$ and are accelerated through the tandem. After the desired total ion beam current (ion fluence) is collected on the sample, a Faraday cup intersects the beam path, and a new sample is prepared for irradiation.

3.2.2 Heavy ion induced displacement damage

Since the stopping of ions in matter cannot be calculated analytically, displacement damage experiments were designed using the Stopping and Range of Ions in Matter (SRIM) software. SRIM uses a Monte Carlo simulation with the binary collision approximation [68] to calculate the path of the energetic ion in the target material. An impact parameter is randomly selected for the ion-atom screened Coulumb collision at the surface of the target and the software then proceeds to calculate the ion-atom interactions that follow until the ion comes to rest. Target atoms displaced from their initial lattice site can cause damage cascades that displace additional target atoms [69]. This sofware has been verified by hundreds of experiments that measure stopping powers and ion implantation ranges [70]. Since the stopping calculations are largely based on binary-collision theory, SRIM calculations are commonly relied upon in the literature to interpolate ion-solid interactions that have not been experimentaly verified, especially with novel multi-layered targets.

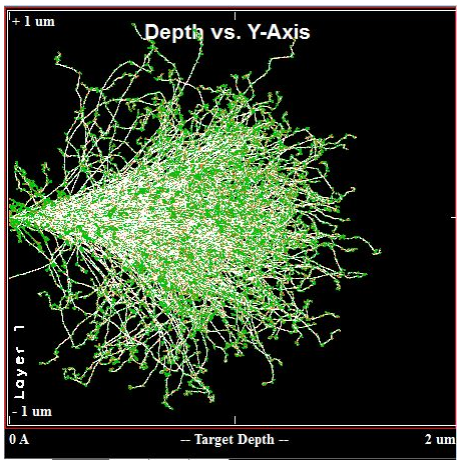

Figure 3.4: Snapshot of the SRIM simulation of 5 MeV Cu ions through 2 μm of a W target.

The data from the SRIM simulation is used to calculate the displacements per atom (dpa), which is a unitless parameter used to quantify damage, as well as the total number of vacancies, and a spatially resolved density of the implanted ions. The "detailed calculation with full damage cascades" option was selected for the SRIM simulations, and the displacement damage threshold energy (i.e. the energy to displace a W lattice atom far enough from its lattice site so it does not fall back into this lattice vacancy) was set to 90 eV as recommended in [71]. Figure 3.4 shows a snapshot of a simulation of 5 MeV Cu ions on a W target. Each line shows the path of a single ion through a pristine W target within the first 2 μm, where collision events are marked with green and orange points along the path.

An important limitation for this type of calculation is that SRIM simulates ion-atom collisions without considering temperature effects. Essentially the simulation is done at 0 K, so that the damage cascade is "frozen in" [69]. Metals, however, can easily recover from displacement damage at elevated temperatures [72] by having mobile interstitials that find and occupy vacancies, which annihilates the Frenkel pair, or by having mobile vacancies that migrate to a grain boundary. For W, interstitials are mobile beyond 27 K, so this effect can be expected with ir-

radiations at room temperature [73]. Therefore the SRIM results over-estimate the displacement damage remaining in the material before plasma exposure. Molecular dynamic (MD) simulations can take temperature into account, but the intensive calculation needed to simulate high fluences of Cu (or W) ion irradiation in W and the resulting interstitial migration in order to calculate the number of atomic displacements and vacancies in our experiments is not available at this time.

The important outputs from the SRIM simulation are number of displacements and vacancies resulting from the damage cascades introduced by ion-atom collisions and the spatially resolved density of implanted atoms after irradiation. Collision event data shown in figure 3.5a is the sum of primary knock-on (PKO) vacancies left by atoms recoiling due to collision with the ion, W vacancies caused by recoiling W atoms displacing other W atoms from their lattice sites, and replacement collisions where recoiling W atoms displace other W atoms from their lattice site and fill the resulting vacancy. These data give the number of displacments, $N_{\text{displacment}}\left(\frac{1}{\text{ions}\cdot m}\right)$, of W lattice atoms used to calculate dpa

$$\text{dpa} = \frac{N_{\text{displacement}}\phi}{N_{\text{W}}}, \tag{3.1}$$

where $\phi\left(\frac{\text{ions}}{m^2}\right)$ is the fluence of the ions and $N_{\text{W}}\left(\frac{\text{at}}{m^3}\right)$ is the atomic density of W. By instead adding together the number vacancies and subtracting the number of replacement collisions, we can calculate the total number of vacancies, which will be useful in the diffusion model in damaged W proposed in chapter 7. Using equation (3.1) and the peak value of $N_{\text{displacement}}$, the ion beam fluence is chosen to achieve the desired peak dpa value. Figure 3.5b shows the average depth where the impinging ion comes to rest in the target, where the y-axis gives the average density per ion fluence. Using the ion fluence chosen for the desired dpa value, we relied on this ion ranges data to quantify Cu contamination. When using Cu ions to

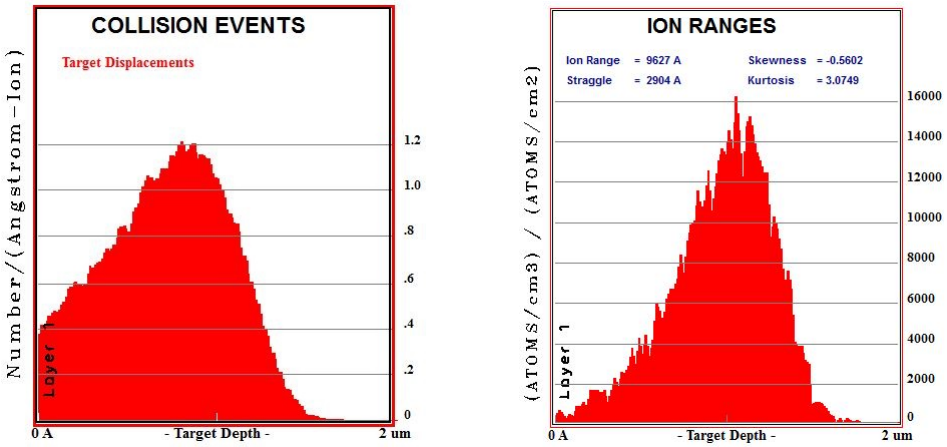

(a) (b)

Figure 3.5: SRIM histogram outputs resulting from 5000 simulation ions of 5 MeV Cu on a W target. The collision events (a) are used for dpa calculation, and the ion ranges (b) are used to estimate the amount of Cu contamination after irradiation.

irradiate a W target, the amount of Cu contamination is a concern because we want to study how pure W responds to plasma exposure after displacement damage. Our W samples, however, do have 10 ppm Cu intrinsic impurities associated with the manufacturing process [66]. Chapter 5 will present data showing that if the added contamination is of the same order of magnitude as the intrinsic Cu contamination or lower, then D retention is unaffected by the additional contaminants.

3.2.3 PISCES steady-state plasma devices

The experiments in chapters 4-5 used the Plasma-Surface Interaction Experimental Station A (PISCES-A) for plasma exposures [74]. A layout of the device is given in figure 3.6. The vacuum chamber is a ∼1.5 m long by 20 cm diameter cylinder. A uniform magnetic field 0.08 to 0.24 T contains a cylindrical plasma up to about 10 cm in diameter. The plasma is created in the source region by reflex arc discharge, driving a current from the negatively biased LaB_6 cathode disk - heated to emit electrons and ionize the gas injected near the source

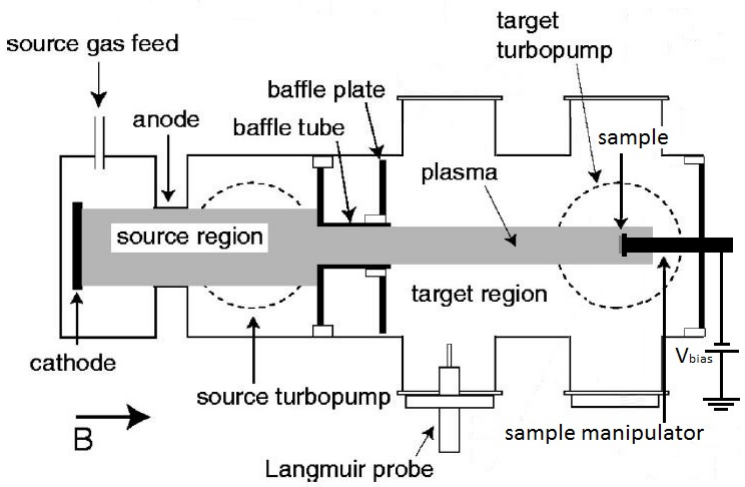

Figure 3.6: Schematic of the PISCES-A plasma device, showing the source region, the target region, and the probe and sample locations.

- to the grounded anode ring downstream. A 4.8 cm diameter floating Cu baffle tube allows gas pressure in the target chamber to vary from 0.1-4 Pa while source conditions remain constant. Electron densities can range $10^{18\text{-}19}$ m^{-3}, and electron temperatures are typically 5-7 eV. The target at the end of chamber can be negatively biased so that ions will be accelerated by its sheath potential and impact the target with high energies. We can estimate ion energies impinging on the target by subtracting the bias of the target from the plasma potential, which is typically 10-20 eV. Characterization of PISCES plasmas has shown that target gas pressures less than 0.67 Pa, which is the operating pressure range in these experiments, produce predominantly molecular ions D_2^+ or H_2^+ [75]. Ion fluxes measured by a swept Langmuir probe in front of the target remain constant at $1.5\,(\pm 0.3) \times 10^{22}$ ions/m^2/s over the entire operational time. The target is heated by the plasma and cooled by pressurized air contained within the sample manipulator. Sample temperatures are measured with a thermal couple pressed to the back sided of the sample, isolated from the plasma.

Controlled sample temperatures around 370 K were achieved using the MORI^{TM}-200 plasma device after adapting its silicon wafer handling stage to accommodate our small W samples [76]. Experiments in chapters 6 and 7 used this plasma etcher, referred to here as "PISCES-E", to obtain lower sample temperatures and lower fluxes. PISCES-E is shown schematically in figure 3.7. Plasmas are created with a helicon wave excited by the radio frequency (rf) antenna wrapped around the bell jar at the top of the device. Diverging magnetic field lines draw the plasma down into the field-free target/process chamber below, impacting the negatively biased stage and sample. The 1200 W input power to the antenna and 0.35 Pa neutral D_2 (or H_2) pressure in the target chamber results in constant plasma parameters for the entire exposure: electron densities in the 10^{16} m^{-3} range, electron temperatures around 5 eV, ion fluxes in the 10^{20} $m^{-2}s^{-1}$ range, and plasma potentials around 15 eV. These plasma parameters were measured by sweeping a Langmuir probe in front of the sample. PISCES-E samples are heated by the plasma and cooled by pressurized air insided of the sample manipulator. Sample temperatures are measured with a thermal couple that is isolated from the plasma and pressed against the back side of the sample.

Plasma densities, energies, and fluxes were based on Langmuir probe measurements. The Langmuir probe sweeps through negative to positive voltages with a function generator and collects plasma currents that diagnose various plasma parameters. The basic physics are as follows. At large negative voltages, the ion current collected by the probe reaches a saturation value called the ion saturation current. This means that the ions form a Debye sheath around the probe to shield the probe's negative potential so that the drift velocity of ions, u_i, passing through the sheath must satisfy the Bohm criterion, $u_i > \sqrt{\frac{T_e}{m_i}}$ [12]. Here, T_e is the electron temperature in energy units, which is assumed to be much greater than the ion

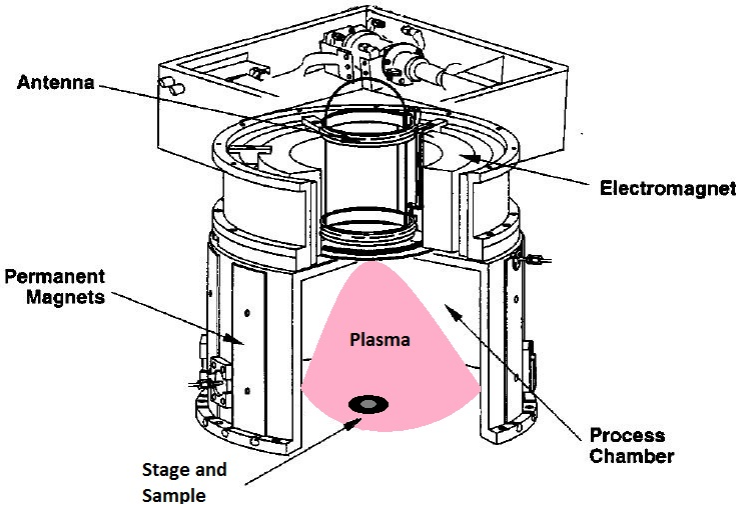

Figure 3.7: Schematic view of the MORI^{TM}-200 plasma etcher, "PISCES-E". The antenna at the top of the device excites a helicon radio frequency (rf) wave that produces plasma, guided axially downward by diverging magnetic field lines into the field-free process chamber where the plasma impacts a biased stage and sample.

temperature, and m_i is the ion mass. The ion velocity at the sheath edge is given by the Bohm sheath criterion to be given as $\sqrt{\frac{T_e}{m_i}}$. The ion saturation current is then calculated by the charge density multiplied by this velocity

$$j_i = 0.6 n_e A e \sqrt{\frac{T_e}{m_i}}, \tag{3.2}$$

where the 0.6 factor comes from the drop in the ion density in the pre-sheath region [12], n_e is the electron density and Ae is the total collected charge over the area, A, of the probe tip. The ion flux reported in these experiments was taken to be the ion saturation current. Making the voltage more positive increases the electron current to the probe (see fig 3.8b). Assuming the electrons have a Maxwell-Boltzmann distribution, the current of electrons to the probe is given by

$$\begin{aligned} j_e &= 0.6 n_e A e \sqrt{\frac{T_e}{2\pi m_e}} \exp\left(\frac{-eV}{T_e}\right) \\ &= j_i \sqrt{\frac{m_i}{2\pi m_e}} \exp\left(\frac{-eV}{T_e}\right). \end{aligned} \tag{3.3}$$

Therefore the total current collected by the probe at any voltage is the sum of the ion and electron currents

$$j = j_i \left(-1 + \sqrt{\frac{m_i}{2\pi m_e}} \exp\left(\frac{-eV}{T_e} \right) \right), \tag{3.4}$$

where we have used the convention that the current from the probe into the plasma is positive.

At large negative voltages, the potential drop across the sheath, V, is large so that the current measured, j, from equation (3.4) gives the ion saturation current, j_i (see figure 3.8a). At large positive voltages, the sheath is nearly stripped away when probe potential is greater than the plasma potential so that electrons are no longer reflected away from the probe. This is where the current begins to saturate (see figure 3.8b green line). In between these two saturation regimes, the slope of equation (3.4) provides the electron temperature, T_e (figure 3.8b red line). The electron density can now be calculated with equation (3.2). We calculate the plasma potential as the voltage where electron saturation begins to dominate. This is taken to be the intersection of equation (3.4) and the electron saturation current (figure 3.8b dashed line).

3.3 Retention data acquisition and analysis

After W samples have been exposed to plasma, we measure the retention properties of D atoms (as well as H atoms in some cases). We have two techniques that independently measure the total amount of retention, but both techniques also provide unique insights into retention properties. Nuclear reaction analysis (NRA) probes from the surface into the first $\sim$10 μm of the sample to give the D concentration profile versus depth. This can provide a quantitative measure of

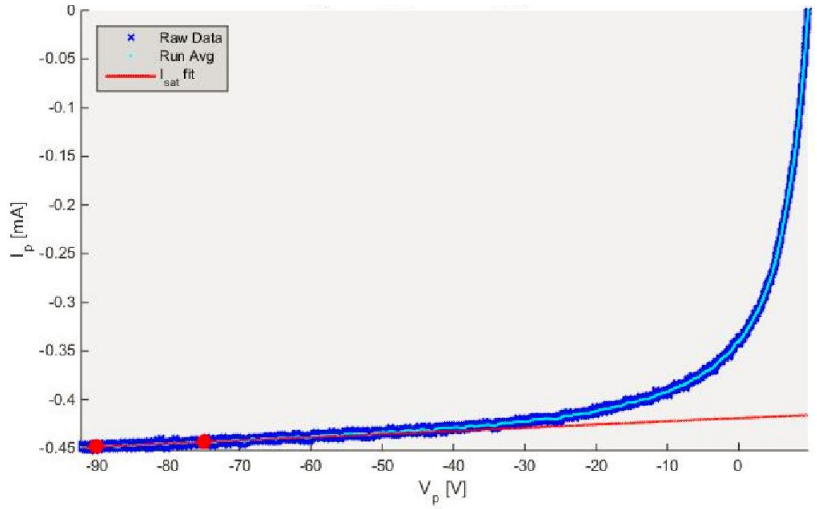

(a)

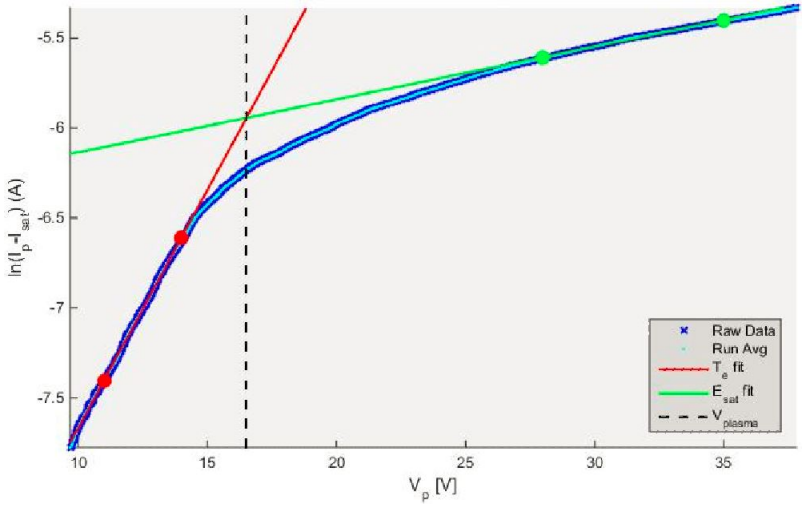

(b)

Figure 3.8: Raw data taken by a Langmuir probe (in blue) with inferred values from fitting the data (straight lines). The figures show a typical ion saturation current at negative voltages (a) as well as the change of the current as the voltage increases to larger positive values (b), where information about the electron temperature, electron density, and plasma potential is gleaned.

the atomic D diffusion in W after plasma exposure. NRA is a non-destructive diagnostic [77], which means very little of the retained D was affected by this measurement. Thus the same sample can be subsequently measured by thermal desorption spectroscopy (TDS). In addition to the total retention value, TDS provides qualitative information about the energy of the D trapping sites in the W sample by the shape of the flux vs temperature profile. This is especially important in chapter 5 when comparing the displacement damage defects created by Cu and W ion beams, which showed the limits of the Cu ion dose before retention is affected by contamination.

3.3.1 Nuclear reaction analysis (NRA)

NRA is a technique that can measure depth profiles of low Z impurities in solids. The experiments presented here probe the depth profiles of D atoms in W specimens using high energy (0.6-4.5 MeV) ^{3}He ion beams. When the ^{3}He ion overcomes the Coulumb barrier and hits the nucleus of target atom, D, this newly formed nucleus is in an excited state and decays into a more stable nucleus, ^{4}He, emitting a proton. This nuclear reaction is usually written as D(^{3}He,p)^{4}He. Knowing the incident ion fluence, the number of measured protons should be proportional to the number of D atoms in the sample. By analyzing the kinematics of the system, the energy of the measured protons also reveal the depth from which the reaction took place so that a depth profile can be determined. Since this measurement relies on the measurement of emitted particles out of the material, reliable measurements can only be taken near the surface of the material up to several microns [78].

Reaction kinematics are key to determining the depth profile. The energy released from the nucleus going from its excited state decaying into its ground

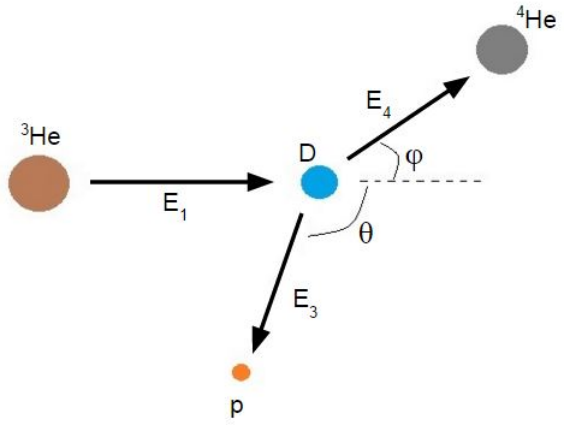

Figure 3.9: Diagram of the D(^{3}He,p)^{4}He reaction collision. The ^{3}He and D nuclei combine then decay into a ^{4}He nucleus, emitting a proton.

state can be calculated from Einstein's $E = mc^2$ and is referred to as the Q-value of the reaction. This Q-value is a constant that is useful in balancing the kinetic energies of the emitted particles (see figure 3.9)

$$E_1 + Q = E_3 + E_4 = E_T, \tag{3.5}$$

where E_1 is the energy with mass M_1 of the impinging particle (i.e. ^{3}He), E_3 is the energy with mass M_3 of the emitted particle (i.e. proton), E_4 is the energy with mass M_4 of the recoiling nucleus (i.e. ^{4}He), and E_T is the total energy. Using equation (3.5) and momentum conservation with these energies and masses, along with the angles described in figure 3.9, we can derive the energy of the emitted particle with respect to the total energy [79]

$$\frac{E_3}{E_T} = A\left[\cos\theta \pm \sqrt{\frac{B}{A} - \sin^2\theta}\right]^2 \tag{3.6}$$

with

$$\begin{aligned} A &= \tfrac{M_1 M_3}{(M_1+M_2)(M_3+M_4)}\tfrac{E_1}{E_T} \\ B &= \tfrac{M_2 M_4}{(M_1+M_2)(M_3+M_4)}\left(1 + \tfrac{M_1 Q}{M_2 E_T}\right), \end{aligned} \tag{3.7}$$

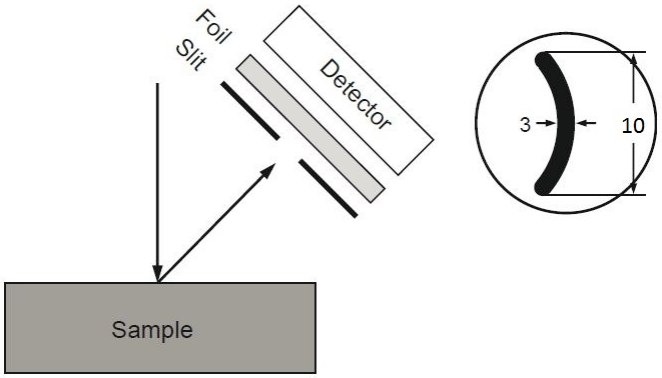

Figure 3.10: Detector set-up for NRA experiments [81]. A schematic of the detector positioning relative to the sample is shown on the left, and a face-on view of the slit aperature is shown on the right with units in mm.

where M_2 is the mass of target atom (i.e. D). The incident ^{3}He ion loses energy through collisions as it travels into the material. Therefore, the measured proton energy will differ depending on the ^{3}He energy. The change in energy of the emitted proton with respect to depth is defined

$$\frac{dE_3}{dx} = N\epsilon_{\mathrm{nr}}, \tag{3.8}$$

where N is the density of the material and ϵ_{nr} is the effective nuclear reaction stopping cross-section that is proportional to the sum of the stopping cross-sections of the incoming particle and emitted proton [78]. For non-resonant NRA equation (3.8) simplifies to the difference in energy of the measured proton emerging at depth, x, from the energy of a proton created at the surface

$$E_{3,\mathrm{measured}} - E_{3,\mathrm{surface}} = xN\epsilon_{\mathrm{nr}}. \tag{3.9}$$

The stopping cross-sections for the D(^{3}He,p)^{4}He reaction at $\theta = 135^o$ have been analyzed by [80], so the relationship between measured energy and depth is established.

The tandem accelerator at LANL irradiated the damaged and D^+ plasma implanted W samples with ^{3}He ions in the general purpose analysis chamber (figure 3.2C). Proton energy spectra, $E_{3,\text{measured}}$, were measured with a 300 mm^2 aperature 2 mm thick Si surface barrier detector at a 135^o scattering angle and 45 mm away from the sample (figure 3.10). A 12 μm thick Al foil was placed in front of the detector to stop elastically scattered ^{3}He ions, and a 3 mm curved slit aperature in front of the detector reduced measurement errors due to geometrical straggling [81]. In addition to the geometrical straggling occuring largely in the top 250 nm, the experiments in [81] have noted that there is an energy spread for $E_{3,\text{measured}}$ largely due to multiple small angle scattering of the incoming ^{3}He ions for larger depths in W. To decrease this energy spread, multiple ion energies were used to produce mulitple proton spectra. Deconvolving these spectra provide better resolution of $E_{3,\text{measured}}$ as we have scanned the optimal (i.e. maximum) stopping cross-section deeper in the material with increasing ^{3}He ion energy. In our experiments, we chose seven energies ranging from 0.6-4.5 MeV to probe up to ~ 8 μm in depth, resulting in depth resolutions better than 1 μm.

The proton spectra resulting from the D-^{3}He reaction were simulated with the SIMNRA v6.80 software [82]. In this analysis, the simulated target is divided into thin slabs of uniform impurity concentration and constant cross-section/stopping power. By changing the compositions in each layer and taking the experimental set-up, ion fluence, and reaction kinematics - equations (3.6) and (3.9) - into account, the simulated spectra can be fitted to the data. The concentrations in these layers are the resulting depth profile of D in W. Samples of typical proton spectra measurements are shown in figure 3.11 for two different ^{3}He ion energies, where the measured proton energy spectra are the red curves and the simulated specta are the blue curves. By simulating the spectrum of a standard sample with known

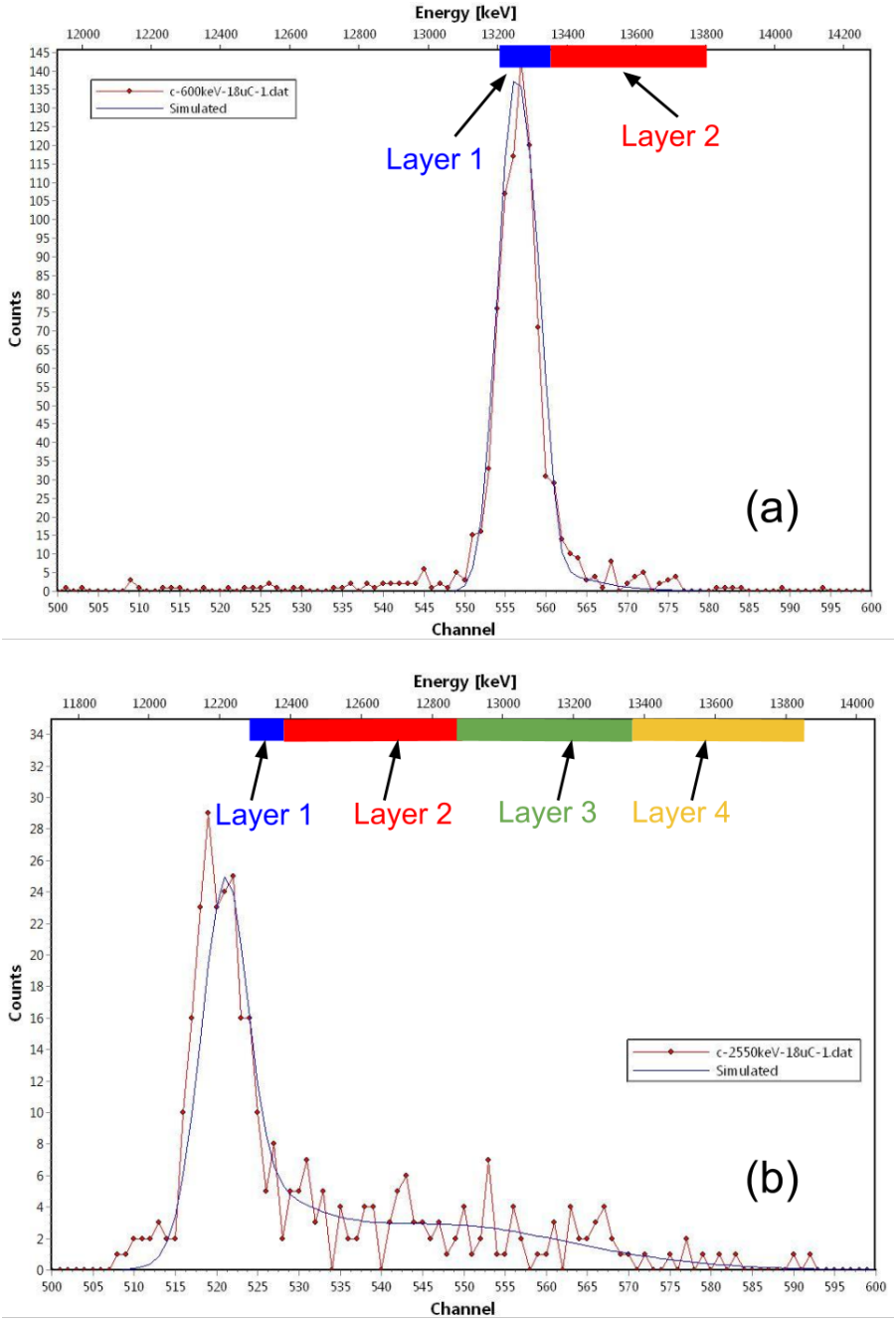

Figure 3.11: Measured (red points) and simulated (blue curve) proton spectra from a 600 keV (a) and a 2550 keV (b) ^{3}He ion beam on a D plasma exposed W sample. The layer (depth) of origin of the measured protons with their respective energies are indicated by the highlighted regions on the upper x-axis. Spectra were simulated with SIMNRA v6.80 software [82].

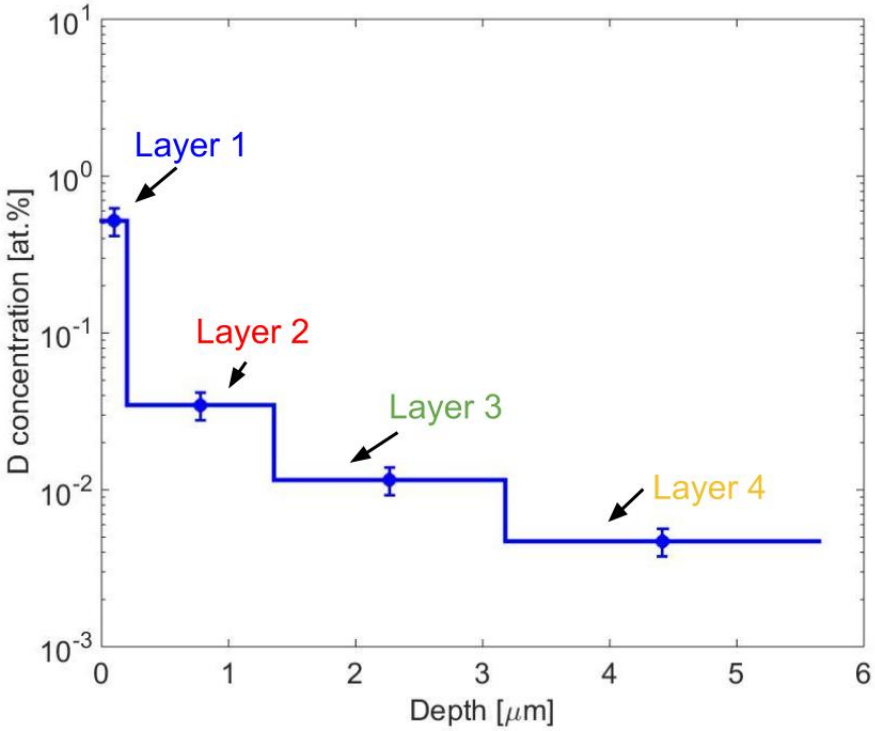

Figure 3.12: Resulting NRA concentration profile, after fitting the proton spectra as in figure 3.11.

thickness and uniform D concentration, the channel axis (lower x-axis) can be directly converted to energy (top axis). We used an amorphous C sample 264 nm thick with a uniform 35 at.% concentration of D. The layer (depth) of origin of the measured protons with their respective energies are indicated by the highlighted regions on the upper x-axis of figure 3.11, which illustrates the need to use larger ion energies in order to measure the concentrations of D at greater depths. The simulated proton spectra in our W samples can be made to have the same counts as the measured data by changing the composition in each layer. After fitting the proton spectra resulting from each ^{3}He energy with the same D compositions, the most accurate depth profile was deconvolved (figure 3.12).

3.3.2 Thermal desorption spectroscopy (TDS)

The TDS technique liberates D atoms trapped in W lattice defects by heating the W sample in vacuum and measuring the partial pressures of D_2, HD, and H_2 molecules that desorb out of the sample. When the thermal energy of the sample becomes comparable to the binding energy of a D (or H) atom to a trapping site, the trapped atom goes into solution and diffuses to the surface where it can find another D (or H) atom to form a molecule and evaporate [83]. The temperature is ramped up slowly so that the entire sample reaches an equilibrium temperature for each measurement. Then it is assumed that the change in partial pressure (i.e. flux out of the sample) of the measured molecules correlates with the temperature with which the atoms are released from trapping sites. This gives a qualitative description of the energies and densities of trapping sites in the W samples. After ramping the temperature up until the partial pressures return to background levels, integration of the partial pressure (i.e. molecular flux) profile gives the total retention value.

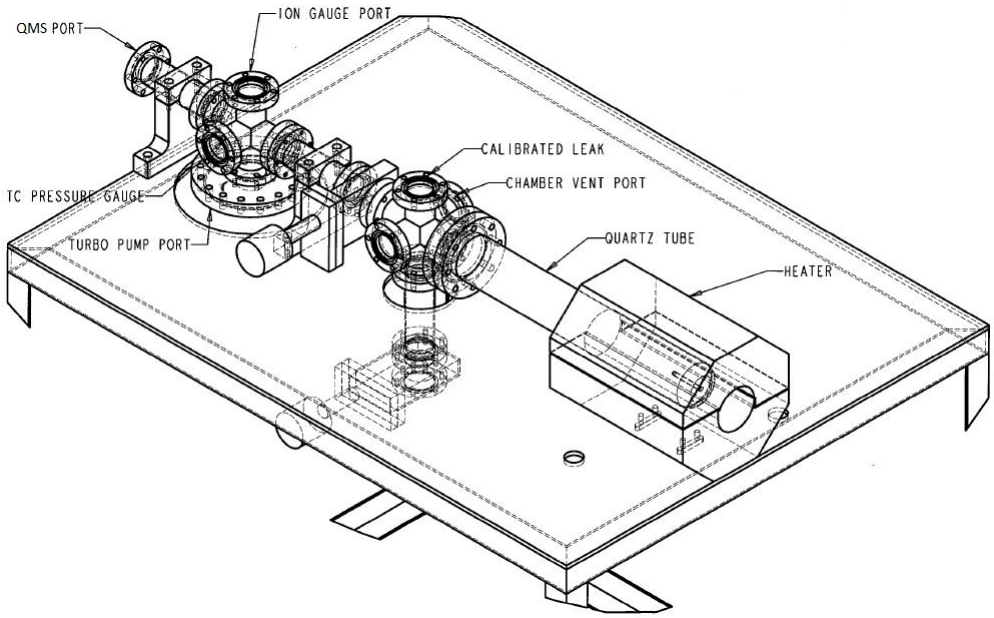

Figure 3.13: Experimental set-up for thermal desorption spectroscopy. Samples are placed in vacuum within the quartz tube, surrounded by the infrared light heater. The partial pressures are measured at the end of the vacuum chamber with a QMS and is calibrated by a standard D_2 leak.

A schematic of the TDS hardware is given in figure 3.13. The W sample is heated from room temperature to 1273 K with an initial background pressure of 4×10^{-5} Pa at 0.5 K/s with infrared heating lamps outside of the quartz tube vacuum chamber. Sample temperature is measured with a thermal couple in vacuum sitting next to the W sample. A MKS instrument^{TM} quadrupole mass spectrometer (QMS) measures the partial pressures of molecular H isotopes throughout the temperature ramp. We calibrate the QMS after each experimental campaign with a standard D_2 leak in mols/s at the same background pressure. This calibration allows us to convert partial pressure into flux.

Accounting for the area of the sample and using the D_2 and HD data, a D atom flux can be measured versus the sample temperature (figure 3.14). The flux peaks at 500 K and 800 K qualitatively describe two dominant trapping energies or possibly two clusters of trapping energies with nearly the same value. The

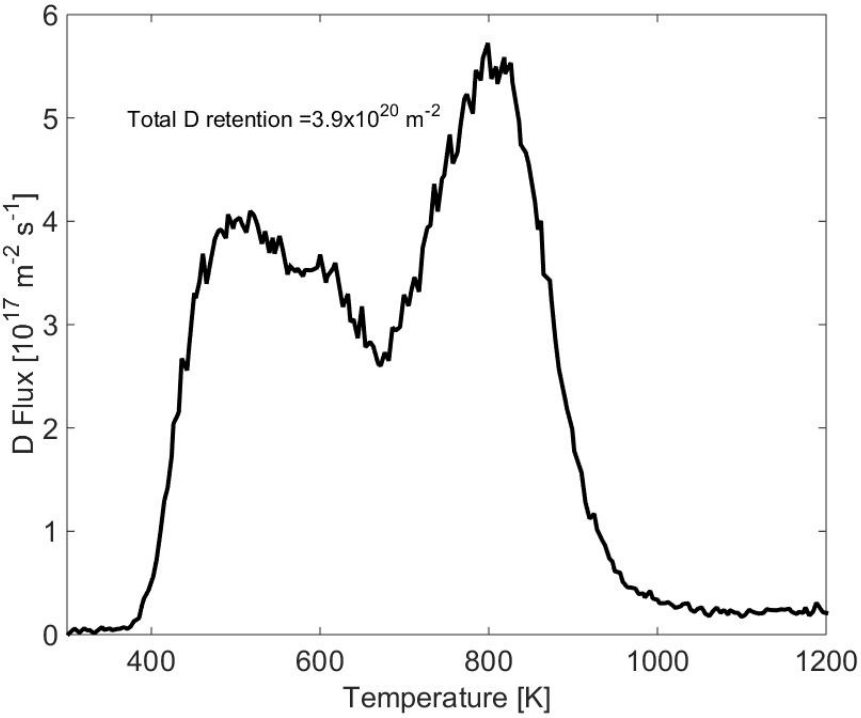

Figure 3.14: A TDS profile with two predominant flux peaks. This W sample was damaged with Cu ions to 0.1 dpa and exposed to D plasma to a fluence of 10^{24} ions/m^2.

amplitude of these peaks describe the trap density differences due to the amount of D released. Since the temperature is increased at a controlled rate of 0.5 K/s, we can integrate the flux over temperature to obtain the total fluence (m^{-2}) of atoms out of the W sample, which gives the total amount of D retained.

Chapter 4

Initial isotope exchange experiments in displacement damaged tungsten

4.1 Introduction

As long pulse torroidally confined plasma devices such as ITER and DEMO edge closer, tritium inventory in the walls raises radiation safety concerns because of increased radioactive inventory in plasma facing components (PFCs) [11, 84, 85]. Isotope exchange has been proposed as a removal technique in W [49]. It can be studied by exposing a metal surface to a D plasma and then subsequently exposing the same sample to H plasma. Some of the H atoms will then displace trapped D atoms which then diffuse out to the surface and escape. In this chapter, the goal of these isotope exchange experiments is to gain an understanding of how implanted isotopes move through trap sites in the material and/or can be exchanged out of the material, which may lead to an increase in the operational time before a major component exchange is necessary.

In a working fusion reactor, 14.1 MeV neutrons can impact the walls causing atomic displacement damage cascades throughout the material. Enhanced

hydrogen isotope retention and degraded material properties have been observed as a result of neutron bombardment [85, 57, 58, 86, 62, 87, 88]. Because energetic neutron irradiation is not possible with present facilities and handling activated samples is difficult, heavy ion beams have been used [62, 61, 89, 63, 90] to simulate neutron induced displacement damage effects. Note that neutrons can cause defects throughout the material [62]; whereas, heavy ion irradiation only affects the first few microns of the exposed surface. But the increase in defects and trap sites for implanted H isotopes due to heavy ion irradiation adds an interesting and realistic complication to retention in PFCs.

In this chapter, PISCES-A was used to investigate H isotope exchange in W with low-energy (100 eV) and relevant flux ($>10^{22}$ ions/m^2/s) plasmas at low temperatures while varying H fluence and ion irradiation damage levels.

4.2 Experimental

4.2.1 Materials

The materials used in these experiments were polycrystalline Plansee ITER Grade W samples 6 mm in diameter and 2 mm thick. The surfaces were mechanically polished to a mirror finish, and then the samples were cleaned in an acetone ultrasonic bath and annealed at 1273 K for 1 h to decrease the amount of intrinsic defects and remove impurities from the surface region.

4.2.2 Damage production in W through Cu ion irradiation

The tandem ion accelerator at Ion Beam Materials Laboratory (IBML) in Los Alamos National Laboratory (LANL) was used to produce irradiation damage in room temperature W by exposing samples to a 2.5 MeV Cu^{2+} ion beam. The

ion fluences used for irradiation in W were 1.25×10^{18}, 1.25×10^{19}, and 1.25×10^{20} Cu^{2+}/m^2. These fluences correlate to 0.4, 4, and 40 dpa (displacements per atom), respectively, by peak damage concentrations calculated with

$$\mathrm{dpa}_{\mathrm{peak}} = \frac{N_{\mathrm{displacement}}\phi}{N_{\mathrm{W}}}, \tag{4.1}$$

where $N_{\mathrm{displacement}}\left(\frac{1}{\mathrm{ions}\cdot m}\right)$ is the peak number of displacements per Cu ion, $\phi\left(\frac{\mathrm{ions}}{m^2}\right)$ is the Cu ion fluence, and $N_{\mathrm{W}}\left(\frac{\mathrm{at}}{m^3}\right)$ is the atomic density of W. The number of displacements were calculated by the SRIM-2012 simulation code [70] with the "full damage cascade option" and a displacement threshold energy in W of 90 eV, as recommended in [71], which resulted in a Cu implantation depth of 520 nm. The SRIM damage profile and ion range profile of 2.5 MeV Cu in W is shown in figure 4.1. A more detailed discussion of the SRIM model was given in section 3.2.2. The impurity level of Cu in W was calculated to increase to nearly 0.004, 0.04, and 0.4 at% near the peak damage region for the three levels of increasing Cu ion fluence. The highest Cu impurity level may have affected D retention, but the data below suggest larger trap densities play a more important role in retention.

4.2.3 Plasma treatment

Both Cu ion beam displacement damaged as well as undamaged W samples were bombarded with D plasma to a fluence of 10^{26} ions/m^2 to saturation [91], where retention reaches a maximum value. Undamaged samples were subsequently exposed to H plasma fluences of 0, 8.4×10^{23}, 6.6×10^{24}, 5×10^{25}, and 10^{26} ions/m^2 and Cu irradiated samples had H plasma fluences of 0, 5×10^{25}, and 10^{26} ions/m^2. Fluxes in PISCES-A for both plasma species were 1.5 ($\pm$0.3) $\times$ 10^{22} ions/m^2/s. The beam diameter is greater than 4 cm, so we expect radial uniformity on our 6

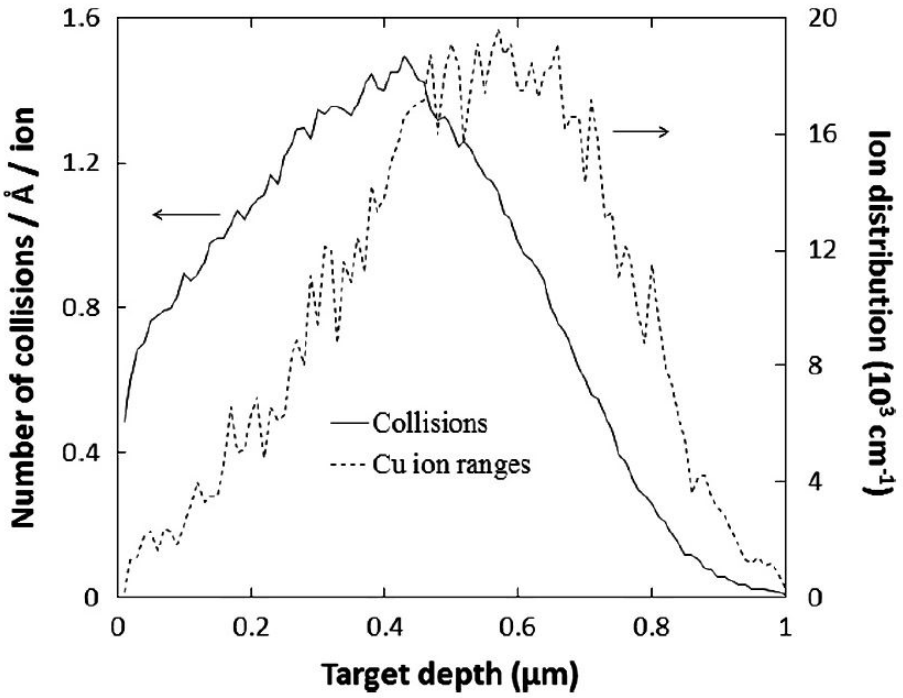

Figure 4.1: SRIM-2012 simulation of depth resolved collision events and ion ranges of Cu in W.

mm diameter samples. All experiments were conducted using ion energy of 100 eV per D_2^+or H_2^+. The ion energy was calculated by subtracting the bias of the target (-110 V) from the plasma potential measured from a swept Langmuir probe. Note that the dominant species in our experiments with neutral gas pressures below 0.67 Pa are molecular ions [75]. The temperature of our samples was measured with a thermocouple pressed against the non-plasma facing side. We performed plasma exposures using temperatures below 373 K, decreasing the complications of enhanced blister formation. We certainly cannot avoid blister formation, even at the low temperatures of our experiments [26]. But we want to emphasize the focus these experiments on the behavior of atomic D to simplify the problem as much as possible.

4.2.4 Deuterium retention measurements

After the plasma exposures, concentration depth profiles of D in W were obtained with nuclear reaction analysis (NRA) up to 3.5 μm by the D(^{3}He, p)^{4}He nuclear reaction with a constant 2.5 MeV ^{3}He ion beam normal to the surface of the sample. The measured energy of protons that escape through the surface determines the depth into W from which the reaction took place [92], details of which are provided in the discussion of the NRA technique in chapter 3. A 2 mm thick Si surface barrier detector, with a 300 mm^2 aperture and 46.5 mm from the sample at a 30 degree angle relative to the beam, was covered by 12 μm thick Al foil to stop elastically scattered ^{3}He particles to isolate the proton energy measurement. Because we see a drastic difference between near surface inventory and bulk inventory, we focused our attention to these two regions. Analysis software SIMNRA [82] was employed to convert the yield versus energy spectra given from the detector into concentration versus depth profiles using two equally spaced W/D layers over our measurement range of 3.5 μm. The first layer we will call the "surface region", and the other the "bulk region".

After NRA, total D retention in the W was measured *post mortem* with thermal desorption spectroscopy (TDS). Each sample was heated from room temperature to 1273 K in vacuum with a background pressure of 4.1×10^{-6} Pa at 0.5 K/s with infrared heating lamps. A quadrupole mass spectrometer (QMS) tracked the signals of D_2 and HD molecules as they were released from the sample. The QMS was calibrated by a standard D_2 leak after each analysis.

4.3 Results and discussion

Concentrations of D in W from NRA are shown in table 4.1, and TDS bulk retention measurements are shown in figure 4.2. Both measurements are in good agreement. Undamaged samples (0 dpa) exposed to five different doses of H, including no H exposure, have significantly different depth profile retention characteristics. We suspect that the saturation of the surface region is the reason we see a higher percentage of D there. This saturation probably occurs in the first few hundred nm [49] of the 0 H ions/m^2 profile where close to all trap sites are filled with D [91]. Since our NRA does not show an equal distribution of D in both the "surface region" layer (0-1.75 μm) and the "bulk region" layer (1.75-3.5 μm), the D profile beyond the surface layer must be a result of diffusion during the 2 hour D plasma exposure in PISCES. As a result, the surface region inventory is depleted more quickly during isotope exchange because H atoms can diffuse to a trapping site and exchange with D in the surface region sooner than diffuse to a D filled trapping site in the bulk region. The D concentration in undamaged W was eventually depleted beyond the NRA detection limit after an H fluence of 5×10^{25} ions/m^2. The bulk retention measurements after 5×10^{25} H ions/m^2 also show that the D signals are within the background noise of the detector, indicating almost all of the D was exchanged out.

When displacement damage is introduced, both NRA and TDS show an increased amount of retained D inventory. Bulk retention (Figure 4.2) shows an increase of 5–7 times more D than the undamaged sample without isotope exchange. The surface region contains most of the D concentration (Table 4.1), even as H fluence increases. This higher inventory is presumably a result of more trap sites created by Cu ion irradiation causing more vacancies and dislocations. Concentrations of D after isotope exchange seem to correlate with the change in the

Table 4.1: D concentrations (10^{20} atoms/m^2) in W calculated from NRA data with varying H fluence and dpa levels. The total D retention (summing both layers defined by the "surface region" and "bulk region"), the D retention in the "surface region" layer, and inventory percentage of the "surface region" layer are tabulated for each scenario.

H fluence (ions/m^2)	0 dpa		0.4 dpa		4 dpa		40 dpa	
	Total	Surface layer	Total	Surface layer	Total	Surface layer	Total	Surface layer
0	1.28	1.01, 79%	7.46	6.96, 93%	9.83	9.73, 99%	10.72	10.50, 98%
8.4E + 23	1.11	0.66, 59%	–	–	–	–	–	–
6.6E + 24	0.25	0.11, 44%	–	–	–	–	–	–
5.0E + 25	0	0, 0%	0.27	0.21, 78%	1.02	0.94, 92%	1.15	1.07, 93%
1.0E + 26	0	0, 0%	0	0, 0%	0.86	0.77, 90%	1.23	1.16, 94%

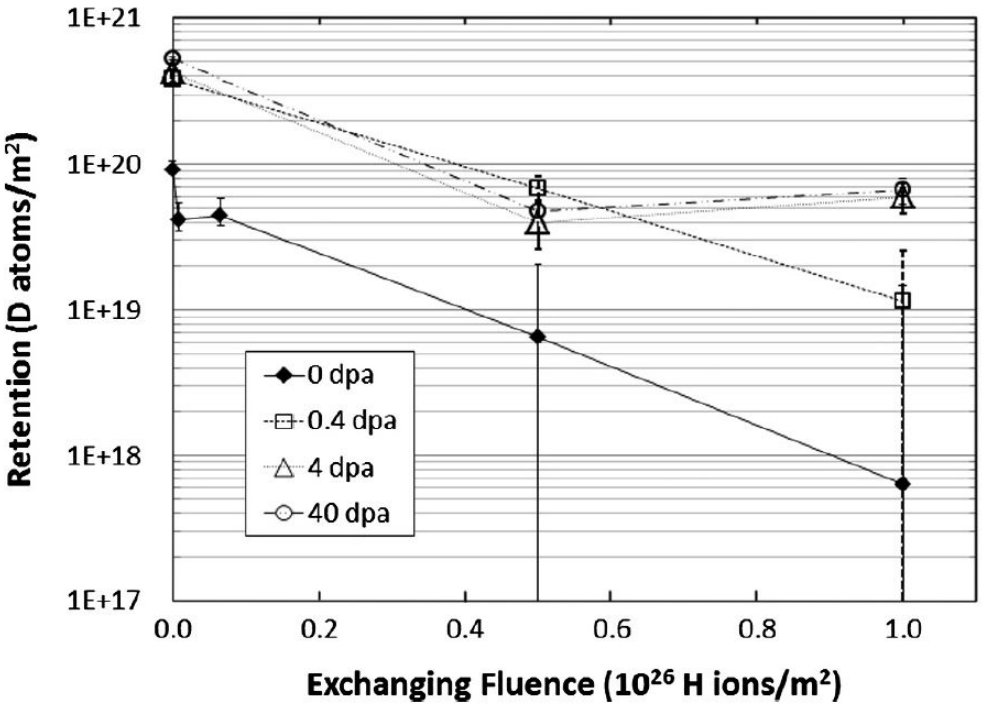

Figure 4.2: Total retention of D as a function of H plasma fluence for each level of damage.

concentrations in the surface region, indicated by the higher fraction of D in the surface region even while the inventory is being depleted. During isotope exchange, displacement damage allows more D to be retained near the surface because the exchanged D atoms can more easily re-trap before diffusing. After 5×10^{25} H ions/m^2, TDS shows an 80% reduction in inventory for all damage levels. It appears that the remaining 20% of D inventory is exchanged out of the 0.4 dpa sample, but with higher damage we were still able to detect measurable amounts of D concentration after high H fluences. The increased number of trap sites in the surface hinders the efficiency of isotope exchange by inhibiting the diffusion of H atoms and by re-trapping the exchanged D. We perhaps would have to expose damaged samples to plasma on even longer time scales to purge the entire D inventory.

Figure 4.3 shows the TDS emission of the undamaged W samples. These results shed more light on how the D inventory is affected by isotope exchange.

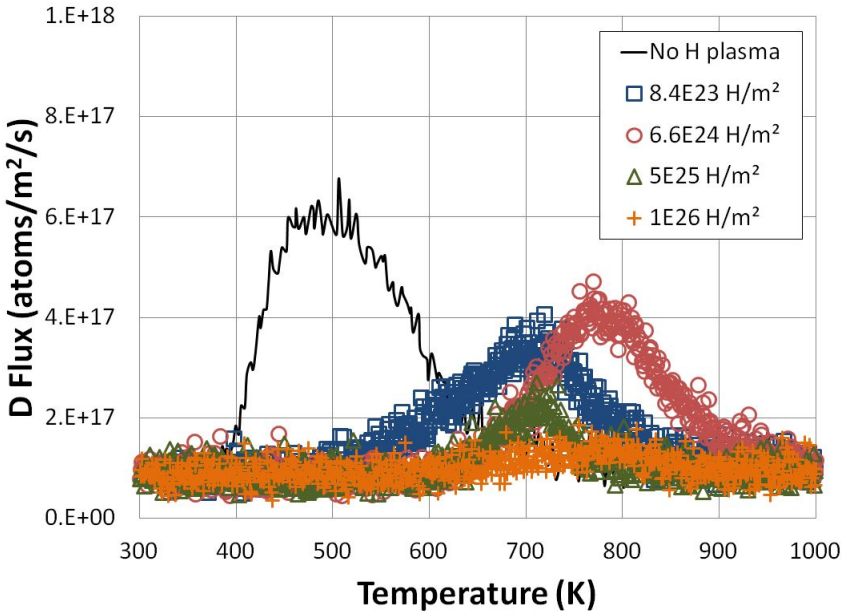

Figure 4.3: Thermal desorption profiles of the undamaged W samples after D plasma treatment and varying doses of H plasma.

Without isotope exchange, the peak desorption occurs around 490 K, and the slope of the curve on the low temperature side indicates that much of the inventory was released quickly, relative to our temperature ramp. On the other hand, the samples with exposures to H plasma have release peaks ranging from 700 to 790 K, and the slopes of these curves on the low temperature side show a slower rate of desorption. Release peaks at higher temperatures may indicate that the released D originated from higher energy traps, and the slower rates of desorption may indicate that the D atoms took longer to diffuse to the surface, originating deeper within the sample. Table 4.1 also indicates that most of the remaining D inventory is in the bulk region as H fluence increases. This would mean that most D atoms have exchanged out of the traps in the surface region during H plasma treatment.

Desorption profiles for each damage level without isotope exchange show rapid release starting around 400 K (Figure 4.4). Irradiated samples, however, have higher temperature release peaks. The release peaks at higher temperature

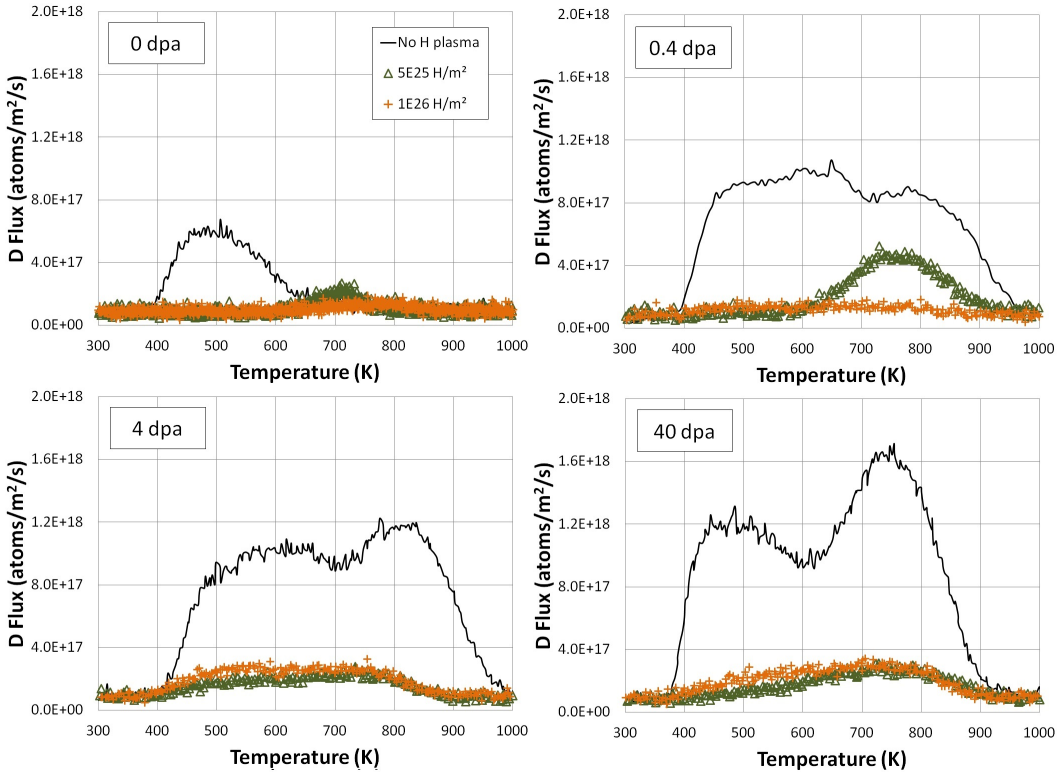

Figure 4.4: Thermal desorption profiles of W after D plasma treatment and varying doses of H plasma for each damage level.

are possibly due to the increase of the number of higher energy vacancy traps caused by the introduction these defects by irradiation. There is a similarity in the 0 and 0.4 dpa samples after the 5×10^{25} H ions/m^2 dose: a release peak at higher temperature and a slower rate of desorption. This may show that D inventory in the 0.4 dpa sample can still easily diffuse deeper within the sample after being exchanged out of traps. This is not inconsistent with table 4.1, since the surface region loses 15% of the total inventory to the bulk after exchange. At higher damage (4 and 40 dpa) with isotope exchange, D begins to desorb at the same low temperature as in the non-exchanged case and seems to desorb at a slow and almost constant rate during the temperature ramp. Most of the D inventory remained in the surface region according to NRA, so this slow desorption rate is probably a result of diffusion being inhibited by a higher density of traps.

4.4 Summary

We exposed undamaged and Cu irradiated W samples at room temperature to low-energy, constant-flux D plasmas at plasma fluences that were sufficient to saturate the samples and sequentially exposed them to H plasma at varying fluences. TDS and NRA data both show that isotope exchange reduces D inventory in W significantly. When displacement damage is introduced in W by way of Cu ion irradiations, concentration profiles of implanted D show that increased retention nearer to the surface is favored over diffusion into the bulk. We see that high damage levels (4 and 40 dpa) tend to keep more of the inventory nearer to the surface and reduce the efficiency of isotope exchange, presumably because of increased trap site densities.

High dpa levels in the W lattice have shown us that isotope exchange is not efficient at removing the entire D inventory. With the combination of the increased number of trap sites and plasma recycling in front of the target (a complication not experienced in ion beam isotope exchange experiments), isotope exchange is too slow a process for practical tritium removal after long exposures to fusion neutrons. However, this initial work suggests that isotope exchange experiments could provide a useful tool to study D trapping in damaged W. In chapter 6, we model NRA data in order to understand how the trapping energies and densities of these traps affect H isotope migration in materials. Higher resolution NRA D profiles that provide more than two layers would quantify this phenomena better.

Acknowledgments

The work in this chapter was supported by the US Department of Energy under DE-SC0001999 and DE-FG02-07ER54912. The ion irradiation and ion beam

analysis work at the ion beams materials laboratory was supported by a LANL new program development grant in support of its MaRIE signature facility. Technical assistance and experimental guidance from M. Baldwin and T. Lynch is gratefully acknowledged.

This chapter, including text and data, is in part a reprint of the material as it appears in J. L. Barton, Y. Q. Wang, T. Schwarz-Selinger, R. P. Doerner, G. R. Tynan, Isotope exchange experiments in tungsten with sequential deuterium and protium plasmas in pisces, J. Nucl. Mater. 438 (2013) S1183-S1186. The dissertation author was the primary investigator and author of this paper.

Chapter 5

Deuterium retention in tungsten after heavy ion damage and hydrogen isotope exchange in PISCES

5.1 Introduction

Tritium retained in the plasma facing components (PFCs) of large magnetically confined nuclear fusion test reactors, such as ITER, pose concerns regarding loss of fusion fuel and radiation safety [11, 84, 85]. Methods to reduce trapped H isotopes have been tested [49, 50, 93] by exposing D doped W materials to H ions in order to see the effect of D displacement. The goal is to preserve the tokamak walls and divertor plates from reaching the tritium contamination limit [34]. However, isotope exchange experiments also provide an interesting new insight into the atomic migration paradigm that trapping effects reduce hydrogenic diffusion.

DT fusion reactions produce 14.1 MeV neutrons, which can impact the PFCs of a working fusion reactor. These high energy collisions cause damage cascades in the lattice that can change the retention properties of the material [59, 62]. Since present facilities available cannot replicate neutron bombardment in a fusion reactor and because handling neutron irradiated samples is difficult, heavy ion beams have been used to mimic neutron damage [59, 62, 90, 60]. However, using ions as surrogates for neutrons do not fully replicate the uniform damage profiles that neutrons can provide, but within the penetration depth of these heavy ions, they model the retention characteristics of damaged PFC materials reasonably well [59]. The other issue with using heavy ions to create damage is that it allows the possibility of impurity build-up in the material. Some experiments have used self-damage, i.e. W ions on W, to avoid contamination [59, 60], but W ions have a very shallow stopping distance in W (about an average of 500 nm with a 6 MeV beam [70]); in addition, creating a W ion beam has complications of its own. Cu ions have been used to create damage in W [93, 62], and they can produce similar damage profiles as W ions. Therefore we want to determine when contamination from impurity Cu ions start to play a role in changing retention characteristics in W.

This chapter again examines H isotope exchange in W by measuring the remaining D retention, but motivated by the results of chapter 4, we made several modifications to the experimental procedures. We simulate realistic material properties after neutron irradiation in a fusion reactor with heavy ion irradiation, but this time we compare Cu ion versus W ion irradiation to see what levels of Cu contamination significantly affect D retention. The plasma exposure temperatures are carried out at 100 K higher than in the results of chapter 4. In addition, we improved the NRA measurement resolution by implementing multiple ^{3}He ion

beam energies. At any rate, the isotope exchange data presented in this chapter are consistant with the D retention characteristics in the "surface region" and "bulk region" defined in chapter 4.

5.2 Experimental

5.2.1 Materials

Plansee [66] polycrystalline W samples 6 mm in diameter and 2 mm thick – machined from W rods – were used in these experiments. The surfaces were mechanically polished to a mirror finish, and were cleaned in an acetone ultrasonic bath. To decrease the amount of intrinsic defects and remove impurities, the samples were then annealed at 1273 K for 1 h.

5.2.2 Damage production in W with Cu and W ions

The tandem ion accelerator at the Ion Beam Materials Laboratory (IBML) in Los Alamos National Laboratory (LANL) was used to produce 2 MeV Cu^{+} and a 6 MeV W^{2+} ion beams to create displacement damage in our W samples. Damage profiles were simulated with the SRIM-2012 simulation code [70], with the "detailed calculation with full damage cascades" option turned on and a displacement damage threshold of 90 eV for W as recommended in [71]. The computed damage profiles and ion stopping ranges are shown in figure 5.1. The left-hand vertical axis shows the distribution of displacements per atom (dpa) from Cu and W ions to produce 1.0 dpa at its peak, and the right-hand vertical axis shows the stopping range of these ions. Peak dpa were calculated in the same way as chapter 4 with equation 4.1. Since Cu ions have significantly lower mass than W ions and therefore have a lower number of displacements per incoming ion, Cu ion fluences

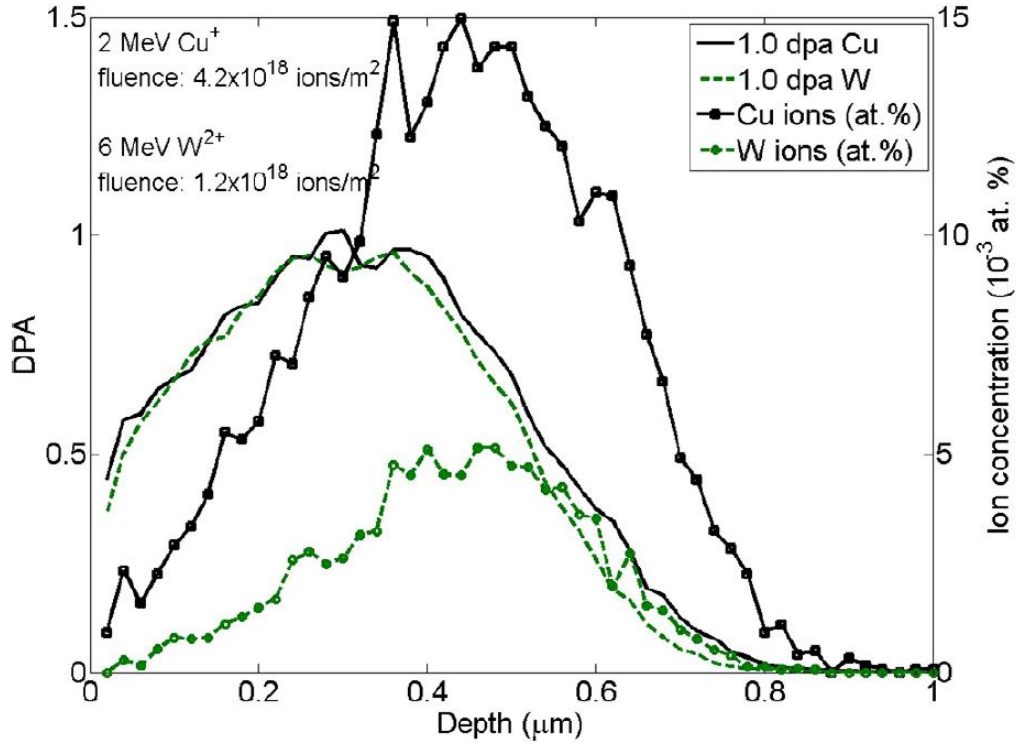

Figure 5.1: SRIM simulated damage profiles and ion concentration in W (90 eV displacement threshold) for 2 MeV Cu and 6 MeV W ions.

had to be increased to 3.5 times the W ion fluence to represent a similar damage profile in order to compare retention characteristics. The ion stopping ranges are quite similar, but it is important to note that Cu contamination occurs only in the first 1 μm. In order to produce 0.01, 0.1, and 1.0 dpa in our W samples, we applied Cu ion fluences of 4.2×10^{16}, 4.2×10^{17}, and 4.2×10^{18} ions/m^2, respectively, where the W ion doses were 3.5 times lower.

5.2.3 Plasma treatment

Undamaged as well as Cu irradiated and W irradiated samples were exposed to plasma in the PISCES linear plasma device at UCSD. Fluxes in the PISCES-A device for both D and H plasmas were 1.5 ($\pm$0.3) $\times 10^{22}$ ions/m^2/s. We expect radial uniformity in the plasma wetted area of our 6 mm diameter samples

because our beam diameter is greater than 4 cm. The ion energies were 150 eV per D_2^+ or H_2^+, calculated by subtracting the bias voltage of the sample holder (160 V) from the plasma potential measured from a swept Langmuir probe. In our experiments, neutral gas pressures entering the vacuum chamber below 0.67 Pa produce molecular D_2^+ ions as the dominant plasma species [75]. We kept the W sample temperature at a constant 473 K, measured by a thermocouple pressed against the sample back side, isolated from the plasma. All samples were treated with D plasma to 10^{26} ions/m^2, which is a fluence well into the saturation regime [38]. Undamaged samples used for isotope exchange were subsequently exposed to H plasma fluences of 2.6×10^{24}, 5×10^{25}, or 10^{26} ions/m^2; and isotope exchange experiments with Cu irradiated samples were also exposed to H plasma to fluences of 5×10^{25} or 10^{26} ions/m^2.

5.2.4 Nuclear reaction analysis and thermal desorption spectroscopy

Profiles of D concentration as a function of depth were obtained by nuclear reaction analysis (NRA) up to 7.7 μm by the D(^{3}He,p)^{4}He nuclear reaction and measurement methods described in [81]. The measured energy of protons that escape through the surface determines the depth into W from which the reaction took place [94]. A 2 mm thick Si surface barrier detector, with a 300 mm^2 aperture and located 45 mm from the sample at a 135 degree scattering angle, was covered by 24 μm thick Al foil to stop elastically scattered ^{3}He particles as well as a 3 mm curved slit aperture, as in [81], to isolate the proton energy measurement. To increase the precision and spatial resolution of our measurements, we used ^{3}He beam energies of 0.8, 2, 2.75, 3.5, and 4.5 MeV, where greater energies provide confidence in resolution at greater depths as the penetration distance of ^{3}He increases

before it reacts with D. The analysis software SIMNRA [82] was employed to fit the yield versus energy spectra to extract concentration versus depth profiles. The simulation inputs assume constant concentration of D per W layer, where each layer thickness can be varied.

The total amount of D retained in W was measured with thermal desorption spectroscopy (TDS). Samples were heated from room temperature to 1273 K at a rate of 0.5 K/s with infrared heating lamps and a background pressure of 1.1×10^{-5} Pa. A quadrupole mass spectrometer (QMS) measured the D_2 and HD pressure signals as the temperature increased and released these molecules from the sample. After each analysis, the QMS was calibrated with a standard D_2 leak to convert the measured partial pressure data to molecular flux. Integrating the signals over the temperature ramp gives the fluence, which is total amount retained.

5.3 Results and discussion

Subsequent exposure of the damaged and plasma-implanted D samples to 150 eV/H_2^+ plasma at various fluences and a 473 K sample temperature decreased the amount of D atoms saturated in the W samples by exchanging H with the implanted D. The concentration profiles in figure 5.2 shows a significant decrease in inventory in the first 2 μm from the surface with increasing fluences of H plasma. Measured D inventory deeper within the bulk also decreases as H atoms diffuse inward and displace the trapped D atoms there. These results are in good agreement with [49, 50], which found the inventory in the first few microns decreasing significantly and concentrations deeper than 3 μm within the sample remaining somewhat unaffected. At the high fluences achieved by this experiment, we can see an interesting phenomena occur. Comparing the D retention profiles of the sample exposed to 3×10^{24} H/m^2 to the sample exposed to 5×10^{25} H/m^2, the

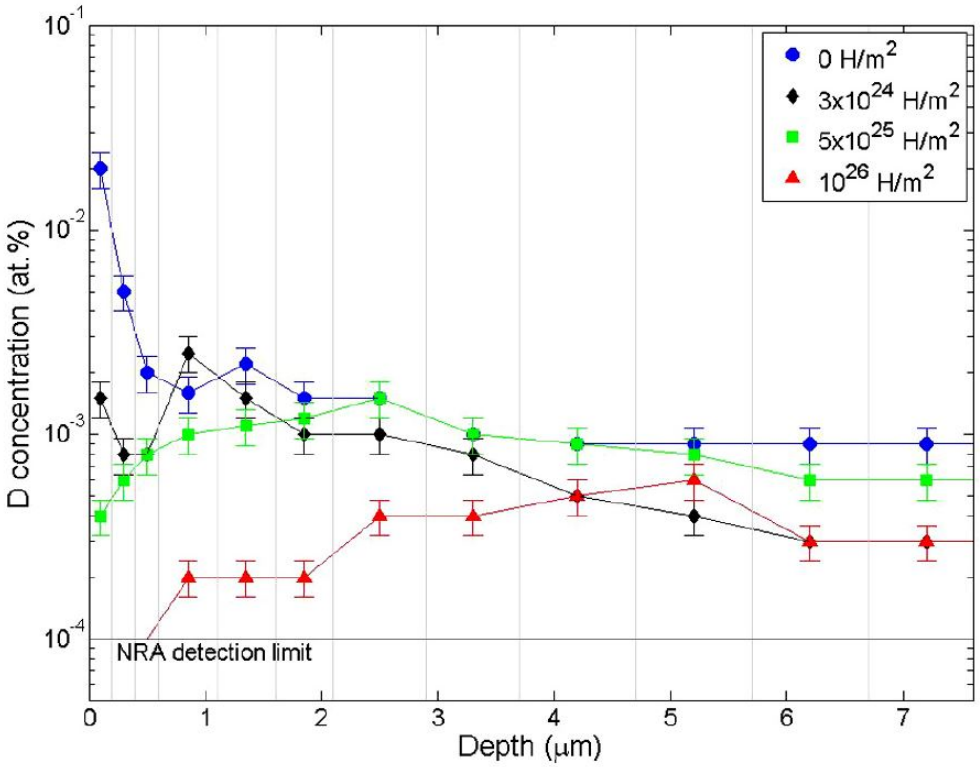

Figure 5.2: Depth distributions of D in W after exposure to 10^{26} D ions/m^2 plasma and various fluences of H plasma. The connecting lines are only to guide the eye, and the grey vertical lines show the thickness of the W layer that was simulated.

increase of D concentration at depths greater than 1 μm as H plasma fluence increases may be an indication that although some D is displaced and migrates to the surface, some of the displaced D migrates deeper into the bulk. This can be seen by the peak of concentration moving inward, where at that same depth the concentration was lower with less exposure to H plasma. But overall, the entire D inventory is reduced with increasing H fluence.

Heavy ion irradiation on W causes an increased number of trapping sites with ion induced vacancies, voids, and interstitials stressing the lattice. Therefore we expected to see an increase in D inventory in our damaged W samples. Figure 5.3 shows a significant increase in D concentrations within the first micron, i.e. the damaged region, but follow a similar trend as the undamaged samples beyond

the damaged region. Even though there is an increase in trapping sites in the material, which may reduce diffusion to greater depths, this saturation condition at high fluences of D plasma can allow diffusion past them.

Damaged samples with H plasma fluences of 5×10^{25} and 10^{26} ions/m^2 could not be accurately measured, possibly because of some experimental limitations. The sample holder for all other samples had broken, so a different sample holder was used for these six samples. This new sample holder is different in that the thermal couple contacts the sample holder and not the samples. It is possible that during the H plasma treatment of these damaged samples that they did not have good thermal contact with the heat sink, and since temperature was measured from the sample holder, accurate sample temperatures may not have been measured. If the sample temperature was higher than reported, diffusion of H isotopes could have been more rapid and could explain the greater decrease in D inventory. Due to more defects in the material as a result of damage, we would have expected less efficient diffusion of H isotopes. These phenomena will be investigated in future experiments.

Looking at figure 5.3, the W ion damage samples seem to be indistinguishable from the Cu ion damaged samples at 0.01 and 0.1 dpa; however, it seems that Cu impurities begin to play a role in affecting retention at higher dpa. There is about 3 times more D in the damaged region of the Cu irradiated 1 dpa sample than the W irradiated 1 dpa sample. The impurity level in this case is 65 atomic parts per million (appm), where the inherent impurity of Cu from the manufacturer is around 10 appm [66]. So it makes sense that we see a change in the attributes of our samples at this high fluence of Cu. High fluences of Cu ions may not even be necessary to mimic W ion damage, since heavy ion induced damage to the lattice may have already reached "damage saturation" around 0.1 dpa [60]. Neutron

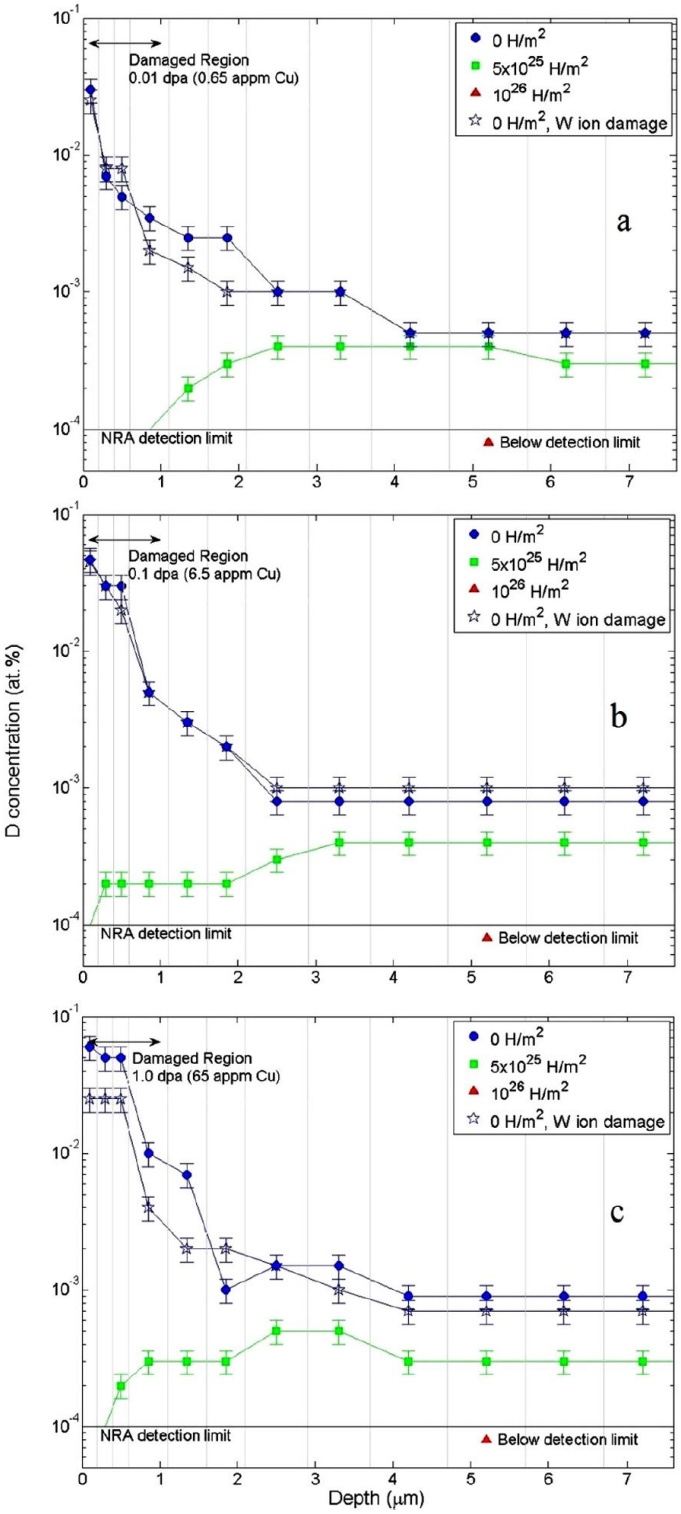

Figure 5.3: Depth distributions of D for (a) 0.01 dpa, (b) 0.1 dpa, and (c) 1.0 dpa in W after exposure D plasma and various fluences of H plasma. Open symbols represent samples irradiated with W ions.

induced damage, however, may not reach this damage saturation because transmutated W atoms could play a role in creating additional trapping sites. Since ion damage does not produce transmutations, this phenomenon is not observed here.

The total amount of D retained as a function of H plasma fluence is shown in figure 5.4. At even lower sample temperature (373 K) where Cu ion damage affects the efficiency of isotope exchange [93], damage seems to have no effect on the efficiency of isotope exchange carried out at 473 K. However, as mentioned above, the temperature measurement may have been compromised on the damaged isotope exchanged samples. The error bars on figure 5.4 represent their signal to noise ratio from the molecular background fluctuations in the QMS. So the large error bars on the high H fluence samples indicate that there is almost no measureable amount of D remaining in the samples. In other words, only trace amounts of D remain after exposure to high fluences of H plasma.

There seems to be little difference in retention of D, when comparing Cu and W ion damage with total retention in figure 5.4. The TDS temperature traces (Figure 5.5) shows similar out-gassing rates of D_2 and HD, except at 1.0 dpa, where again we see that these high Cu contamination levels seem to affect D uptake. The Cu irradiated sample releases D molecules at a lower temperature (energy) and has a broader spectrum than the W irradiated sample at 1 dpa. We can speculate that the Cu contamination produces a wider array of different energy trap sites due to differing amounts of Cu contamination within the damage layers. Thermal desorption from lower temperatures may be from D originating from lower energy traps, and desorption at higher temperatures may be D desorbing after a random walk of escaping from a higher energy trap and falling into other traps until reaching the surface. These TDS spectra also give a surprising result. Although the NRA concentration profiles for the damaged samples show only differences in

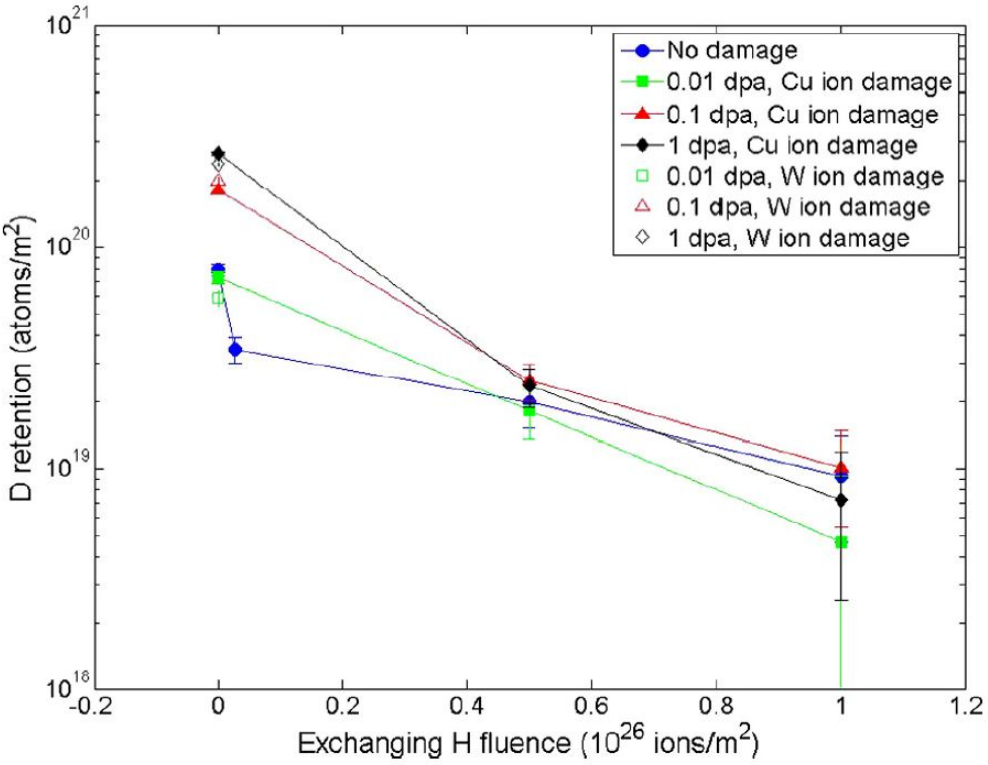

Figure 5.4: Total retention of D as a function of H plasma fluence for each dpa level. Error bars in this case represent the ability to discern the signal from the background fluctuations measured by the QMS.

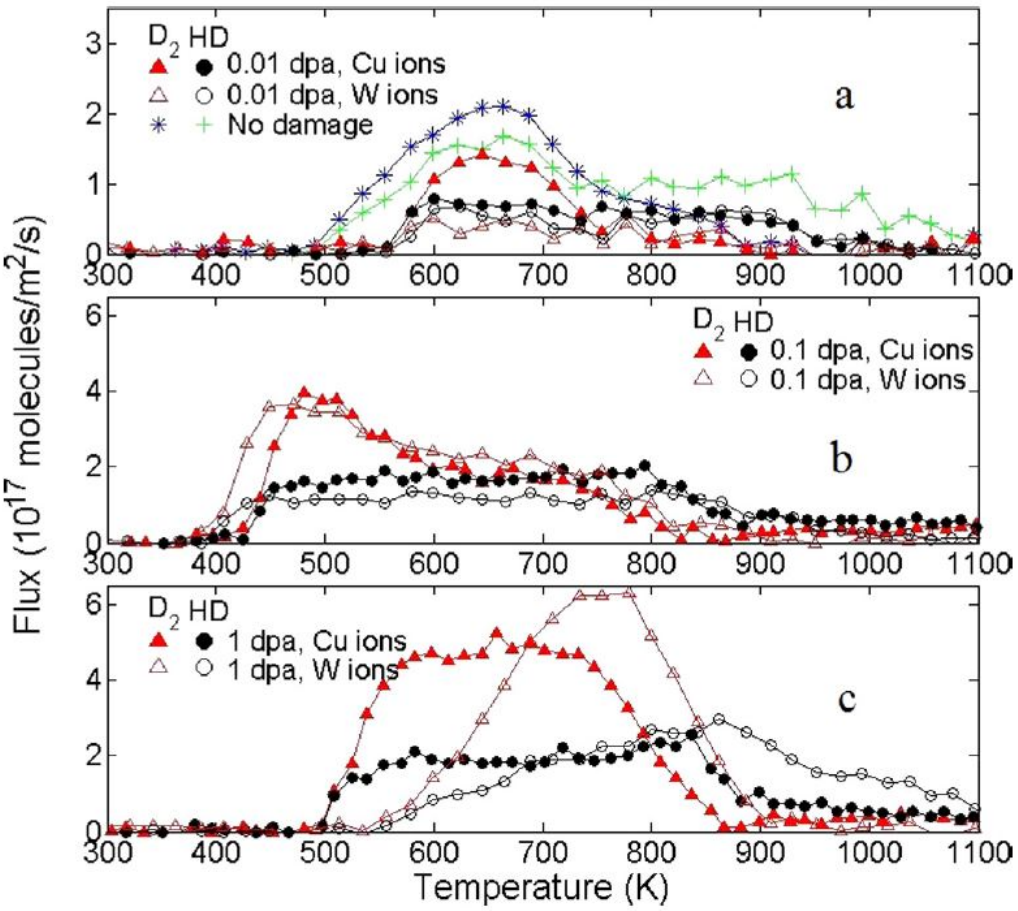

Figure 5.5: TDS temperature traces, after exposure to only D plasma, of the D_2 and HD molecules comparing the molecular release rates due to damage created by Cu or W ions with (a) no damage and 0.01 dpa, (b) 0.1 dpa, and (c) 1.0 dpa.

the amount of D retained as a result of the level of damage they received, the TDS temperature trace profiles vary significantly. The damaged samples had increased D inventory closer to the surface where the damage occurred, so these differing TDS profiles may display changes in the trapping mechanisms as the damage level increases, possibly due to different distributions of atoms in vacancies caused by regions of the lattice that are stressed by interstitials or voids in the lattice [91, 95].

5.4 Summary

W samples were exposed to high fluences of D and H plasmas sequentially after being irradiated by high energy Cu or W ions to varying levels of displacement damage in order to investigate H isotope replacement in W. The higher 473 K plasma exposure temperature of the W samples allowed more rapid diffusion of H isotopes, regardless of dpa level. As a result, the H atoms were able to reduce the D inventory down to trace levels. This observed H exchange efficiency may be due to possible temperature control issues, because higher temperatures could have allowed more rapid diffusion of H and subsiquent isotope exchange in our damaged samples. There seems to be no discernible difference between Cu induced ion damage and W ion damage at 0.01 and 0.1 dpa, where concentrations of Cu are below intrinsic Cu impurity levels. At 1.0 dpa (4.2×10^{18} Cu ions/m^2 or 65 appm in the first 1 μm) Cu contamination affected D concentrations in the damaged region and may have different trapping mechanisms compared to 1.0 dpa W without contamination. Isotope exchange can reduce tritium inventory, but it is expected that tritium can exchange equally as well with other H isotopes and can reestablish itself in W PFCs [50]. We can thus conclude that this method of isotope removal will at least extend operation time before major interventions are needed.

Some models exist, such as [96], which model atomic trapping and diffusion, where atoms are released from traps only by thermal activated release. Currently, no model exists where atomic exchange in trapping sites is taken into account. We (and others [95]) have observed that trapping mechanisms may change with the level of damage in the material, so this atomic exchange from traps may affect the diffusion of H isotopes differently as damage is increased. Understanding the physical process of atomic exchange will not only increase our understanding

of atomic migration in fusion materials but also may provide precision in future modeling endeavors to understand trapping processes. In the following chapter, we introduce a model of the isotope exchange process and compare it to experimental results.

Acknowledgements

This work was supported by the U.S. Department of Energy under DE-SC0001999 and DE-FG02-07ER54912 and the University of California Office of President Research Fund under Award Number 12-LR-237801. The ion irradiation and ion beam analysis work at the ion beams materials laboratory was supported by a LANL new program development grant in support of its MaRIE signature facility.

This chapter, including text and data, is a reprint of the material as it appears in J. L. Barton, Y. Q.Wang, T. Dittmar, R. P. Doerner, G. R. Tynan, Deuterium retention in tungsten after heavy ion damage and hydrogen isotope exchange in pisces, Nucl. Instrum. Methods Phys. Res., Sect. B 332 (2014) 275279. The dissertation author was the primary investigator and author of this paper.

Chapter 6

Analytical diffusion model for hydrogen isotope exchange in tungsten

6.1 Introduction

Hydrogenic species retention in plasma facing materials (PFCs) is a major concern for practical operation of magnetically confined fusion reactors [34]. Tritium fuel accumulates in PFCs diffusing well beyond their implantation depth of 2–5 nm, raising both safety and tritium self-sufficiency concerns. The isotope exchange technique will be useful in prolonging the lifetime of PFCs because much of the trapped tritium fuel in PFCs can be recycled back into the plasma. By treating a PFC that has H isotopes retained within it using a plasma of another H isotope, we showed in chapters 4-5 and others have also shown [97, 50, 49] that the retained H isotopes can be exchanged out of the material, at depths that are well beyond the ion implantation depth of a few nanometers. An isotope exchange

model was proposed [98] that depended on the ion implantation energy for materials like Si, C, and other Ti composites. However, there is no predictive model for the isotope exchange rate in materials like W, where the arrival rate of the exchanging H isotope at depths beyond the ion implantation zone is due to H isotope diffusion and not energetic deposition. This chapter introduces a model for H retention depth profiles in W and attempts to model how this profile changes due to isotope exchange.

6.2 Experimental

The metal samples used in the experiments used in this chapter were 2 mm thick by 6 mm diameter hot-rolled tungsten with purity of 99.97 wt.% manufactured by PLANSEE [66]. These samples were polished mechanically to a mirror-like finish, cleaned in an acetone and ethanol ultrasonic bath, and annealed at 1200 K for one hour to remove any impurities and reduce other intrinsic defects.

A radio frequency (rf) helicon wave plasma source, characterized in [76], was used to treat the W samples with D and H plasmas. With an input power of 1.2 kW, plasma densities range from $6 - 9 \times 10^{16}$ m^{-3} , and plasma fluxes are $1.5\,(\pm.2) \times 10^{20}$ ions/m^2/s, both measured by sweeping a Langmuir probe in front of the sample. The flux was also verified by measuring the current to the sample holder. The ion energy in these experiments was 100 eV, which was estimated from subtracting the negative bias on the sample holder from the measured plasma potential. Note that since the fluxes here are considerably lower than the fluxes achieved in PISCES-A, each W sample was treated with D plasma to a fluence of 10^{24} ions/m^2. This fluence is still sufficient to saturate the W samples [38], and the total plasma exposure time was the same as in chapters 4-5. The vacuum chamber was then pumped down for 5 min, the gas inlet lines were purged with H_2 gas, and

the sample was treated with H plasma to a fluence of either 10^{22}, 5×10^{22}, 10^{23}, or 10^{24} ions/m^2, except the control sample which was not exposed to H plasma. The temperature of the samples during plasma treatment was measured using a thermocouple pressed to back of the sample, insulated from the plasma. Samples were held at a constant 370 K throughout plasma exposure.

The retained D concentration profile was subsequently measured using nuclear reaction analysis (NRA) by the D(^{3}He,p)^{4}He reaction at the Ion Beams Materials Laboratory (IBML) at Los Alamos National Laboratory (LANL). The measurement technique is described in more detail in chapter 3 and in the literature [81]. Tungsten samples were irradiated with a ^{3}He ion beam at room temperature with energies of 0.5, 0.8, 2, 2.75, 3.5, and 4.5 MeV to produce a D depth profile with a depth resolution of less than one micron up to a depth of 7.7 μm, similar to [97].

6.3 Model

We have developed a model for plasma ion implantation, diffusion, and trapping as well as for the exchange and removal of hydrogen species. Here we introduce the key elements of the model and then compare it against the experimental results.

6.3.1 Retention

H isotopes are retained in defects in the crystalline lattice as they diffuse in solution through W into the bulk region, which is defined as greater than the implantation zone of the plasma ions. The diffusion of H in *solution* has been studied extensively through modeling and experiment [18], but we want to study

how particular types of defects, such as dislocations or vacancies, accumulate an inventory of H as it diffuses through W. We will assume that these defects do not migrate so that the arrival rate of atoms to a trap site (i.e. the filling evolution of the trap site) will be related to the measured diffusion coefficient of solute H in W. Formulating the problem as the evolution of filled trap site concentrations, as opposed to the diffusion of solute atoms explicitly, allows for easy comparison to the trapped D spatial profile in NRA experiments. H atom interactions with defects will be defined by a trapping and release rate, similar to the diffusion code TMAP [96]. We take the trapping rate for each diffusing atom to the ith trap site to be given as

$$\alpha_{t,i} = \frac{D_s}{\lambda^2}\left(\frac{C^0_{t,i} - C_{t,i}}{N_{\mathrm{W}}}\right), \tag{6.1}$$

where the subscript i refers to the trapping energy of the ith type of trap as discussed below; D_s is the diffusion coefficient of atoms through solution defined by [99]; λ is the lattice parameter; $C^0_{t,i}$ is the total concentration of traps of type i, which we will assume to be uniformly distributed in the material without space or time dependence; $C_{t,i}$ is the concentration of filled traps of type i and does depend on space and time; and N_{W} is the atomic density of W. The choice of the value of D_s, the Frauenfelder coefficient, is worthy of mention because we seek to decouple the effects of trapping from solute diffusion. Frauenfelder's measurement of D_s at temperatures greater than 1000 K is assumed to have little trapping effects. In our work here, we extrapolated this value of D_s to lower temperatures to reflect only the solute diffusion and treat trapping separately. The coefficient of (6.1) defines the lattice jump rate of H in W, and this is multiplied by the probability of finding an empty trap of type i. This probability is not constant because $C_{t,i}$ increases until it equals $C^0_{t,i}$, at which point the trapping rate is reduced to zero.

The release rate of the ith trap site is taken as

$$\alpha_{r,i} = \nu_{\mathrm{D}} e^{-E_{t,i}/T}, \tag{6.2}$$

where ν_{D} is the maximum frequency of oscillations in one dimension due to thermal vibrations (Debye frequency) of the trapped atom, $E_{t,i}$ is the energy the trapped atom has to gain to escape the trap site, and T is the temperature of W in energy units. These rate coefficients (6.1) and (6.2) can be used to model one atom in each trap. However, density functional theory (DFT) models have shown [35, 36, 37] that trapping defects in W can trap more than one H atom. For instance, it has been modeled that a monovacancy defect in W can accumulate up to 10 H atoms [35]. This work also shows that as the defect accumulates more atoms, the energy $E_{t,i}$ that the trapped atom must gain to escape the trap decreases (i.e. a single H atom in a monovacancy must gain more energy to escape than an H atom with nine other H atoms in that vacancy). We handle these various trapping energies by treating them as distinct and separate trapping types. Thus a vacancy with no H atoms is treated as a separate trap from a vacancy with 1 trapped H atom, which is separate from a vacancy with 2 trapped H atoms and so on. The trapping energy must then be a function of the number of trapped atoms and will be estimated from the DFT models. In this way, we can include the fact that defects in W can hold more than one H atom. By treating each trapping energy as a separate trapping site, we can use the trapping and release rates to model one atom in each trap site.

Since H isotopes must first diffuse through solution to reach a trap site, we treat the concentration of each partially filled trap site as a diffusive process,

$$\frac{\partial C_{t,i}}{\partial t} = D_s \frac{\partial^2 C_{t,i}}{\partial x^2} - \frac{\partial C_s^{\mathrm{local}}}{\partial t}, \tag{6.3}$$

where the use of D_s in this equation is motivated by the fact that the evolution of the filled trap site concentrations, $C_{t,i}$, depends on the arrival rate of solute atoms and C_s^{local} is the local concentration of this H isotope in solution. Eq. (6.3) defines the time evolution of the concentration of a partially filled trap of type i in terms of a one dimensional diffusion process, combined with a volumetric loss rate due to the escape of trapped atoms which enter into solution. The sum of all the solutions of (6.3) over all of the i trap types will then give the total retention profile that can be compared to NRA data. We can determine C_s^{local} by comparing the rates of trapping and release to the rate of diffusion through solution over a relevant length scale. Fig. 6.1 shows the estimated values for trapping, release, and diffusion of H in W samples for a relevant range of sample temperatures. We see that the diffusion rate (over a length scale of 10 μm) is much less than the release rate (with a trapping energy of 1 eV, similar to a vacancy trap [35]) and the trapping rate over all temperature ranges for fusion related plasma-material experiments. As the concentration of filled traps increases toward saturation (i.e. ${}^{C_{t,i}}/_{C_{t,i}^0} \rightarrow 1$), the trapping rate decreases, approaching the diffusion rate. However, the release rate is constant with constant material temperature, making the trapping rate's approach to saturation slow as the release rate becomes much greater than the trapping rate. Motivated by these estimated rates, we can assume that the trapping and release rates are always much greater than the diffusion rate throughout the simulation. As a result, a local equilibrium condition exists between the concentration of trapped atoms and the local concentration of atoms in solution, and this is given as

$$\alpha_{t,i} C_s^{\text{local}} = \alpha_{r,i} C_{t,i}. \tag{6.4}$$

Solving this equation for C_s^{local} with the definitions (6.1) and (6.2) and using it in Eq. (6.3), we can then find the rate at which the concentration of atoms in trap

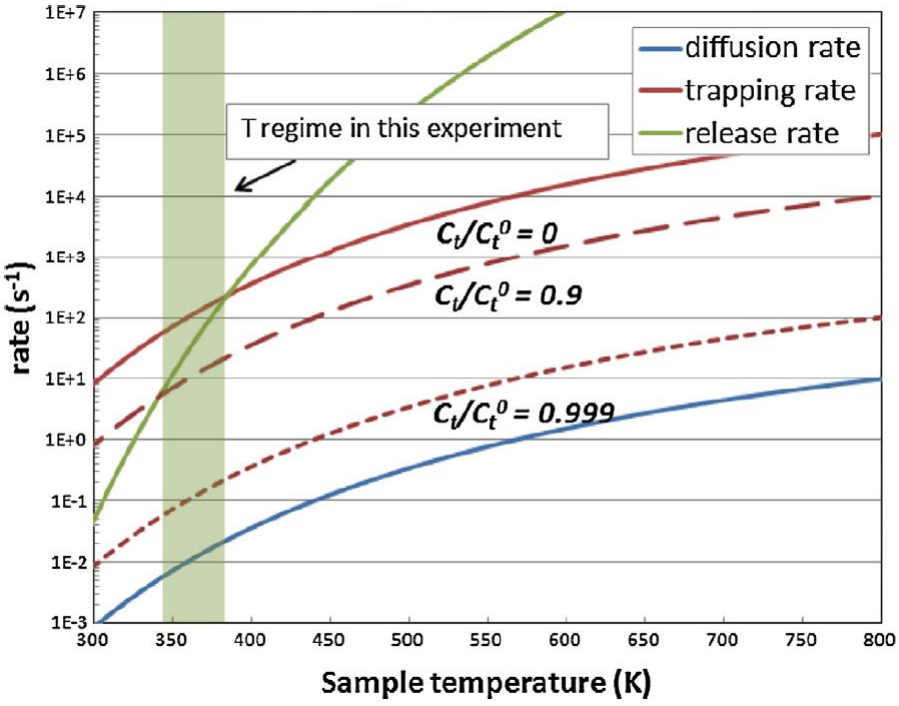

Figure 6.1: Diffusion rate much lower than trapping and release rates for all relevant experimental temperatures.

type i fills throughout the material.

Solutions for each trap type i of Eq. (6.3) require initial and boundary conditions. Initially the concentration of trapped D (or H) is assumed to be zero throughout the domain, i.e. we assume initially that $C_{t,i} = 0$ for all i and all position x. The boundary conditions are then

$$C_{t,i}\left(x = 0, t > 0\right) = C_{t,i}^{0}, \tag{6.5}$$

$$C_{t,i}\left(x \to \infty, t > 0\right) = 0. \tag{6.6}$$

Condition (6.5) states that, on the surface, trap type i becomes completely saturated, which is reasonable given the high fluxes in most plasma experiments. For convenience, we will assume that the NRA measurement is taken instantaneously after the plasma is turned off (i.e. the trapped concentrations are frozen in at the

end of the experiment) so that the transport of atoms after plasma exposure are not calculated. H isotopes can diffuse to the surface and desorb after plasma treatment, but we are taking this effect to be small. Frauenfelder's diffusion coefficient [99] at our experimental temperatures estimates that the deepest penetration of hydrogen isotopes through solution is 90 μm, and our sample thickness is 2 mm. So it is reasonable to have boundary condition (6.6) such that no traps are filled for very large depths. By writing the initial and boundary conditions in this way, we can combine the space and time variables into one variable, and hence solve an ordinary differential equation, using the Boltzmann transformation

$$y = \frac{x}{2\sqrt{Dt}}, \tag{6.7}$$

where $D = {}^{D_s}/\left(1+\frac{\alpha_{r,i}\lambda^2 N_W}{D_s C^0_{t,i}}\right)$ is the effective diffusion coefficient. This effective diffusion coefficient reflects the decoupling of solute diffusion from the effects of trapping. Eq. (6.3) can now be solved using a simple numerical method because of the non-linearity caused by the non-constant value of the trapping rate. Fig. 6.2 shows the numerical solution for one trap type after exposure to D plasma (blue curve) for $t = 5000$ s. For small values of $C_{t,i}$, to first order, the trapping rate is constant. In that case, the solutions of (6.3) are complementary error functions.

To model our NRA data, we include three trap types with a total of 21 trapping energies. According to Liu's DFT work [35], a monovacancy within a grain (or bulk vacancy) needs to be modeled with 10 trapping energies because up to 10 atoms can occupy this defect. Dislocation defects can hold up to 6 atoms and therefore have 6 trapping energies, according to a model proposed by Xiao [36]. Finally, Zhou [37] proposes 5 types of grain boundary (GB) vacancies that can hold only 1 atom each but have different trapping energies based on the lattice configuration. We will take the trapping energies from these published

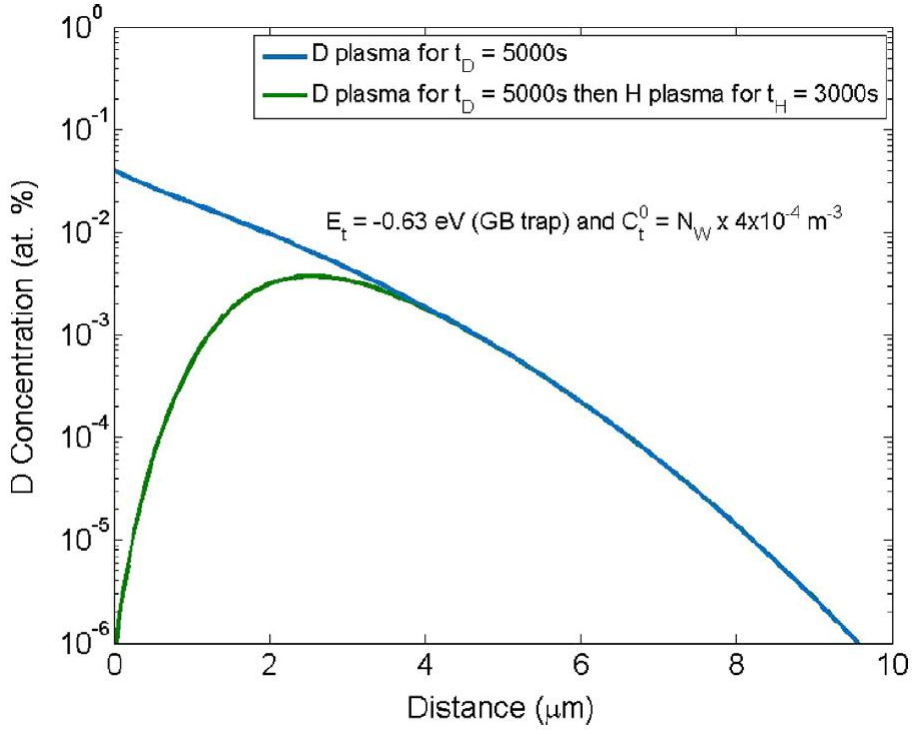

Figure 6.2: The solution for one trapping type before (blue curve) and after (green curve) isotope exchange.

DFT models and treat them as fixed parameters in our model. Because all of the trapping energies are defined, the release rate is therefore completely constrained. We then define the distribution of these 3 defect types $\left(C_{t,i}^0\right)$ as fitting parameters for the retention data. We chose uniform distributions of 0.04, 1.3×10^{-3}, and 5×10^{-4} at.% for GB, dislocation, and bulk vacancy traps, respectively, which qualitatively represent the occurrence of these defects. We chose GB defects to be the most prominent inherent defect in our polycrystalline W material, then chose dislocations as the next largest defect due to the findings in another retention model [100], and inherent bulk vacancies were chosen as the least prominent defect. All parameters (trap concentrations and energies) are now fixed when used to calculate the isotope exchange rate.

6.3.2 Isotope exchange modeling

An isotope exchange model was proposed by Doyle [98] in which the ion implantation energy of H isotopes into Si, C, and other Ti composites was the key variable that governed the trapping physics. Since experiments with W have shown that isotope exchange happens at micrometers into the bulk, which is much greater than plasma ion implantation depth of a few nanometers [97, 50, 49], this model needs to be modified for the case in which the diffusion of an atom resulting from ion implantation is included. Doyle's model assumes that each isotope has an equal probability of being trapped, and whichever atom is not trapped then disappears from the material. The loss rate of D being exchanged by H, $\frac{\partial C_{t,i}^{\mathrm{D}}}{\partial t}$, is proportional to the probability of H taking the D filled trap multiplied by the rate of H arrival at an ith trap that is filled with a D atom. Therefore, we have

$$\frac{\partial C_{t,i}^{\mathrm{D}}}{\partial t} = -\frac{1}{2}\frac{C_{t,i}^{\mathrm{D}}}{C_{t,i}^{0}}\frac{\partial C_{s}^{\mathrm{H,local}}}{\partial t}, \tag{6.8}$$

where the D and H superscripts indicate either trapped concentrations of D or H, respectively. The one half in (6.8) is the probability that H will exchange with D, since our model states that only one atom can occupy each trap site and has two competing atoms. The second ratio is the fraction of traps of type i that are filled by D. The local equilibrium condition (6.4) relies on the fact that atoms are trapped and released orders magnitude faster than they can diffuse through solution. This is true for both isotopes, and thus the equilibrium holds for both H and D. During the isotope exchange phase, we only consider the diffusion of the exchanging isotope (H). We do not consider the diffusion of D atoms during the H plasma treatment, but we do consider trapped D atoms to be in equilibrium with solution as before. Eq. (6.4) still applies to D atoms that have not been exchanged,

but if an H atom has diffused to that trap site, an H atom has a 50% chance of occupying trap instead. We could alternatively model how D atoms diffuse and are re-trapped during isotope exchange by solving the reaction–diffusion equations for both species simultaneously. However, this first simple model attempts to extract some of the basic physics of isotope exchange. Due to the flood of H atoms occupying solution during the exchange phase, we assume that D atoms are not trapped again after exchanging and instead escape from the sample. Eq. (6.8) can then be solved directly to find the concentration of D after isotope exchange with H

$$C_{t,i}^{\mathrm{D}} = C_{t,i}^{\mathrm{D,init}} \exp\left\{ A \left[1 - \left(1 - \frac{C_{t,i}^{\mathrm{H}}}{C_{t,i}^{0}} \right)^{-1} \right] \right\}, \tag{6.9}$$

where $C_{t,i}^{\mathrm{D,init}} = C_{t,i}\left(x, t = t_{\mathrm{D}}\right)$ is the D filled trap profile after exposure to D plasma for time t_{D}, $A = \frac{\alpha_{r,i}\lambda^2 N_{\mathrm{W}}}{2 D_s C_{t,i}^{0}}$, and $C_{t,i}^{\mathrm{H}} = C_{t,i}\left(x, t = t_{\mathrm{H}}\right)$ is the H filled trap profile after exposure to H plasma for time t_{H}. Fig. 6.2 shows $C_{t,i}^{\mathrm{D}}$ after isotope exchange (green curve) with $t_{\mathrm{D}} = 5000$ s and $t_{\mathrm{H}} = 3000$ s. To obtain the total D profile after isotope exchange, the sum of all i solutions to (6.9) represent the remaining D inventory.

6.4 Results and discussion

The observed D retention profile (Fig. 6.3) is similar to other retention experiments with this W material and plasma exposure [97]. To replicate the NRA data with the model, the solutions of Eq. (6.3) with ($t = t_{\mathrm{D}}$, the D exposure time) for each trap site energy (defined by 1 of 3 fitting parameters for each defect type, $C_{t,i}^{0}$, and literature values of $E_{t,i}$ for the ith trapping energy) were added together to obtain the total D retention profile. Comparing the individual filled trap concentration profiles, the model indicates that GB traps fill much slower than the higher energy traps in dislocation and bulk vacancies even though there is a

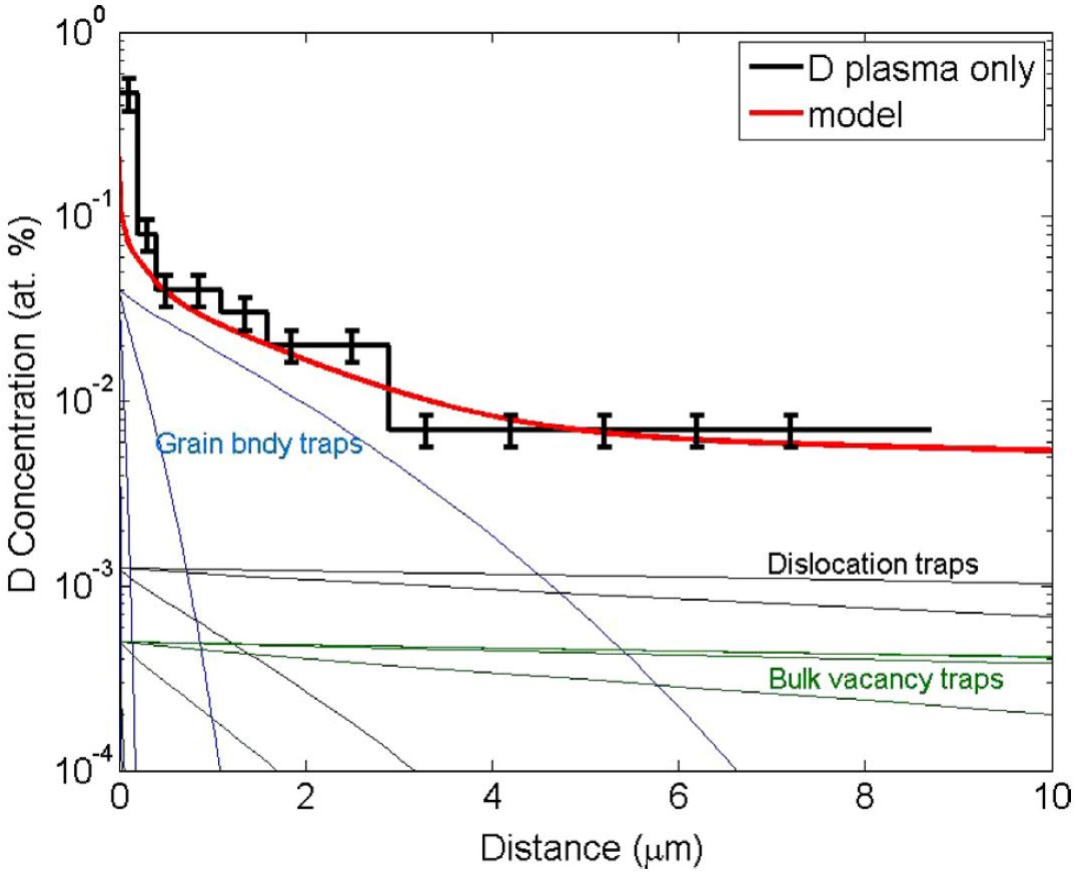

Figure 6.3: D retention NRA data in W after a D fluence of 10^{24} ions/m^2 and modeled by the sum of all of the partially filled trap concentrations for each trapping type: grain boundaries (5 types uniformly distributed 0.04 at.%), dislocations (6 types uniformly distributed 1.3×10^{-3} at.%), and bulk vacancies (10 types uniformly distributed 5×10^{-4} at.%).

higher GB trap density throughout the material. This is because the low trapping energies of the GB traps have higher release rates, so these traps take more time to fill. Higher energy traps fill throughout the material much faster because it is rarer for an atom to escape due to thermal vibrations in the lattice.

Although the distribution of trap concentrations were free parameters used for fitting, we observe in Fig. 6.3 that the model represents the D depth profile data well. If these defect concentrations could be estimated accurately or measured elsewhere, this model could provide a fully predictive model for retention. However,

exact knowledge of the material's defect history is not available at this point in time. Having fit the model to the D depth profile obtained for the D plasma exposed sample, the parameters $C_{t,i}^0$ are now fixed and can be used to model the effects of H isotope exchange.

We use Eqs. (6.3) and (6.9) to estimate the loss of D after exposure to H plasma. Fig. 6.4 shows the D depth profile after various fluences of H plasma as well as the resulting model predictions. The expected experimental result [97, 50, 49] of D inventory decreasing with increasing H fluence is again observed here. The model follows the isotope exchange data within the experimental error of the measurements with the two lowest H fluences, except for the data point closest to the surface which could be accounted for by blistering or other surface morphology effects not considered in the model. For the highest H fluences, the model predicts that H diffuses deeper in the material and thus exchanges with more trapped D than what is measured. The overestimation could be due to the assumption that an exchanged D disappears immediately from the material, where realistically it could be re-trapped before reaching the surface.

Atoms can escape more easily (i.e. exchange atoms more efficiently) from lower energy traps, and we observe this in the model. The D concentration profiles resulting from lower energy traps are reduced more rapidly during isotope exchange than the concentration profiles from higher energy traps. These rapidly exchanging D profiles produce an odd result for the total predicted D concentration profile near the surface by appearing to create oscillating features. Because each trapping site is treated separately in the model, these features arise after the resulting solutions of each trap type are added together to calculate the total concentration. Physically, these trapped concentration profiles are not independent of each other: D atoms released from a low energy trap could then be re-trapped by a higher energy trap.

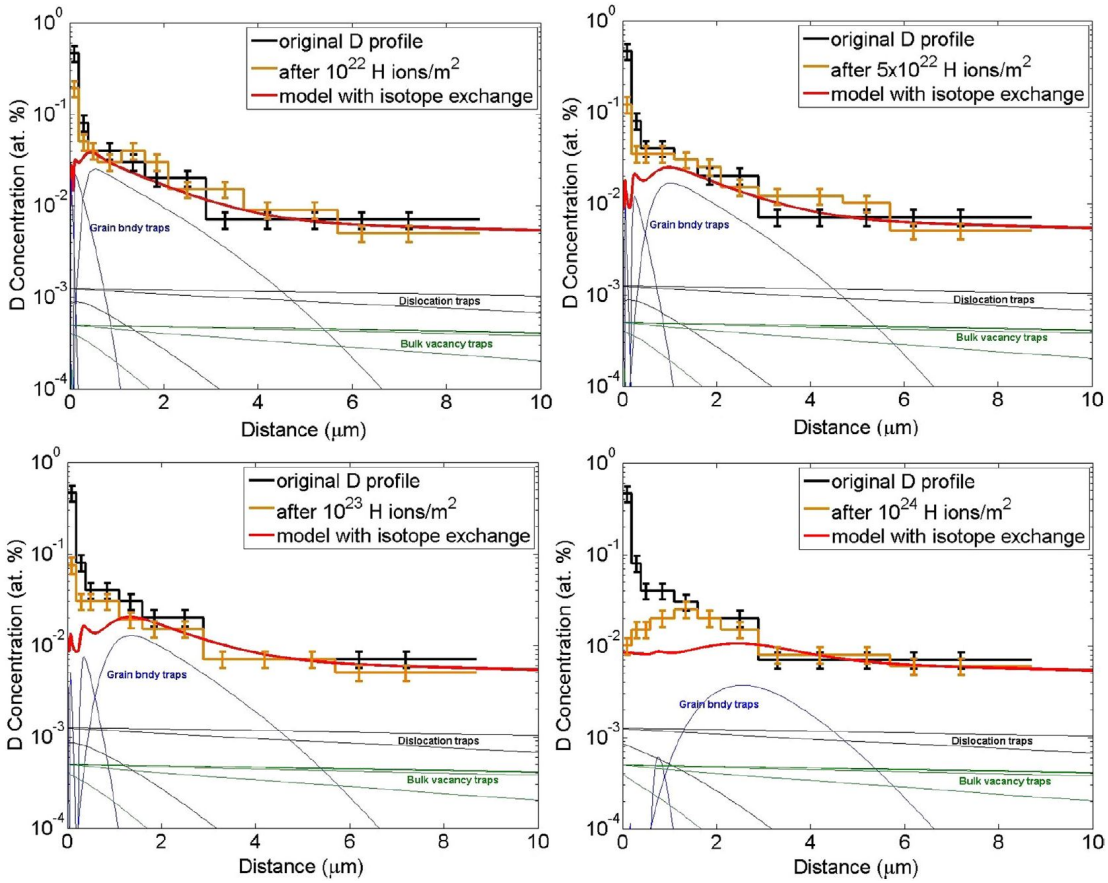

Figure 6.4: Deuterium retention profiles after isotope exchange and the corresponding isotope exchange model prediction, where t_{H} is calculated from the flux and fluence of the H plasma. The D profile for the non-isotope exchanged sample is also plotted for reference.

Re-trapping of the exchanged solute D atoms during H plasma exposure need to be included in the model in order to have better agreement with the data. Overall this model gives qualitative agreement with what is experimentally observed, namely that isotope exchange is inefficient at replacing the implanted isotopes at depths greater than 1 μm.

6.5 Summary

A retention model is proposed that models how trapping sites, defined by their trapping energy and their distribution in the material, fill up as H isotopes diffuse through solution. Three defect types are used in the development of the model: grain boundary vacancies, dislocations, and bulk vacancies. The trapping energies are defined by published DFT modeling [35, 36, 37]. We assume these 3 defect types are uniformly distributed in the material, and since exact knowledge of their distributions are not known, we consider their values as 3 free parameters. Each trapping site is treated separately allowing insight into how each site accumulates and exchanges inventory with isotopes. Another advantage of the model is that it is now feasible to include any number of trapping types, which will allow us to include defects not intrinsic in the material like ion or neutron damage induced vacancies. We reproduce the experimental D retention data well and capture the main physics of isotope exchange with the model. This recasting of the Doyle isotope exchange model [98] with a H diffusion arrival rate seems to agree well with the data at low H fluences, but seems to overestimate the isotope exchange rate at high H fluences. Future modeling work should include the possibility of D atoms being re-trapped in the material after an exchange event.

Acknowledgements

This work was supported by the U.S. Department of Energy under DE-SC0001999 and DE-FG02-07ER54912 and the University of California Office of President Research Fund under Award Number 12-LR-237801. The ion beam analysis work at IBML was supported by a LANL new program development grant in support the UCOP project.

This chapter, including text and data, is a reprint of the material as it appears in J. L. Barton, Y. Q.Wang, R. P. Doerner, G. R. Tynan, Development of an analytical diffusion model for modeling hydrogen isotope exchange, J. Nucl. Mater. 463 (2015) 1129-1133. The dissertation author was the primary investigator and author of this paper.

Chapter 7

Plasma implanted hydrogenic diffusion and trapping in ion beam damaged tungsten

7.1 Introduction

Retention of H isotopes in W and other materials is a subject of major interest due to tritium accumulation in plasma-facing components (PFCs) in magnetically confined fusion reactors [34, 85, 11, 84]. H isotopes diffuse well beyond their ion implantation depth (ranging 2-5nm for 100 eV ions), which raise tritium safety and self-sufficiency concerns. Experiments have shown [100, 88, 58, 57, 86, 87] that displacement damage from neutrons in PFCs enhance H retention and can have a significant impact on the long term operation of a reactor. Displacement damage experiments using energetic (∼1-10 MeV) heavy ions as surrogates for fusion neutrons have been used to study these long term material and retention effects in short time frames [101, 97, 95, 59, 93, 60, 61, 89, 62, 90]; however unlike neutrons,

ion irradiation can only damage the near surface due to the short mean-free path of the heavy ions in the lattice. The experiments in this chapter will examine D retention in W with the effects of an ion-beam induced peaked damage profile and a uniform damage profile, created with multiple ion energies, up to 0.8 μm in depth.

Most plasma-material studies lack a unified theoretical model on which to make predictions other than from empirical studies alone. This difficulty in creating theoretical models occurs in part due to the multi-scale nature of the problem. There are not only the quantum effects of atomic trapping within vacancies [36, 37, 35] but also morphology effects on the material surface like D-filled blisters [95, 26] or changes to bulk material properties like thermal conductivity [15] that occur over macroscopic scales. In this chapter, we address this problem, focusing our attention on the D retention profile at depths greater than the ion implantation zone and consider surface effects separately. We endeavor to create a simplified model that strips away many of the complicated interrelated morphological effects, like blistering or sputtering, from the problem with the idea to add them back in later. Motivated by these considerations, the plasma treatments in this work were conducted at low temperature (380 K), to ensure that D filled blister growth and W defect migrations would be avoided. This simplified model of retention allows the identification of the dominant physics of trapping and diffusion so that empirical data can be extrapolated to make predictions in more extreme environments not available with current experimental facilities.

This chapter will discuss D retention experiments in W samples with controlled levels of displacement damage. A Cu ion beam is used to induce damage at room temperature, thus avoiding the migration of monovacancies to form larger vacancies at temperatures larger than 570K [102]. The samples are then exposed

to a D plasma with a sample temperature of 380 K in which D retention is known to be significant [38]. Overall, the retention increases with increasing dpa, and the shape of the damage profile does not seem to significantly affect the shape of the retention profiles or total retention, even though the uniformly damaged samples have slightly more total displacements than the peaked damage profile. We develop a continuum model for trapping and diffusion, which will culminate with the calculation of a diffusion coefficient for hydrogenic atoms in solution with W that is dependent on the concentration of trapped atoms. Our simplified model captures most of the measured D retention profile for all damage levels. From this we can extract a diffusion coefficient that successfully captures the results found in previous measurements of H diffusion in W.

7.2 Experimental

The metal samples used in these measurements were 2 mm thick by 6 mm diameter hot-rolled W with purity 99.95 wt.% manufactured by Midwest Tungsten Services, Inc. These samples were polished mechanically to a mirror-like finish, cleaned with acetone and ethanol ultrasonic baths, and annealed at 1200 K for one hour to remove any impurities and reduce other intrinsic defects.

Samples were then irradiated with Cu ions at the Ion Beams Materials Laboratory (IBML) at Los Alamos National Laboratory (LANL). The SRIM-2012 [70] code was used to simulate the number of W lattice atom displacements per Cu ion and the stopping range of the Cu ions for ion energies of 0.5, 2, and 5 MeV (fig 7.1). We used 5000 simulation ions with the "detailed calculation with full damage cascades" option turned on with a displacement damage threshold of 90 eV for W [71]. The displacements per atom (dpa) are calculated from the fluence

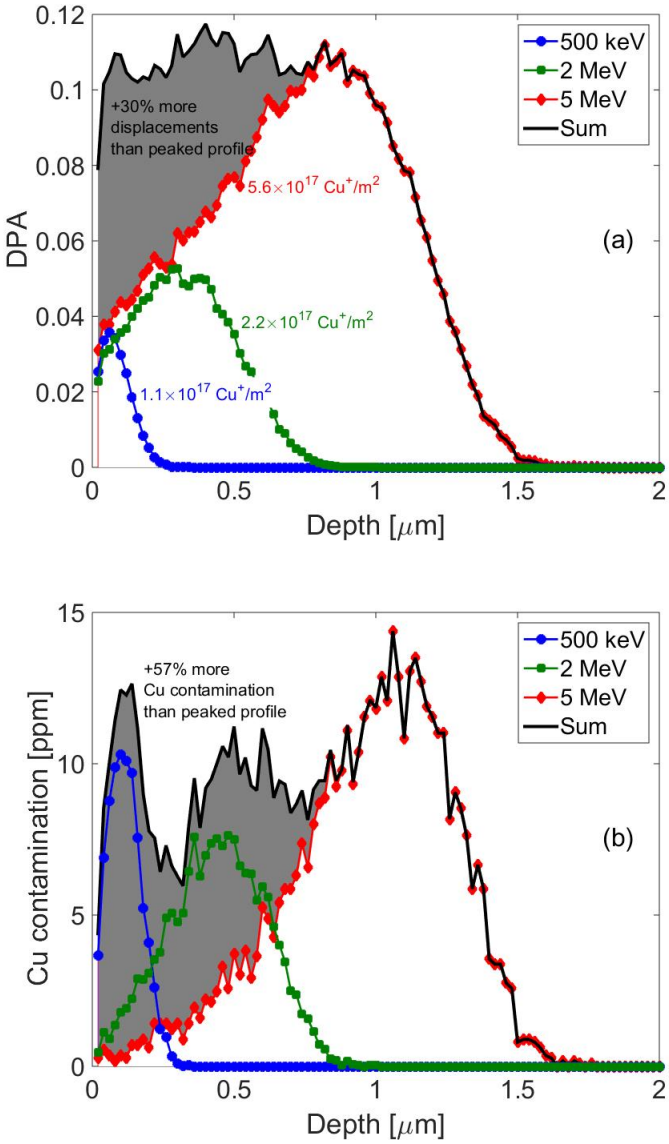

Figure 7.1: SRIM predictions (a) of dpa for Cu ion beams with energies of 0.5, 2 and 5 MeV as well as the sum of these effects on a W target, and (b) the resulting Cu concentration profile added by Cu ion beams with energies of 0.5, 2 and 5 MeV as well as the sum of these effects on a W target.

at a given energy as

$$\text{dpa} = \frac{N_{\text{displacements}}\phi}{N_{\text{W}}},$$

where $N_{\text{displacements}}\,(\text{ions}\cdot\text{m})^{-1}$ is the number of displacements after ion beam exposure and damage cascade relaxation given by the SRIM simulation, $\phi\,(\text{ions}\cdot\text{m}^{-2})$ is the ion beam fluence, and $N_{\text{W}}\,(\text{m}^{-3})$ is the atomic density of W. Two irradiation methods at room temperature were used. One produced samples with a damage profile peaked at 0.8 μm and the other a uniform damage profile up to 0.8 μm depth. We irradiated at room temperature to reduce the amount of defect migrations to grain boundaries, so that the vacancy defect densities and distributions would not change before plasma exposure. Figure 7.1 illustrates the fluences needed to produce a 10^{-1} dpa profile and the resulting Cu contamination profile. The peaked damage profile for 10^{-1} dpa was obtained with a single Cu ion fluence of 5.6×10^{17} ions/m^2 at 5 MeV, and the 10^{-1} dpa uniform damage profile was obtained with the sequential ion fluences of 5.6×10^{17} ions/m^2 at 5 MeV, 2.2×10^{17} ions/m^2 at 2 MeV, and 1.1×10^{17} ions/m^2 at 0.5 MeV. The SRIM calculation shows (fig 7.1) that the uniform damage profile displaces a total of 30% more W atoms than the peaked profile, integrated over the damage profile. The total Cu contamination in the uniform damage profile is increased by 57% compared to peaked profile; however, the maximum contamination in both peaked or uniform damage profiles is never significantly greater than the intrinsic ~10 ppm Cu from the manufacturer [103]. The added Cu contamination at this fluence is not thought to affect retention, since [97] showed no difference in retention from self-damaging for 10^{-1} dpa and below. Using these methods we produced peaked and uniform damage profiles at 10^{-1} dpa, and by reducing the Cu ion fluences by 10 or 100, we also produced samples with 10^{-2} and 10^{-3} dpa, respectively. SRIM calculates the vacancy profile after damage cascade relaxation per unit Cu ion fluence, which we will use

as inputs to our retention model to calculate retention after ion damage.

These ion-beam damaged samples, as well as a control sample with no damage, were then exposed to D plasma. A radio frequency (rf) helicon wave plasma source, characterized in [76], was used for plasma exposure. With an input power of 1.2 kW, plasma densities range from $6-9\times10^{16}$ m^{-3}, and constant plasma fluxes are $4(\pm.2)\times10^{20}$ ions/m^2/s, both measured by sweeping a Langmuir probe in front of the sample. The flux was also continuously monitored by measuring the current to the sample holder. The ion energy in these experiments was 100 eV, which was estimated by subtracting the negative bias on the sample holder from the measured plasma potential. Each W sample was treated with D plasma to a fluence of 10^{24} ions/m^2. The temperature of the samples during plasma treatment was measured using a thermocouple pressed to the back of the sample, insulated from the plasma. Samples were held at a constant 380 K throughout the plasma exposure, heated by the plasma and cooled by pressurized air inside the sample holder. This temperature is high enough so that solute D atoms can still diffuse but low enough to avoid D filled blister growth on the surface [26] as well as avoid the migration of vacancy defects [102].

The retained D concentration profile was measured using nuclear reaction analysis (NRA) by the D(^{3}He,p)^{4}He reaction at IBML about a week after plasma exposure at UC San Diego. The measurement technique is similar to [81], where multiple ^{3}He ion beam energies are used on each sample to produce several proton spectra to increase resolution at greater depths. The proton spectra were simulated with SIMNRA [82], where the free parameters are W layer thicknesses of uniform concentration and the fraction of D in those layers. All of the proton spectra need to be fit simultaneously in order to deconvolve the total D depth profile. A code applying Bayesian statistics [104] was used to find the most probable layer

thicknesses, given the ion beam data. Ion energies of 0.6, 0.8, 1.2, 1.6, 2, 2.5, and 3.5 MeV were used for a depth resolution of less than 1 μm up to a depth of 5.7 μm.

Total D retention in W was subsequently measured with thermal desorption spectroscopy (TDS). Each sample was heated from room temperature to 1273 K in vacuum with a background pressure of 4×10^{-5} Pa at 0.5 K/s with infrared heating lamps. A quadrupole mass spectrometer (QMS) tracked the signals of D_2 and HD molecules as the sample was heated. The QMS was calibrated by a standard D_2 leak after the analysis.

7.3 Retention model

Hydrogen isotopes diffusing in solution with W beyond the implantation zone [92] can be trapped in lattice defects. We want to study how in-grain mono-vacancy, dislocation, and grain boundary (GB) vacancy defects accumulate H isotopes. In this section we will briefly analyze a retention model that has been used to model D retention in W and find that we can propose a more simplified retention model by examining the rate limiting processes. This simplified model can replicate D retention after displacement damage and quantify the reduction of hydrogenic diffusion due to trapping effects.

A 1-D continuum model for diffusion with a sink term due to trapping effects [96] has been used to calculate the concentration of solute D atoms, $C_s(x,t)$, in W by modeling the migration of D atoms during plasma exposure and TDS analysis. The trapping effects are described by the rate of change of the trapped concentration

$$\frac{\partial C_{t,i}}{\partial t} = \alpha_{t,i} C_s - \alpha_{r,i} C_{t,i}, \tag{7.1}$$

where $C_{t,i}$ (m^{-3}) is the concentration of filled traps of the ith trap type, $\alpha_{t,i}$ (s^{-1}) is the trapping rate of the ith trap type, and $\alpha_{r,i}$ (s^{-1}) is the release rate of the ith trap type. In this published model [96], a "trap type" is defined by the density of this trap in the material, where it is assumed that each trap has a one D atom capacity, and its trapping energy. $\alpha_{t,i}$ is related to the trap density, and $\alpha_{r,i}$ is related to the trapping energy. The rate of change of the trapped concentration in the ith trap type given by (7.1) is defined by difference between the rate of solute atoms falling into traps and the rate at which trapped atoms escape back into solution.

The simulation code [96] allows for the definition of three trap types. This simulation is fit to TDS data by defining the trapping energies and densities of trapping sites in the material. Trapping energies are thought to scale with the temperature at which the peaks of the thermal desorption flux occur in the TDS data. This is because the release rate increases as the temperature increases. Thus the probabilities of atoms escaping from high energy traps increases at higher temperatures. The trap densities are thought to correlate to the amplitude of these peaks. However, there are limitations to this type of analysis. First, the solution is not unique. For instance, say the measurement of the thermal desorption flux versus temperature has one peak. This data could be fit by one trapping energy and trap density or could equivalently be fit using three trapping energies with lower trap densities. Secondly, we cannot discern whether each trap type is a vacancy, dislocation, or otherwise because the trapping energies are free parameters. Thirdly, we know from DFT models [36, 35] that defects like vacancies and dislocations can trap more than one atom, and the depth of the potential well of the trap decreases as additional atoms fall into the trap. The trap is then filled when the potential well depth decreases until it is comparable to the activation

energy of an atom diffusing in a perfect lattice. This means that allowing only three trap types are not suffcient to capture the underlying physics of retention. Finally, the temperature of the W sample during TDS analysis increases beyond 570 K at which vacancy defects are mobile [102]. Mobile vacancies can merge with other vacancies to create defects with larger potential wells, meaning that traps need to be defined dynamically if the temperature of the sample is not constant and is greater than 570 K.

The model developed here still incorporates equation (7.1), but we seek to remove these other limitations. In order to do this, we first treat the trapping energies as fixed parameters given by the DFT literature, which reduces the number of free parameters and allows us to associate trapping energies with a certain defect. Second, we treat each trap type as a single occupancy trap, but we account for defects that have multiple atom capacities by treating each trapping energy given from DFT as a unique, single occupancy trap. Adding or removing an atom from the trap then changes the trap well depth and in turn changes the trap index i. Third, our measured NRA D concentration profile provides the total trapped concentration profile, $C^{\text{tot}} = \sum_i C_{t,i}$, that will be the benchmark for our simulation. This data is acquired without having to raise the sample temperature so that we do not have to simulate the effects of mobile vacancies merging to form new multi-vacancy defects. Comparing our computed profile to NRA data then provides a test of the ability of the model to capture the trapping physics. The simplified set of equations to calculate $C_{t,i}$ are justified by first considering the relative timescales for trapping, release, and diffusion for typical experimental conditions.

There are three relevant time scales in this model defined by the trapping rate, release rate, and diffusion rate. The trapping rate due to trap type i in W is

taken to be given as

$$\alpha_{t,i} = \frac{D}{\lambda^2}\left(\frac{C^0_{t,i} - C_{t,i}}{N_{\mathrm{W}}}\right), \tag{7.2}$$

where D (m^2/s) is the measured Frauenfelder diffusion coefficient of solute atoms [99] and is a function of temperature, λ (3.16×10^{-10} m) is the W lattice spacing parameter, $C^0_{t,i}$ (m^{-3}) is the density of trap type i in W, and N_{W} (m^{-3}) is the atomic density of W. The fraction $\frac{D}{\lambda^2}$ describes the jump rate of H isotopes within the W lattice and is multiplied by the probability of finding an empty trap, given by the term in parentheses. This probability decreases the value of $\alpha_{t,i}$ as the trapped concentration, $C_{t,i}$, approaches the total density of this trap type in the material, $C^0_{t,i}$, until it is saturated ($C_{t,i} = C^0_{t,i}$). The release rate from a trap is defined as

$$\alpha_{r,i} = \nu \exp\left(-E_{t,i}/T\right), \tag{7.3}$$

where ν is the maximum frequency of oscillations of an impurity in the W lattice estimated in a similar way as in [105], $E_{t,i}$ (eV) is the energy a trapped atom must gain to escape the ith trap type, and T (eV) is the material temperature in energy units. The defect densities, $C^0_{t,i}$, and trapping energies, $E_{t,i}$, define each trap type. The diffusion rate between traps is estimated from the mean free path between traps, $l_{\mathrm{mfp}} = \left(C^0_{t,i}\sigma\right)^{-1}$. We take the defect cross-section, σ, to be a circle with a radius the size of the lattice parameter, which is a conservative estimate for defects smaller than vacancy clusters. The diffusion rate is $D/l^2_{\mathrm{mfp}} = D\left(C^0_{t,i}\pi\lambda^2\right)^2$. After defining the values of $E_{t,i}$ and $C^0_{t,i}$, we can reveal the rate limiting process.

DFT models have shown that dislocations and vacancies in W can trap more than one D atom [36, 35], with the trapping energy of the defect decreasing with each additional atom occupying the trap. In other words, the trapping energy of a defect is a function of the number of D atoms occupying it. Grain

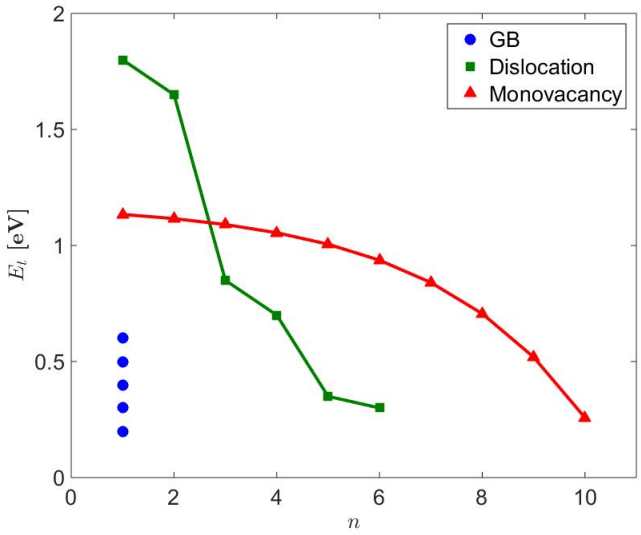

Figure 7.2: DFT calculated trapping energies from the literature. Dislocations [36] and vacancies [35] are a function of n, the number of atoms occupying the defect. GB defects have single occupancy [37], but have different energies depending on geometery of the defect and are included in this figure for comparison. These energies are fixed parameters in our model.

boundary (GB) defects are thought to have the capacity to trap only one D atom. However, depending on the lattice structure around the GB defect, published work [37] suggests five different trapping energies exist for single occupancy GB traps. Figure 7.2 shows the trapping energy versus n, the number of atoms occupying a dislocation or monovacancy defect. The GB trapping energies were included in figure 7.2 for comparison. We will therefore use the index i in our model to uniquely index each trapping energy of the five GB trapping energies ($1 \leq i \leq 5$), the six dislocation trapping energies ($6 \leq i \leq 11$), and the ten monovacancy trapping energies($12 \leq i \leq 21$). Since the multiple occupancy defects change their trapping energy when another D atom is added to or escapes from the defect, each i trap type is treated as a unique, single occupancy trap. Thus, $C_{t,i}$ describes the trapped concentration in a trap with a known energy $E_{t,i}$ and an unknown total trap density of $C_{t,i}^0$. Having 21 trap types is how we capture the effect that some

defects can be occupied by multiple atoms.

It is of course completely impractical to consider a model with such a large number of unknowns, but fortunately the model can be simplified drastically by noting that we do not need to define 21 independent trap densities, $C_{t,i}^0$. First, we note that DFT calculations indicate that ten D atoms can be trapped in a monovacancy [35]. Therefore, the in-grain monovacancy defect density will be the same for all ten trapping energies, and thus for this defect all $C_{t,i}^0$ have the same value $C_{t,i}^0 = C_{\text{vac}}$ for $i = 12$ to 21, where C_{vac} denotes the monovacancy density. In the same way, the dislocation density, $C_{t,i}^0 = C_{\text{dis}}$, has one value for all dislocation trap energies ($6 \leq i \leq 11$). The GB vacancy densities can in principle have 5 different values, since the trapping energies are related to the W atom configuration around the defect. Here, the simplest GB vacancy density model is used by assuming equal GB vacancy densities, i.e. we take $C_{t,i}^0 = C_{\text{gb}}$ for $i = 1$ to 5. All defect densities in our pristine W samples are assumed to be uniformly distributed in the material as well as immobile, which essentially means that annealing effects are negligible. Note that we have 21 trap types in all, but they are defined by one of three defect densities and literature values for the trapping energies. Because the trapping energies are completely defined by independent DFT reports, we only have three free parameters given by three defect densities C_{gb}, C_{dis}, and C_{vac} to fit to the NRA retention data. This is contrasted with the model proposed by [96], which has six free parameters: three trapping energies and three defect densities. Furthermore, we cannot justify changing C_{gb} and C_{dis} after radiation damage at room temperature, so they remain the same value determined from experiments in undamaged samples.

Now we can examine the significant rate limiting processes of trapping, releasing (de-trapping), and diffusion. The release rate, $\alpha_{r,i}$, is completly defined

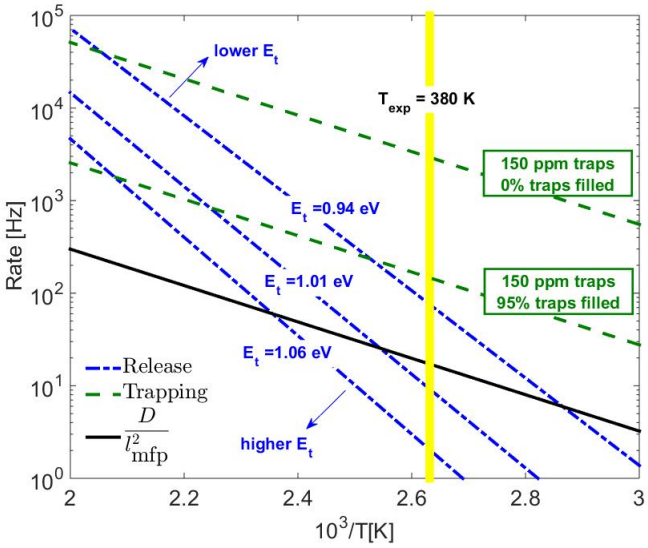

Figure 7.3: Estimate of trapping ($\alpha_{t,i}$) and diffusion (D/l^2_{mfp}) rates if each trap density, $C^0_{t,i}$, is 150 ppm and a sample of the release rates ($\alpha_{r,i}$) resulting from 21 trapping energies. Trapping rates are shown with either 0 percent or 95 percent of traps filled, and the yellow band indicates the temperature during plasma exposure for these experiments.

by the DFT energies above. However, at this point we must estimate $\alpha_{t,i}$ and the diffusion rate with defect densities used in a previous study. The sum of the defect densities in [100] (using the simulation code [96]) was determined to be 3200 ppm for two trap types, after fitting to TDS data. As an a priori estimate, we will use the same total defect density because we are using the same type of material in our work. Thus, we take each of the 21 trap types to have the same density of 150 ppm. For such a case seen in figure 7.3, when $C_{t,i} = 0$ (i.e. 0 percent of the traps are filled), the trapping rate $\alpha_{t,i}$ is more than 2 orders of magnitude greater than its diffusion rate D/l^2_{mfp} and would remain an order of magnitude greater than D/l^2_{mfp} even after 95 percent of this trap is filled. With the exception of the 1.01 eV trap, the release rates $\alpha_{r,i}$ are either significatly slower or faster than D/l^2_{mfp} at our experimental temperature, shown by the yellow band in the figure. In other words, figure 7.3 shows that in the time it takes for a solute atom to diffuse between traps,

either A) a trap is likely to never release an atom, $\alpha_{t,i} \gg {}^{D}/_{l_{\text{mfp}}^2} \gg \alpha_{r,i}$; B) a released atom is likely to be re-trapped before diffusing to the next trap, $\alpha_{t,i} \geq \alpha_{r,i} \gg {}^{D}/_{l_{\text{mfp}}^2}$; or C) a trap releases atoms faster than they can be re-trapped, $\alpha_{r,i} \geq \alpha_{t,i} \gg {}^{D}/_{l_{\text{mfp}}^2}$. In case A) the trapped concentration, $C_{t,i}$, is not likely to lose atoms to solution. Cases B) and C) imply that changes to $C_{t,i}$ by releasing to solution and re-trapping happen at much faster rates than the changes to $C_{t,i}$ due to the solute diffusion between traps. All three cases imply that in the time it takes for atoms to diffuse between traps, each $C_{t,i}$ is essentially constant, and thus $\sum_{i=1}^{21} \frac{\partial C_{t,i}}{\partial t} = 0$. In other words, we have established an equilibrium relationship between $C_{t,i}$ and C_s after each diffusion time step with

$$\sum_{i=1}^{21} (\alpha_{t,i} C_s - \alpha_{r,i} C_{t,i}) = 0. \tag{7.4}$$

In this first order evaluation of the model, we will calculate each $C_{t,i}$ separately as if it were the only trap type in the material, which assumes that each trapped concentration does not affect the others. By doing this, we calculate the concentration of only one trap type in the material where now $\frac{\partial C_{t,i}}{\partial t} = 0$. Then we have a direct relationship between the total solute concentration and trap type i

$$\alpha_{t,i} C_s = \alpha_{r,i} C_{t,i}. \tag{7.5}$$

Equation (7.5) is the local equilibrium condition between the solute and trapped concentrations in the ith trap type. When this approximation is valid, the ith trapped concentration is a function of the solute concentration and decouples trapping effects from diffusion. Having $C_{t,i}$ defined for every diffusion time step is equivalently defining $C_{t,i}$ as a species that diffuses through the material.

Since the trapping rate, $\alpha_{t,i}$, decreases as $C_{t,i}$ increases, the condition $\alpha_{t,i} \gg$

D/l^2_{mfp} will eventually be violated, since the trapping rate will approach zero for trap types that are 100 percent occupied. Our rate estimates indicate that the inequality holds until more than 95 percent of trap type i is filled (i.e. $C_{t,i}/C^0_{t,i} < 0.95$). This then puts an upper limit constraint on the maximum defect density that can be modeled using this approximation. We estimate that the defect density for a single trap type, $C^0_{t,i}$, has to be much less than 1300 ppm. If this condition on the defect density is met, then the trapping rates for each of the 21 traps are large compared to the diffusion rate for the whole simulation, and the local equilibrium condition given by equation (7.5) should hold.

Unlike the trapping rate, the release rate and the diffusion rate are constant with constant temperature. The estimate in figure 7.3 suggests that all but one release rate satisfies the conditions A), B), or C) for the whole simulation. Therefore we will ignore, for now, the one release rate in our a priori estimate that does not satisfy one of the inequalities above, since the defect densities for all trap types are not yet defined. Then we assume that the release rates are either small enough to release a negligible amount of concentration back into solution, case A), or much larger than the diffusion rate, cases B) or C).

Equation (7.5) means that the solute concentration, C_s, is a function of $C_{t,i}$ because of the local equilibrium condition. The physical picture, after examining the rate limiting processes, is of a slowly diffusing concentration of solute atoms that achieve an equilibrium value with the trapped concentrations, $C_{t,i}$, at each position in the 1-D problem. In other words, the ith trapped concentration, $C_{t,i}$, can be equivalently described as a diffusing species through the material because equilibrium with C_s is achieved before C_s diffuses further. Motivated by this physical picture, we propose a diffusion equation for the $C_{t,i}$ species. Since we are calculating the $C_{t,i}$ concentrations separately, the diffusion of the trapped

concentration of the ith trap type is defined as

$$\frac{\partial C_{t,i}}{\partial t} = D\frac{\partial^2 C_{t,i}}{\partial x^2} - \frac{\partial C_s}{\partial t}, \tag{7.6}$$

where the sink term is the rate of the C_s atoms that have been released from the ith trap type after each diffusion time step. We take the coefficient D to be the same Frauenfelder coefficient for the diffusion of solute atoms because traps are in equilibrium with the solute atoms arriving to these traps when equation (7.5) holds. Also note that D is constant with constant temperature, so it has been pulled outside of the derivative. Formulating the problem in terms of the evolution of the concentration of occupied traps, $C_{t,i}$, allows straightforward comparison of the model to the trapped inventory depth profile from NRA data. This is valid as long as the trapped inventory profile does not change significantly after the plasma treatment has ended.

Solving equation (7.5) for C_s and using the result in (7.6) with the unitless values $C_i = \frac{C_{t,i}}{C^0_{t,i}}$ and $R_i = \frac{\alpha_{r,i}\lambda^2 N_W}{DC^0_{t,i}}$, we now have, after some simplification,

$$\frac{\partial C_i}{\partial t} = D\frac{\partial^2 C_i}{\partial x^2} - \frac{\partial}{\partial t}\left(R_i \frac{C_i}{1-C_i}\right)$$

$$\frac{\partial C_i}{\partial t} = D\frac{\partial^2 C_i}{\partial x^2} - \frac{R_i}{(1-C_i)^2}\frac{\partial C_i}{\partial t}$$

$$\left(1 + \frac{R_i}{(1-C_i)^2}\right)\frac{\partial C_i}{\partial t} = D\frac{\partial^2 C_i}{\partial x^2}$$

$$\frac{\partial C_i}{\partial t} = D_{t,i}\frac{\partial^2 C_i}{\partial x^2} \tag{7.7}$$

$$D_{t,i} = \frac{D}{1 + {R_i}/{(1-C_i)^2}}. \tag{7.8}$$

Equation (7.8) is the effective diffusion coefficient for the diffusion of $C_{t,i}$ that

depends on the trapping energy, $E_{t,i}$, the distribution of the defect density in the material, $C^0_{t,i}$, and is a function of the normalized trapped concentration, C_i. Equation (7.8) indicates that as trap type i approaches saturation (i.e. $\frac{C_{t,i}}{C^0_{t,i}} = C_i \to 1$), the diffusion of this trap type approaches zero, meaning that, at least in this idealized model, C_i ceases to diffuse. Recalling that our constraint on $C^0_{t,i}$ requires $C_i < 0.95$ for the trapping rate to remain much greater than the diffusion rate which in turn allows the local equilibrium condition to remain valid.

Initial and boundary conditions are required to find solutions to (7.7). Initially, all traps in the material are unoccupied, and the semi-infinite boundary conditions are

$$C_i\left(x = 0, t > 0\right) = 1 \tag{7.9}$$

$$C_i\left(x \to \infty, t > 0\right) = 0. \tag{7.10}$$

Condition (7.9) states that instantaneously after the experiment starts, trap type i is completely filled at $x = 0$. It is important to point out that we define $x = 0$ as the implantation depth of the plasma ions because, as previously mentioned, we do not want to consider surface effects. Therefore, (7.9) is stating that the defects are saturated in the implantation region throughout the experiment. This condition is resonable given the large plasma fluxes in our experiments. We can estimate the cross-sectional area of one trap to be $\pi\lambda^2$ and estimate the sum of the densities from all trap types to range from 10^3 to 10^4 ppm. Since the plasma flux is 4×10^{20} ions/m^2/s, then condition (7.9) is satisfied in our experiment in 0.8 to 8 seconds, where the total time to reach the 10^{24} ions/m^2 fluence used in our experiments is 2500 sec. Condition (7.10) is applicable in our experiments because of the thickness of our samples and the temperature during plasma exposure. If we assume no trapping and extrapolating the Frauenfelder diffusion coefficient down

to 380 K, then the maximum distance solute atoms can diffuse is about 70 μm after 2500 sec of plasma exposure. Since our sample thickness is 2 mm, condition (7.10) is reasonable. These initial and boundary conditions allow for Boltzmann's transformation $\xi = {}^{x}/_{2\sqrt{t}}$ of the independent variables that simplifies (7.7) into an ordinary differential equation

$$D_{t,i}\frac{d^2C_i}{d\xi^2} + 2\xi\frac{dC_i}{d\xi} = 0. \tag{7.11}$$

The solution for $C_i(x,t)$ can now be obtained using a simple numerical method. We use a numerical boundary value problem solver that implements Simpson's rule that requires an initial approximate solution before numerical integration. An appropriate initial solution is the complementary error function, which is the solution of (7.11) when the diffusion coefficient is constant (i.e. $D_{t,i} = \frac{D}{1+R_i}$ in the limit that $C_i \sim 0$). Then integration can proceed using $D_{t,i}$ as defined in (7.8). Once the solutions for all i traps are found, the sum of their solutions will give the total inventory profile

$$C^{\mathrm{tot}}(x, t_{\mathrm{exp}}) = \sum_{i=1}^{21} C_{t,i}(x, t_{\mathrm{exp}}), \tag{7.12}$$

where $t = t_{\mathrm{exp}}$ is the plasma exposure time. The concentration C^{tot} can be compared to NRA D concentration profiles. Figure 7.4(a) shows the solutions after some time, t_{exp}, using the DFT energies shown in figure 7.2 and the best fit choices (explained in section 4.2) for C_{gb}, C_{dis}, and C_{vac} for each GB vacancy, dislocation, and in-grain monovacancy densities, respectively. The resulting total inventory profile is also shown by the red curve. We will fit the total inventory profile to the NRA data using the defect densities. The higher energy traps fill much faster

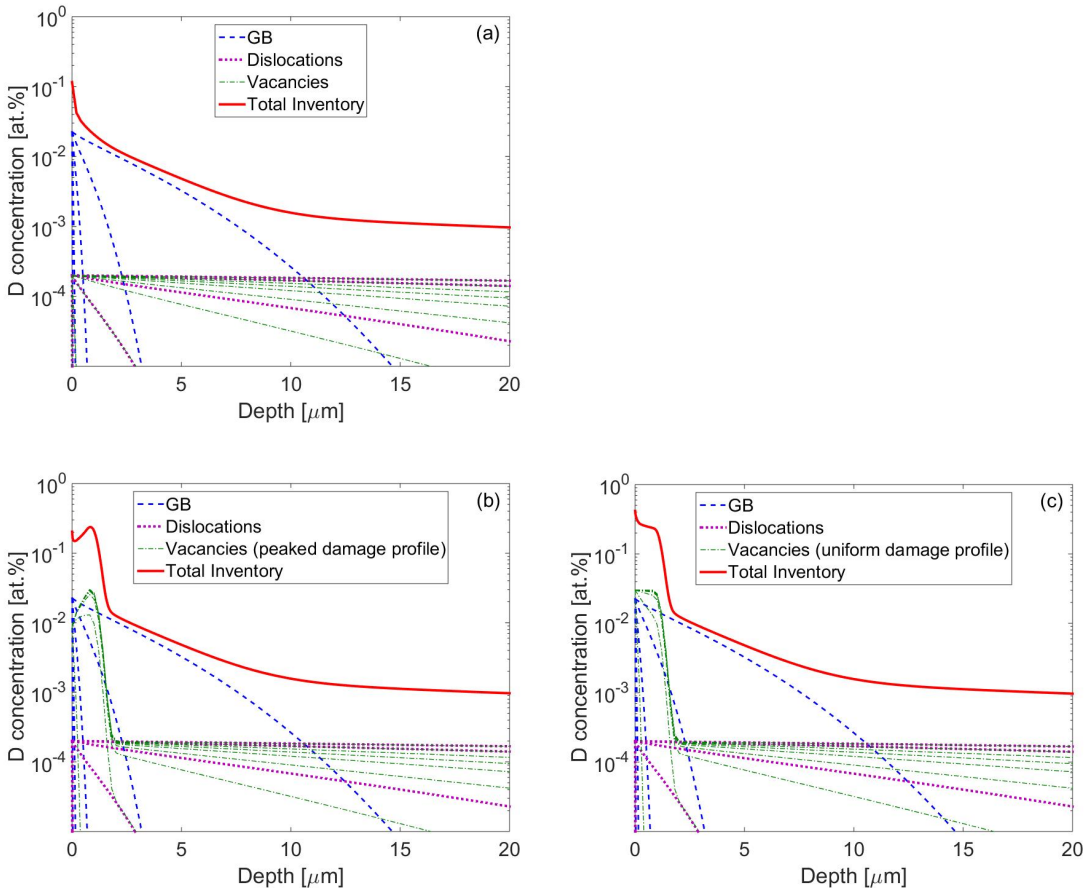

Figure 7.4: Individual solutions to equation (7.11) for each i trap type and the total inventory profile for: (a) an undamaged sample for best fit choices of C_{gb}, C_{dis}, and C_{vac} to our data, which is presented in section 4.2; (b) a sample with a peaked damage profile, where $C_{\mathrm{vac}}(x)$ comes from the SRIM calculated spatial profile of vacancies induced by 5 MeV Cu^{+} for a calculated damage level of 10^{-2} dpa; and (c) a sample with a uniform damage profile, where $C_{\mathrm{vac}}(x)$ here is the same as in (b) but is taken to be the maximum peak value from the surface up to 0.8 μm. The DFT energies shown in figure 7.2 are used in all cases.

because their release rate is smaller, and these traps dominate the inventory profile at larger depths. Lower energy trap types, such as trap types associated with GB vacancies, fill much slower.

Displacement damage caused by neutrons can cause the production of new monovacancies uniformly throughout the W lattice. We assume that the dominant defects introduced to our samples from ion-beam induced displacement damage are in-grain monovacancies [106]. At our temperatures, the W interstitials produced can freely migrate [72]. They can either migrate to a vacancy, removing a Frenkel pair, or remain as an interstitial, which we will not treat as a trapping site. Additional defect creation by the migration and merger of monovacancies, into di-vacancies and larger voids, is neglected because the temperature during irradiation is well below the stage III recovery temperature in W (570 K) where monovacancies are able to migrate to form larger vacancy clusters [102]. The increased number of monovacancies is modeled by treating the monovacancy defect density C_{vac} as a free parameter. Then the retention in damaged samples can be modeled with equation (7.11) by simply changing the value of C_{vac}. However, the defects caused by ion damage have a spatial variation due to the limitations on the ion's implantation depth, and thus $C_{\mathrm{vac}}(x)$. We will leave GB vacancy and dislocation defect densities unchanged from the values determined by fitting the model to retention profiles in undamaged samples. Since we expect that there are no new types of defects introduced by the displacement damage process other than monovacancies [107], the trapping energies of all trap types are assumed to be unchanged from the values computed by DFT for undamaged W materials. Thus, the only free parameter available to model retention after ion damage is the monovacancy defect density. The monovacancy density, C_{vac}, will be calculated by the sum of $C_{\mathrm{vac,int}}$, the defect density of intrinsic vacancy traps before ion damage taken

from the fit to an undamaged sample and $C_{\mathrm{vac,dam}}(x)$, the depth dependent defect density after ion damage. For the peaked damage profile, the $C_{\mathrm{vac,dam}}(x)$ is taken from the SRIM calculated vacancy distribution. For the uniform damage profile, the same profile is used except that $C_{\mathrm{vac,dam}}(x)$ is taken to be the maximum peak value from the surface up to the distance that peak value is reached, $\sim 0.8\ \mu m$. Figures 7.4(b) and 7.4(c) show the individual solutions and total inventory profiles after a calculated displacement damage level of 10^{-2} dpa for a peaked and uniform damage profile, respectively. The individual GB and dislocation profiles remain the same, but the new profiles for vacancy trap types significantly change the total inventory profile near the surface.

7.4 Results and discussion

7.4.1 Experimental results

The D concentration profiles obtained from NRA measurements for both the peaked and uniform damage samples are shown in figure 7.5. The retention profile of the undamaged W sample for this temperature is similar to previous NRA experiments [97]. Most of the D inventory for all damage levels is contained between the surface and a depth of about 1.5 μm; beyond that depth almost all of the samples have the same concentration profile within the experimental error of $\pm$20 percent. Therefore in the region $< 1.5\ \mu m$ in depth, where the retention profile has the largest changes to its concentration from layer to layer, the differences of the D retention profiles due to displacement damage are observed.

Retention with a peaked damage profile caused by a 5 MeV Cu ion beam increases with dpa, as expected. The samples with uniform damage also have increased retention with dpa. Figure 7.5 shows the percent increase in retention

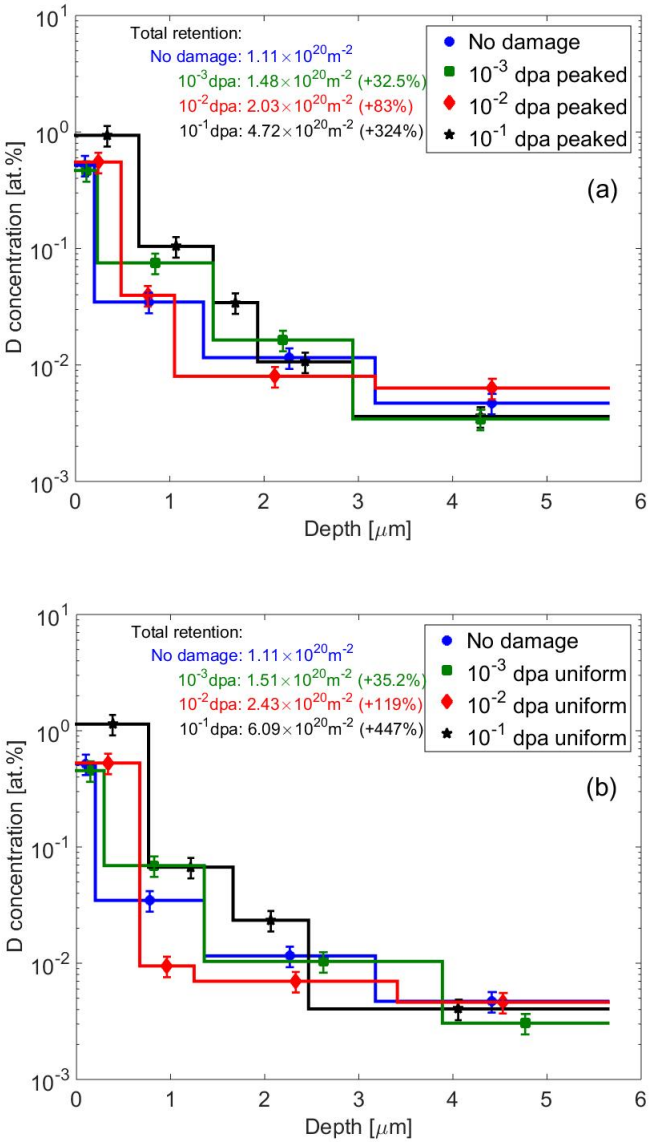

Figure 7.5: D concentration profiles for peaked (a) and uniform (b) damage with increasing levels of dpa. The control sample containing no damage is shown in both cases for reference. Error bars are ±20% due to experimental error.

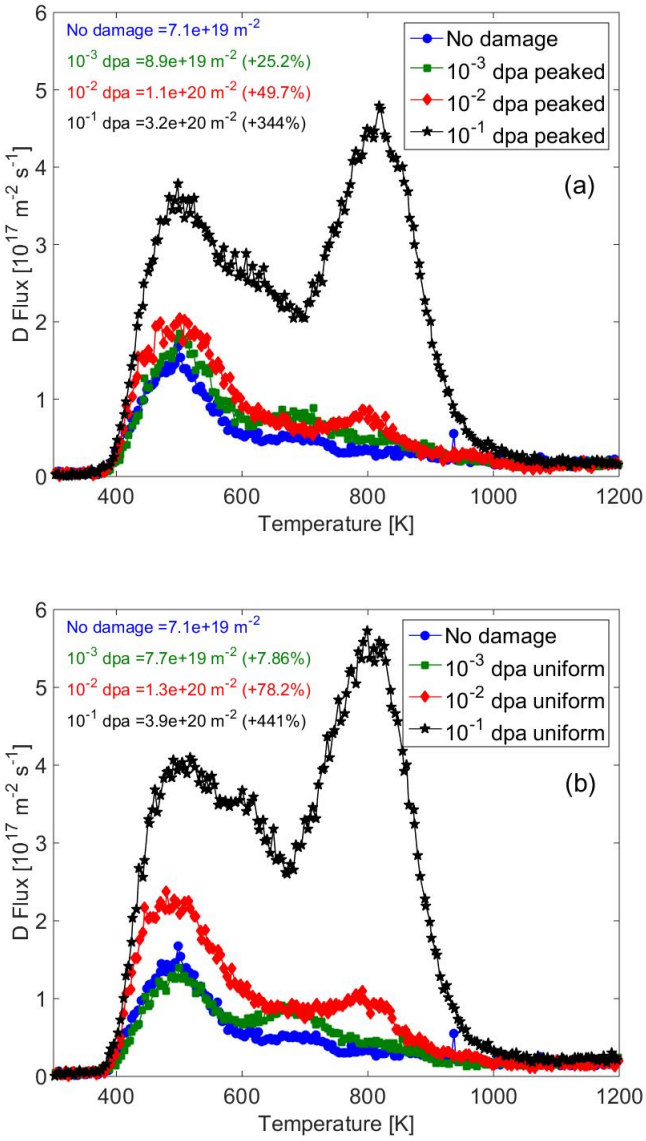

Figure 7.6: Comparison of D flux temperature traces for increasing levels of dpa for peaked (a) and uniform (b) damage profiles.

from the undamaged case. According to these data, a factor of ten increase in dpa does not increase the retention by a factor of ten, indicating that a linear relationship may not exist between the increase in retention due to displacement damage and dpa. The TDS data from the samples (fig 7.6) also reproduces these NRA retention trends, but the values for the total retention are different for the two measurement techniques. These differences could be explained by the fact that TDS measurements were taken 1-2 weeks after NRA, where room temperature desorption at atmospheric pressure could have occured, lowering the D inventory [108]. The total retention calculated from TDS has an error of about ± 20 percent as well, and again we observe a non-linear increase in retention with dpa (i.e. increase in retention $\propto$ dpa^x, $x < 1$). TDS results from both peaked and uniform damage cases have significant increase in retention with dpa, and again we see that a factor of ten increase in dpa does not produce a factor of ten increase in retention. Figure 7.7 shows the non-linear power-law relationship between the percent increase in total D retention from an undamaged sample and dpa. Taking both the NRA and TDS measurements into account, the increase in retention for a peaked damage profile is $\propto$ dpa$^{0.66}$, and for the uniform damage profile, the retention increases $\propto$ dpa$^{0.65}$. A non-linear power-law relationship between retention and dpa from self-damaged W has been previously reported [60] where maximum retention was reached by 0.2 dpa. If we assume that D occupied vacancies are saturated [38] so that D retention can be used as a proxy for the number of vacancies induced by ion damage, then this indicates that the actual number of vacancies per unit Cu ion fluence is lower than what is calculated by the SRIM code. This relationship between retention and dpa will affect how we use SRIM to calculate the number of vacancies induced by ion damage, discussed in the next section.

There are two clear peaks in the TDS data in both peaked and uniform

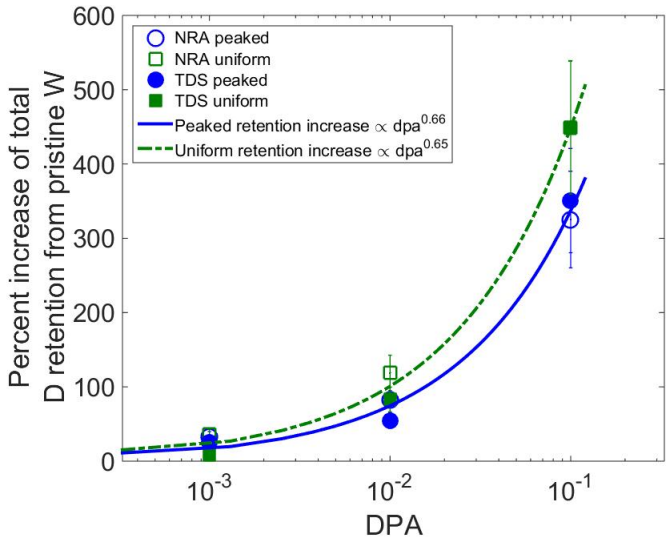

Figure 7.7: Percent increase in D retention from a pristine W sample with dpa. Samples that have a peaked damage profile are the circles, and samples that have a uniform damage profile are squares. The empty and filled markers indicate retention measured by NRA and TDS, respectively. The curves are fits to the average value of the percent increase in dpa measured by both NRA and TDS.

damage samples around 500 K and 800 K (fig 7.6) that increase in magnitude as dpa increases. These peaks may be due to an increase in defect densities, like in-grain monovacancies, introduced from ion damage. By extending our model to include non-constant temperature, we could in principle verify which defects are responsible for these peaks, since trapping energies are fixed in our model. However, these peaks could also represent other phenomena where traps need to be defined dynamically, since during the TDS procedure, the sample temperature is raised well beyond 570 K. Empty vacancies are mobile at this temperature and can merge, and phenomena like the mobility of D filled traps introduce additional modeling challenges. We can at least see that these peaks around 500 K and 800 K are consistent with defects where multiple trapping energies are around two distinct ranges that correspond to the two release temperatures. Looking at the trapping energies from DFT (fig 7.2), 6 of the monovacancy trapping energies are

within 10 percent of 1 eV. This close grouping of trapping energies is consistent with releasing atoms from traps with nearly the same trapping energy at close to the same temperature during TDS. As the monovacancy density increases with ion damage, the D flux peak around this temperature would increase, as observed in the TDS data.

Comparing samples with uniform damage to the analgous peaked damage profiles (fig 7.8), the shape of the NRA retention profiles as well as their total retention are similar. It is interesting to see that the shape of the damage profile does not significantly affect the shape of the retention profile, since the layer thicknesses were chosen by statistical software [104] based on the shapes of the proton spectra. The increase in retention in the 10^{-3} and 10^{-2} dpa cases are both within the experimental error, so they are approximately the same. The 30 percent increase in total displacements predicted by SRIM is consistent with the 29 percent increase of retention in the 10^{-1} dpa case, but we otherwise see no significant difference between samples with peaked and uniform damage profiles in the NRA data.

The TDS results comparing peaked and uniform damage at each dpa (fig 7.9) also show no significant differences. The total retention is within the experimental error, and the D flux profiles are nearly identical. The peaks are located at about the same temperatures for the two damage profiles, showing that the shape of the damage profile does not appear to significantly affect D migration up through the surface during a TDS temperature ramp.

7.4.2 Model comparison to data

Using three defect densities, we model the retention profile in our undamaged W sample (fig 7.10). The exact trapping energies reported by DFT models

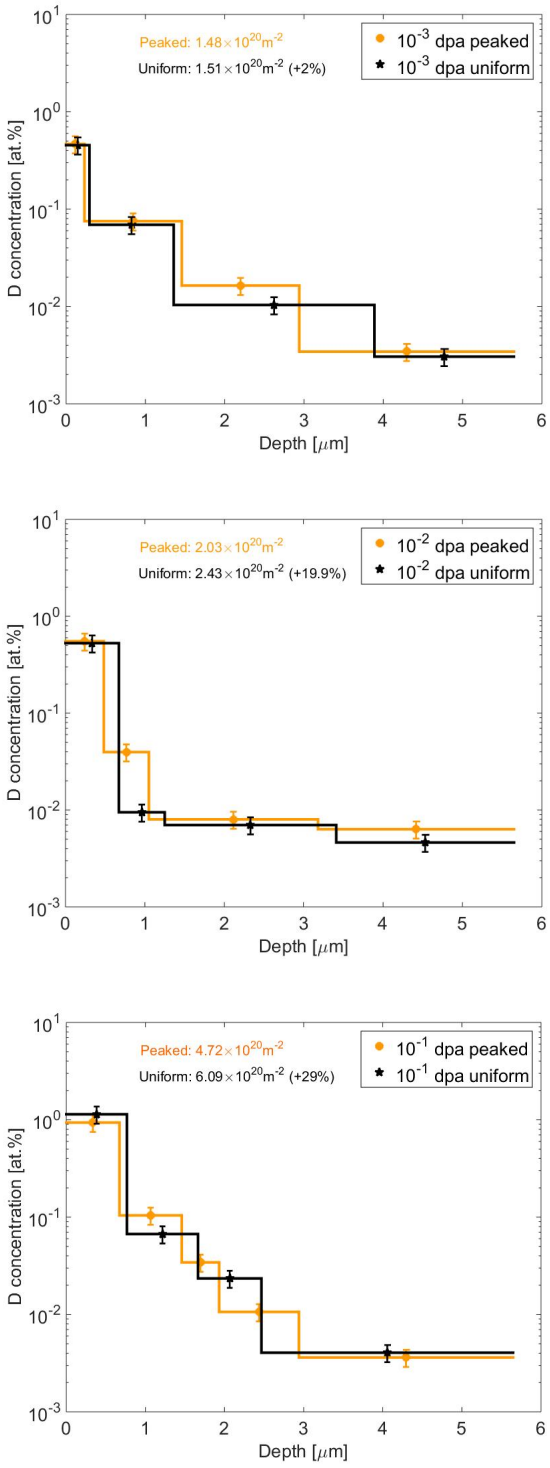

Figure 7.8: D retention depth profiles comparing peaked and uniform damage profiles for each dpa level. The value of total retention is shown on each plot.

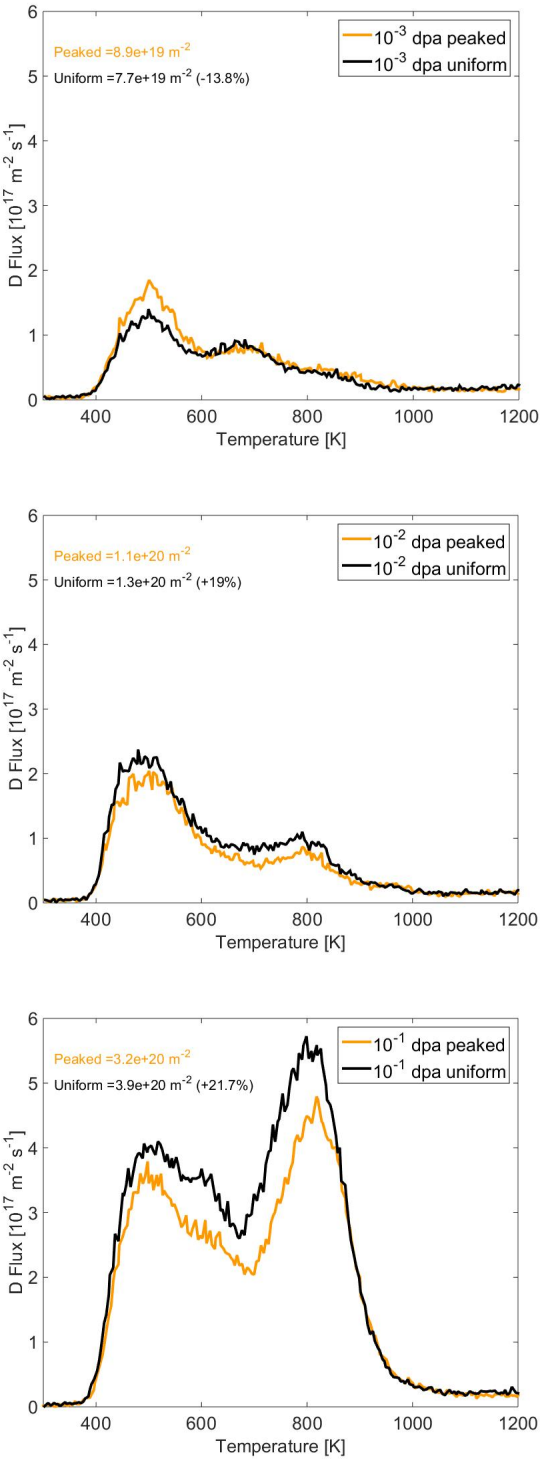

Figure 7.9: D flux temperature traces comparing the damage profile type for each dpa level. The value of total retention is shown on each plot.

tend to differ depending on the conditions of their simulation; however, we did not wish to include these energies as free parameters. First let us examine the choice of defect densities used to fit our NRA data. Due to the large number of grains - and therefore large number of GB vacancies - expected in the as manufactured W samples [103], we expect that the GB defect density to be significantly larger than intrinsic in-grain monovacancy and dislocation densities in undamaged samples. The simulated retention profiles due to GB trap types do not extend very far into the material (see fig 7.4(a)). The defects with larger trapping energies, however, saturate well beyond our measurement depth, 5.6 μm. We then choose C_{gb} to reflect the sloping D concentration in the first 3 μm from the surface and choose C_{dis} and C_{vac} to make up the lower background D concentration trapped deeper in the material. The intrinsic GB vacancy density resulting from this procedure and used to fit our data was 225 ppm for each of the five different GB trap energies. The intrinsic dislocation and vacancy defect densities were both 2 ppm. Since we do not know which of these two densities is more prevalent in our samples, we chose C_{dis} and C_{vac} to have the same value. Thus the total defect density in the material due to 21 trap types is 1157 ppm, which is a sufficient density of traps to satisfy the surface boundary condition in equation (7.9) and is similar to the density used in other models [100]. These intrinsic defect densities are then fixed for all subsequent modeling in this work.

Our model fails to capture the D concentration in the first layer (fig 7.10), but fits the rest of the measured profile reasonably well. Experimental resolution prohibits increasing the number of SIMNRA D concentration layers in the region of the first layer ($< 0.2\ \mu m$) during the proton spectrum deconvolution. Therefore, we need to measure the alpha particles from the reactions near the surface in future experiments to possibly increase resolution in this region. Having more than one D

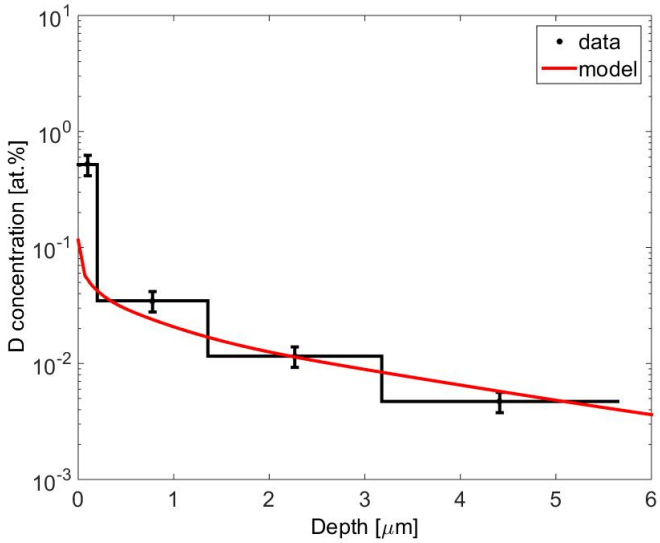

Figure 7.10: D concentration profile of a pristine W sample measured by NRA and the total trapped inventory profile, C^{tot}, calculated with the model. Each trap type is defined by a trapping energy and a trap density. The trapping energies are given in figure 7.2, with five GB traps $C_{\mathrm{gb}} = 225$ ppm, six dislocation traps $C_{\mathrm{dis}} = 2$ ppm, and ten vacancy traps $C_{\mathrm{vac}} = 2$ ppm.

concentration layer in this region would more clearly show the rapid decrease of the D concentration profile near the surface. We could then examine why the model underestimates retention in the first 0.2 μm. The model nevertheless captures the bulk diffusion beyond 0.2 μm and retention well.

Now that we have fixed the intrinsic defect densities of the as-manufactured material in the model, we re-examine the relationships among the trapping, release, and diffusion rates (see fig 7.11). The local equilibrium condition (7.5) that requires $\alpha_{t,i} \gg {}^{D}/_{l^2_{\mathrm{mfp}}}$ is satisfied for all trap types because each trap type is much less than 1300 ppm, so this inequality holds for each trap type until more than 95 percent of this trap is filled. Incidently, this inequality is also satisfied at all temperatures. The release rates, $\alpha_{r,i}$, also need to be significantly greater than the diffusion rate, ${}^{D}/_{l^2_{\mathrm{mfp}}}$, during the time scale of diffusion between traps (see section 3 cases B or C). Examining the rates in figure 7.11, we see that these conditions on the release

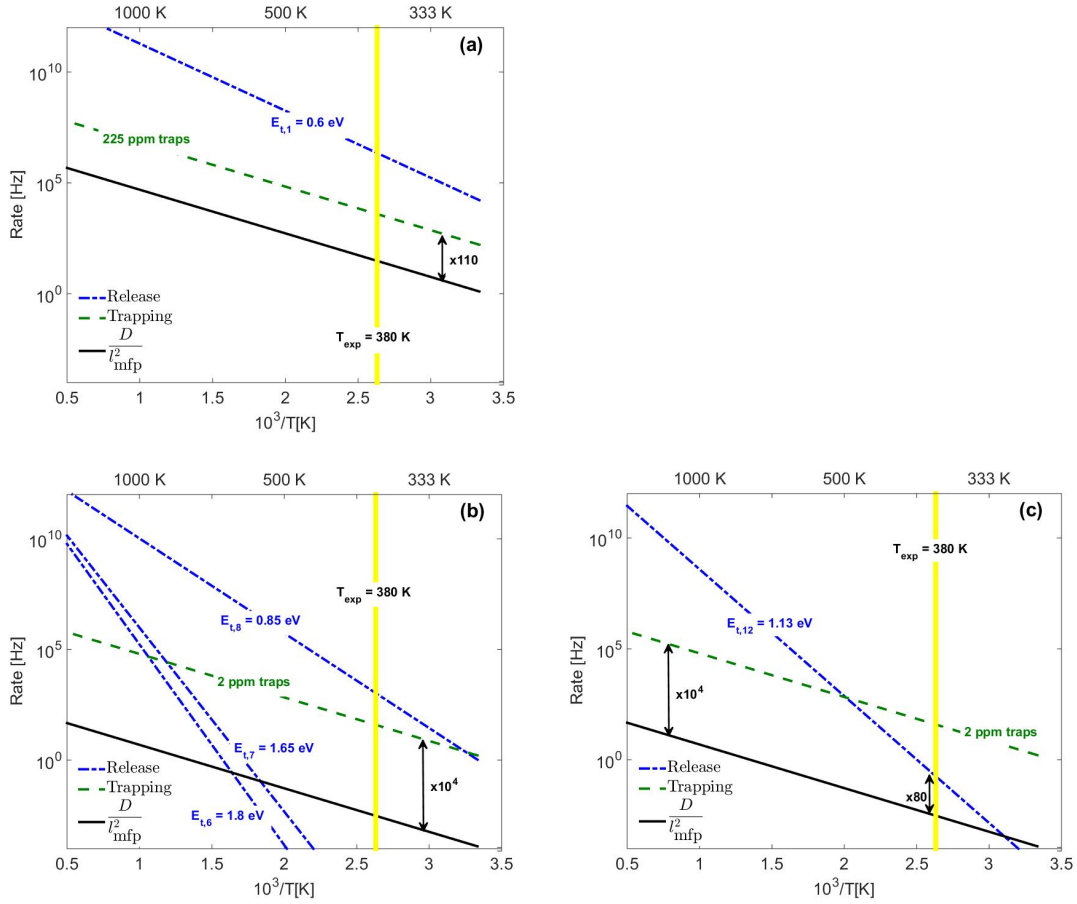

Figure 7.11: Trapping ($\alpha_{t,i}$), release ($\alpha_{r,i}$), and diffusion ($^{D}/_{l^2_{\mathrm{mfp}}}$) rates for relevant trap types in (a) GB vacancy, (b) dislocation, and (c) in-grain monovacancy defects. Only the release rates with the largest (most relevent) trapping energies are shown. The trapping rates are for 0 percent traps filled, and the yellow band indicates the temperature during plasma exposure for these experiments.

rate are satisfied for all trapping energies, except for the release rates due to the two largest trapping energies in a dislocation defect (fig 7.11(b)). However, the release rate can also be much lower than the diffusion rate, where the trapped concentration is not likely to release atoms to solution (see section 3 case A). This means that the sink term in (7.6) is negligible. At our experimental temperature, this condition is satisfied by the two largest trapping energies in a dislocation defect. Therefore with our choices for the defect densities, all trapping energies satisfy the conditions allowing for the local equillibrium condtion to be valid.

We account for damage effects by adding the SRIM prediction for the displacement damage vacancy profile to our intrinsic vacancy defect density, $C_{\text{vac}}(x) = C_{\text{vac,dam}}(x) + C_{\text{vac,int}}$. We saw from our experimental results presented earlier that the number of vacancies calculated from the SRIM prediction of dpa seems to over estimate the actual number of vacancies. SRIM models the damage cascade and relaxation of lattice atoms in a pristine material resulting from the impact of one energetic ion at a time with no memory of previous cascades and with no thermal effects like self annealing. Thus, SRIM provides a depth resolved probability density of ion damage effects like the number of vacancies and the stopping range of Cu ions during ion irradiation at 0 K, so that damage effects are fixed. This is what is used to find the depth profile of vacancies for a given Cu ion fluence. However, the effects of damage saturation [60], where creating a new vacancy subsequently fills another vacancy due to high ion fluences, and the effects of self annealing, where stage I recovery due to the migration of interstitial W atoms to vacancies can occcur with temperatures > 27 K [72], are not included in the calculation, so the number of vacancies are inherently overestimated. A recent report [109] suggests modifications to the SRIM code, such as using the "Quick" Kinchin and Pease option instead of the "Detailed" calculation used in this study, that reduced

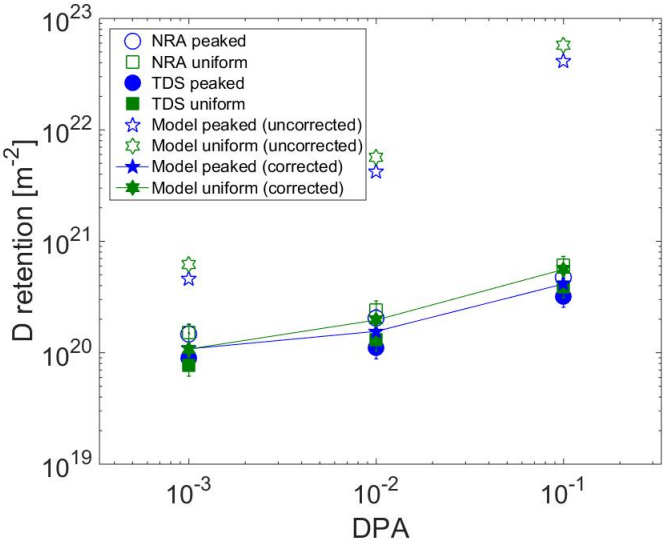

Figure 7.12: Total D retention in W for three levels of ion-induced displacement damage with peaked or uniform damage profiles from experimental measurements and from the model. The retention values from the model using the exact calculation for the number of vacancies per Cu ion are the open stars, and the closed stars with connecting lines are the values from the model after reducing the number of vacancies to reflect experimental retention measurements.

the number of vacancies predicted in self-damaged Fe closer to the vacancies predicted with a full molecular dynamic simulation; however, the SRIM prediction with these modifications still overestimates the number of vacancies by some significant factor. While SRIM is efficient at calculating dpa (a statistical description of the displacement of lattice atoms), it is not accurate enough to estimate realistic vacancy densities in metals at room temperature, given an ion fluence.

We find that we must constrain the number of ion-induced vacancies produced by increased ion beam fluence. Provided that this constraint is applied, our model can reproduce the total retention as found in the experiment. Refering to the open stars in figure 7.12, we see the large discrepancy between measurements and modeling of the total retention if we use the exact SRIM profile for the number of vacancies produced per Cu ion (i.e. $C_{\mathrm{vac,dam}}(x) = N_{\mathrm{vac}}(x)\phi_{\mathrm{Cu}}$, where N_{vac} is the SRIM prediction for the density of vacancies per Cu ion fluence and ϕ_{Cu} is the Cu

ion fluence). Without reducing the number of vacancies SRIM predicts, then our model shows that retention increases linearly with dpa and significantly overestimates the retention. We made corrections to this vacancy density prediction by defining $C_{\mathrm{vac,dam}}^{\mathrm{corrected}} = C_{\mathrm{vac,dam}}/q$, where q is some correction factor, so that the total retention given by our model was the same as our NRA measurements (seen as closed stars in the figure).

Figures 7.13 and 7.14 show the resulting fits of the model to NRA D concentration profile data with the undamaged retention data for reference. In the peaked damage model (fig 7.13), the predicted SRIM vacancy profile was reduced by using $q = 4$, 27, and 99 to fit the 10^{-3}, 10^{-2}, and 10^{-1} dpa samples, respectively. Similarly in the uniform damage model (fig 7.14), the SRIM vacancy profile was reduced by using $q = 6$, 29, 102. These values of q reflect the fact that vacancy production - and therefore D retention - does not increase linearly with dpa. This suggests that partial vacancy healing by subsequent displacement cascades and by interstitial migration at our experimental temperatures is occuring and must be taken into account for any predictive modeling of retention.

In the previous section, we discussed that we do not see a significant dependence of the NRA retention measurements on the shape of the damage profile. In the D retention model, however, we can clearly see differences in the peaked and uniform damage profiles due to $C_{\mathrm{vac,dam}}(x)$ (figs 7.13 and 7.14). We speculate that room temperature annealing of the defects could have diminished the prounced peak damage profile. Comparing the two figures, the model captures increased retention in the damage region, while the retention profile beyond the SRIM predicted damage region remains unchanged. Since the features of retention after ion damage are only seen in the first two layers of the NRA measurements, this again motivates the need to increase the depth resolution of NRA near the surface or

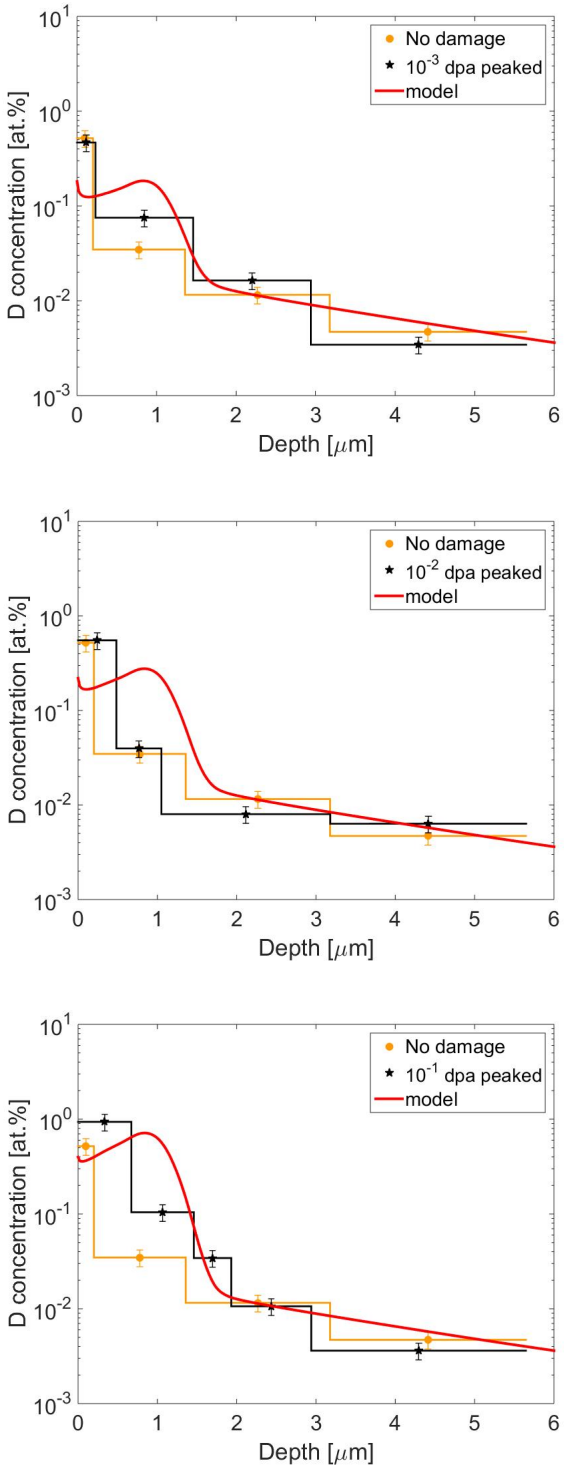

Figure 7.13: Retention model compared to retention measurements in samples with peaked damage profiles for each dpa. The undamaged retention data are included for reference.

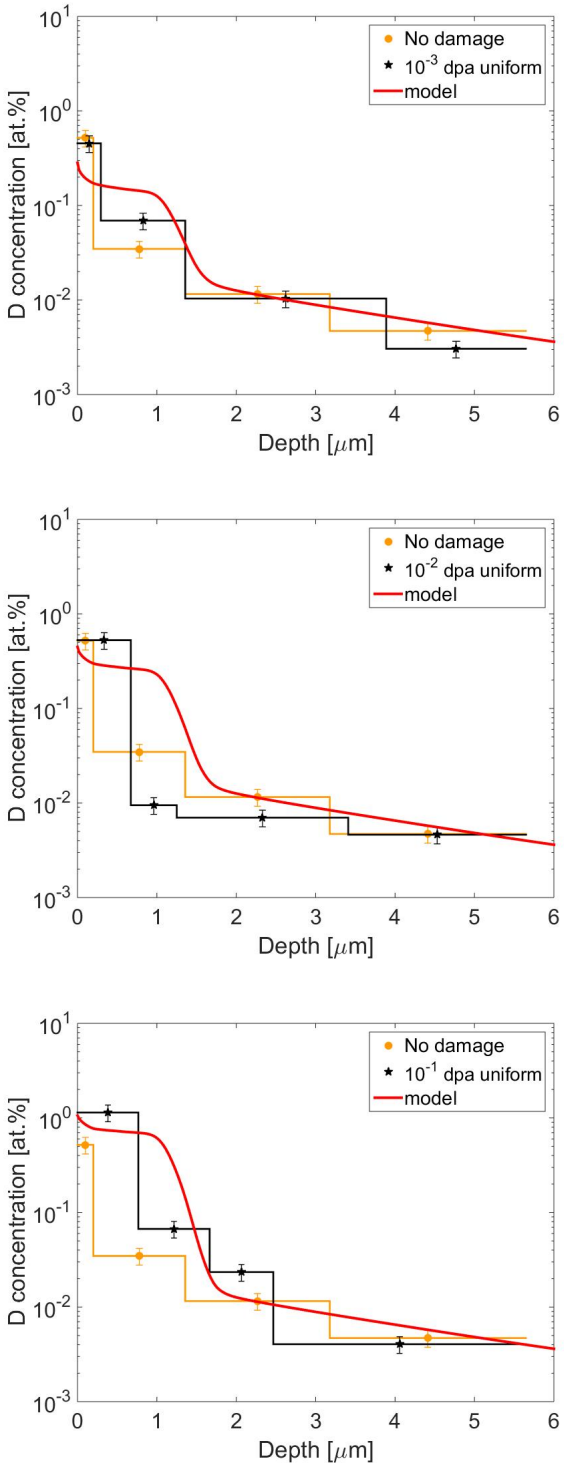

Figure 7.14: Retention model compared to retention measurements in samples with uniform damage profiles for each dpa. The undamaged retention data are included for reference.

use higher depth resolution techniques so that small features of the profile can be measured. Despite these limitations of the current dataset, the model captures the main features of retention after ion damage in this experiment, provided that the probability of SRIM vacancy production is reduced by the reported values of the parameter q.

7.4.3 Comparison of the model to measurements of the diffusion coefficient

The local equilibrium condition (7.5) not only decouples the effects of trapping from solute diffusion but also describes a direct relationship between the trapped and solute concentrations. The model, given by equations (7.6)-(7.8), describes how $C_{t,i}$ can be treated as a diffusing species when the local equilibrium condition is valid. This is useful for computing the trapped concentration profile after plasma exposure. Now we will use the local equilibrium condition to see how trapping affects the diffusion of the species in solution, C_s. The diffusion of the solute concentration, C_s, including the loss rate of solute atoms to all trap types is

$$\frac{\partial C_s}{\partial t} = D\frac{\partial^2 C_s}{\partial x^2} - \sum_{i=1}^{21} \frac{\partial C_{t,i}}{\partial t}. \tag{7.13}$$

To examine the effect each individual trap has on solute diffusion, let us simplify the analysis of equation (7.13) by looking at the effect of only one trap type

$$\frac{\partial C_s}{\partial t} = D\frac{\partial^2 C_s}{\partial x^2} - \frac{\partial C_{t,i}}{\partial t}, \tag{7.14}$$

similar to the discussion the previous sections. By employing equation (7.5) to re-write $C_{t,i}$ in terms of C_s and substituting into (7.14) we obtain

$$\frac{\partial C_s}{\partial t} = D\frac{\partial^2 C_s}{\partial x^2} - \frac{\partial}{\partial t}\left(\frac{C_s}{R_i + {}^{C_s}/_{C^0_{t,i}}}\right)$$

$$\left(1 + \frac{R_i}{\left(R_i + {}^{C_s}/_{C^0_{t,i}}\right)^2}\right)\frac{\partial C_s}{\partial t} = D\frac{\partial^2 C_s}{\partial x^2}$$

$$\frac{\partial C_s}{\partial t} = D_{s,i}\frac{\partial^2 C_s}{\partial x^2}, \tag{7.15}$$

$$D_{s,i} = \frac{D}{1 + {}^{R_i}/_{\left(R_i + {}^{C_s}/_{C^0_{t,i}}\right)^2}}. \tag{7.16}$$

where $D_{s,i}$ has absorbed the sink term. Using equations (7.5) and (7.8) this can be re-written as

$$D_{s,i} = \frac{D}{1 + {}^{(1-C_i)^2}/_{R_i}} = D - D_{t,i} \tag{7.17}$$

to show that $D_{s,i}$ has a non-linear dependence on the trapped concentration $C_i = {}^{C_{t,i}}/_{C^0_{t,i}}$. Equation (7.17) shows that the solute diffusion coefficient with trapping effects is equal to the diffusion coefficient without trapping, D, minus the diffusion coefficient of the trapped concentration, $D_{t,i}$. $D_{s,i}$ approaches the value of diffusion without traps because a saturated trap type i means that $C_i = 1$ and thus by equation (7.8) $D_{t,i} \to 0$. In other words, trap type i reduces its affect on solute diffusion as it approaches saturation. We note again, however, our constraint for this analysis to be valid requires $C_i < 0.95$ according to our estimates.

In order to compare to experimental measurements of the H diffusion coefficient, we would then need to derive $\mathscr{D}_s(C_i)$ such that

$$\frac{\partial C_s}{\partial t} = \frac{\partial}{\partial x}\left[\mathscr{D}_s\frac{\partial C_s}{\partial x}\right] \tag{7.18}$$

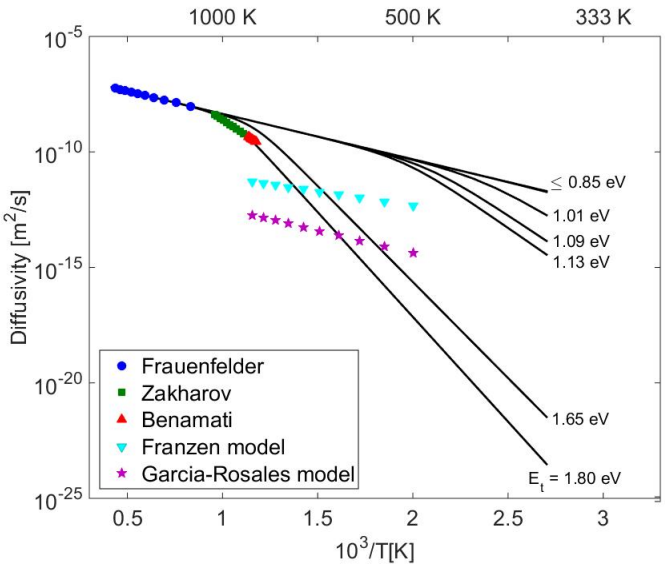

Figure 7.15: Measurements and empirical models (Franzen and Garcia-Rosales) of the H diffusion coefficient [18] and curves of $\mathscr{D}_s\left(C_i = 0\right)$ for various trapping energies.

for the total solute concentration including all i trap types, where $\Gamma_s = -\mathscr{D}_s\left(C_i\right)\frac{\partial C_s}{\partial x}$ is the Fick's Law flux of the total solute concentration. It is obvious to see that we cannot easily extract an effective diffusion coefficient in analytical form because of the summation in (7.13) and must resort to numerical evaluation in this case. We therefore defer the analysis of $\mathscr{D}_s\left(C_i\right)$ to future work.

However, for discussion purposes, we will examine the effect of a single trap type in the material when the trapped concentration is low, $C_i \sim 0$. For this case, (7.17) is constant can be brought inside the first derivative in (7.15) to give

$$\frac{\partial C_s}{\partial t} = \frac{\partial}{\partial x}\left[\frac{D}{1+R_i^{-1}}\frac{\partial C_s}{\partial x}\right]. \tag{7.19}$$

Since there is only one trap in the material, the effective diffusion coefficient is

$$\mathscr{D}_s\left(C_i = 0\right) = \frac{D}{1+R_i^{-1}}. \tag{7.20}$$

Curves of $\mathscr{D}_s\left(C_i = 0\right)$ are plotted in figure 7.15 for trapping energies and their respective defect densities used in the previous sections. To compare to diffusion measurements of H in W, the value of the coefficient D, when calculating $\mathscr{D}_s$ in this case, is the Frauenfelder value for H diffusion [99]. Measurements as well as empirical models for the H diffusion coefficient are also plotted in figure 7.15. The Frauenfelder diffusion coefficient extrapolated to lower temperatures is no different than the value of $\mathscr{D}_s$ with trapping energies lower than 0.85 eV because these trap types produce a $\mathscr{D}_{t,i}\left(C_i = 0\right)$ that is small compared to D. Although low energy trap types are significant in calculating retention, like GB traps, low energy traps seem to not effect solute diffusion. However, the 8 trap types associated with trapping energies greater than 0.85 eV and the intrinsic densities C_{dis} and C_{vac} reduce the value of $\mathscr{D}_s$ well below D, especially at temperatures less than 500 K. We see that the effect on solute diffusion from large energy trap types is to decrease the diffusivity of solute atoms. The trap type with $C^0_{t,6} = C_{\text{dis}}$ and $E_{t,6} = 1.8$ eV, produces $\mathscr{D}_s\left(C_6 = 0\right)$ that agrees with the diffusivities measured by Zakharov and Benamati [18], and along with the trap type $C^0_{t,7} = C_{\text{dis}}$ and $E_{t,7} = 1.65$ eV, $\mathscr{D}_s\left(C_6 = 0\right)$ and $\mathscr{D}_s\left(C_7 = 0\right)$ drop through the emperical models of Franzen and Garcia-Rosales at lower temperatures. The discrepancy between these two diffusivity measurements may be accounted for by our model when the trapped concentration is greater than zero because the value of $\mathscr{D}_s$ increases towards the value of D when the trapped concentration increases.

We include the effects of ion damage in our calculations of $\mathscr{D}_s$ by using the maximum value of the vacancy defect densities from our fits to NRA data and treat them as uniformly distributed throughout the material. Figure 7.16 shows the values of $\mathscr{D}_s(C_i = 0)$ for undamaged W as well as for a range of dpa levels. Here the $\mathscr{D}_s$ curves associated with vacancy traps are shown as dashed lines. The

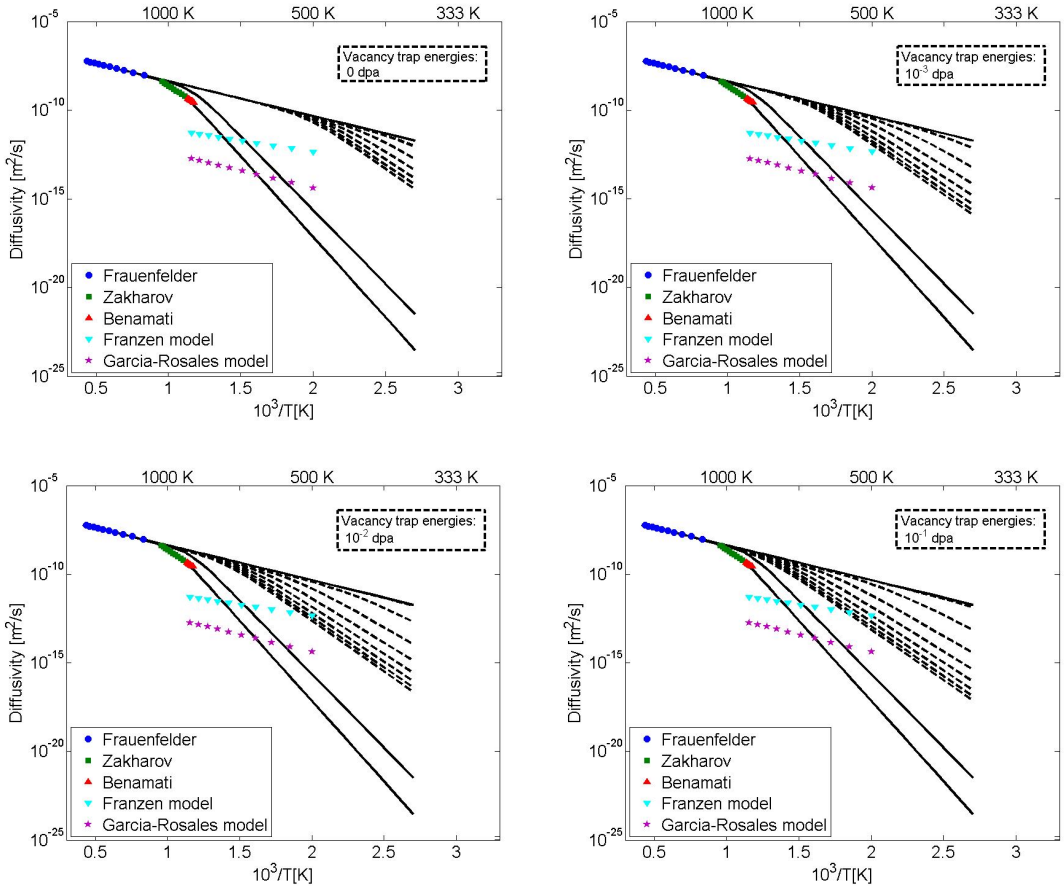

Figure 7.16: Measurements of the H diffusion coefficient [18] and curves of $\mathscr{D}_s\,(C_i = 0)$ for samples with no damage and with 10^{-3}, 10^{-2}, and 10^{-1} dpa. The $\mathscr{D}_s$ curves associated with all monovacancy trapping energies are dashed lines.

trapping energies of these vacancies have not changed; however, the defect density increases with increasing dpa. We now see that the defect density can significantly reduce individual $\mathscr{D}_s$ values at higher temperatures. The results in figure 7.16 show that having a higher density of high energy traps retard solute diffusion by removing more of the mobile concentration and require higher temperatures to overcome this effect. Thus, the $\mathscr{D}_s\,(C_i = 0)$ due to in-grain monovacancies is much lower after enduring displacement damage.

7.5 Summary

D retention profiles are studied in pristine and Cu ion damaged W. Three levels of damage (10^{-3}, 10^{-2}, and 10^{-1} dpa) were applied at room temperature to W samples with either a single 5 MeV Cu ion beam to produce a peaked displacement damage profile or 3 Cu ion energies (0.5, 2, and 5 MeV) to produce a uniform displacement damage profile up to 0.8 μm. These samples were then exposed to a high fluence of D plasma at 380 K. The D retention was measured using NRA to obtain concentration depth profiles as well as total retention up to the measurement depth and using TDS to measure total retention. The concentration profiles show retention increases with dpa in peaked and uniform damage with a power law dependence $\propto \text{dpa}^{0.66}$ and $\propto \text{dpa}^{0.65}$, respectively.

The SRIM program predicts 30 percent more displacements in the uniform damage profile, but this difference is not observed in the retention data. Both NRA and TDS data show that samples with uniform damage have about the same total retention as peaked damage samples within the experimental error of ± 20 percent. We also see that the D depth profiles from NRA have the about the same shape regardless of peaked or uniform damage, and the TDS data has D flux peaks at about the same temperatures regardless of peaked or uniform damge. This is a

useful finding for modeling damage because it seems that the shape of the damage profile has little effect on D retention.

To understand the observed trends in NRA data, a model was developed to elucidate diffusion and trapping effects. We use the descriptions of trapping and release rates from a previous model [96], but make an observation that these rates in W are significantly different than the diffusion rate between traps. Using this we justify a direct proportionality of the trapped inventory of D atoms to the solute concentration of atoms released from the trap. With this simplification, we are able to write down an equation for the filling evolution of each trap type and solve each independently. By implementing trapping energies calculated from DFT models, we reduced the number of free parameters to the defect densities of GB vacancies, dislocations, and in-grain monovacancies. These parameters are used as the three fitting constants to our NRA measurements.

The model was able to reproduce the NRA D depth profile from pristine W. The intrinsic GB vacancy, dislocation, and in-grain monovacancy defect densities we then fixed in subsiquent modeling of retention in displacement damaged samples. A key observation, however, is that SRIM over-estimates the number of vacancies produced, so we were forced to reduce the number of vacancies predicted by SRIM in order to reproduce the same total retention. This is implemented by a correction factor that is proportional to the damage level, dpa, that is then multiplied to the SRIM predicted number of vacancies created by ion damage, and this is added to our intrinsic monovacancy defect density. This correction was sufficient to reproduce the retention profiles in displacement damaged W. We capture the increase in retention in the damaged region, while the inventory beyond the damage region ($\sim 0.8\ \mu m$, given by SRIM) remains unchanged from the retention profile of a sample with no damage.

We discuss the effect each trap type has on the diffusion coefficient for the solute concentration at a low trapped concentration (i.e. $C_{t,i} \sim 0$) and observe that this may resolve some descrepancies in previous diffusivity measurements. Using the trapping energies from the DFT literature, we observe that trapping energies equal to or less than 0.85 eV do not affect solute diffusion. When there is a large number of available high energy traps, the diffusion coefficient, $\mathscr{D}_s$, is several orders of magnitude lower than the Frauenfelder diffusion coefficient extrapolated to all temperatures. According to our analysis the value of $\mathscr{D}_s$ ($C_i > 0$) should approach the Frauenfelder value as these traps become filled because there are less traps available to hinder solute diffusion. Increasing the density of high energy traps with displacement damage decreases diffusivity due to the increased probability of finding these traps. Therefore we see a reduction of $\mathscr{D}_s$ at the front of solute concentration moving through a virgin W sample.

Although we have derived a simplified model, it seems to capture the dominant physics of trapping and diffusion of D in W and provides theoretical corroboration of a range of previous diffusivity measurements. This model is not, in principle, only for W materials but any material where the local equilibrium condition applies during hydrogenic diffusion.

Acknowledgements

The work in this chapter was supported by the U.S. Department of Energy under DE-SC0001999 and DE-FG02-07ER54912 and the University of California Office of President Research Fund under Award Number 12-LR-237801. This chapter has been submitted for publication to Nuclear Fusion in March 2016. The authors are J. L. Barton, Y. Q.Wang, R. P. Doerner, G. R. Tynan. The dissertation author was the primary investigator and author of this paper.

Chapter 8

Summary and future work

8.1 Summary and conclusions

The experiments presented here give meaningful contributions to the understanding of trapping and diffusion of H isotopes in W. There were two main physical processes that were studied: H isotope exchange and ion induced displacement damage. The key physics and engineering questions were

1. Can isotope exchange be an efficient T removal technique, even in the face of neutron damage, and what can it teach us about atomic diffusion?

2. How does trapping and diffusion change as a result of displacement damage?

With a combination of experiments and modeling, these questions were addressed with quantitative results.

The isotope exchange experiments showed significant reduction in the D inventory in first few microns from the surface, but showed very little change in D inventory deeper in the bulk of W. Therefore the experimental results show that isotope exchange is too inefficient for T removal beyond the near surface region of the PFCs. Adapting the Doyle model for isotope exchange [98] to the

simplified diffusion model illuminated the trapping physics that prevent isotope exchange from removing all of the implanted D. We see that low energy traps can release trapped D atoms more easily so that an H atom can take its place, but high energy traps retain D atoms more efficiently, reducing the likelihood of exchange. The trapping energies seem to be the dominant effect that prevent more complete isotope exchange, and the modeling results are in good agreement with this evaluation. We speculate that by including the calculation of D atoms diffusing after they were exchanged from their initial trap sites, we may have a more acurate prediction for the isotope exchange rate. However, this modification of the model has been left for future work. At any rate, this modeling exercise has shown us that the trapped concentration plays an important role in diffusion, since the exchanging H atoms that become trapped do not penetrate very far into the W sample. This analysis of the trapped concentration is investigated further with displacement damage experiments and modeling.

Energetic Cu ions cause damage cascades similar to how energetic neutrons would, and this leaves behind a W lattice that has an increased number of defects to trap D atoms. Thus, we see a clear D retention increase in this region of damaged samples. Another effect of increased defect density is that isotope exchange has a reduced exchange rate because there are more D filled defects. We also see that retention does not increase linearly with the damage level. In particular, we found that the increase in retetion follows a power law relationship with the damage level calculation $\propto \mathrm{dpa}^{0.66}$. This suggests that damage recovery needs to be considered (i.e. an accurate defect density estimate is required) in order to make quantitative predictions of retention in a fusion reactor environment.

With the experimental knowledge gained from these types of experiments, the simplified diffusion model proposed here demonstrates that the key physics of

retention can be captured in a model with only a few free parameters. Isotope exchange experiments showed that the trapped concentrations play an important role in diffusion, and the displacement damage experiments showed how defect densities can increase the trapped concentration. Therefore the diffusion model for damaged materials takes advantage of these two conclusions. An analysis of the rate limiting factors of trapping and diffusion showed that the trapped concentration could indeed be treated as a diffusing species. After defining the trapping energies given by DFT literature, the only free (unknown) parameters are the defect densities, and we model the vacancy defect increase with ion damage. Using our control samples as the benchmark that defines the instrinsic defect densities, we see that high energy traps fill quickly, and that GB traps contain a very significant amount of the trapped D concentration. Then the retention of ion damaged samples can be predicted by only tuning the vacancy defect density given by SRIM computations. By having a more accurate prediction for the ion induced damage profile in W, the model would profide a fully predictive retention profile.

Finally, the culmination of the modeling and experimental work led to an extention of the diffusion model where a diffusion coefficient was derived to compare to measurements of H diffusivity, which vary wildly over a significant temperature range. The derived diffusion coefficient includes the defect densities and trapping energies, which we have learned are key in H diffusion. Discrepancies of H diffusion coefficients at temperatures lower than 1000 K seem to be explained by including trapping effects. By including the effects of ion damage, we see that diffusivity is further reduced at lower temperatures. Although retention is greatly enhanced, diffusion is greatly reduced. Therefore we now have a predictive framework to build upon and to extrapolate diffusivity values for next step fusion devices, but this work is far from complete.

8.2 Future experimental and modeling plans

The diffusion model was derived after observing the key physics driving the phenomena observed from experiments. Therefore future experiments will help identify other processes that need to be added to the model for predicting diffusion and retention in a more realistic fusion environment. Samples were damaged at room temperature in the above experiments, but we expect neutrons to irradiate PFCs operating at elevated temperature up to 1000 K or more. Experiments looking at ion damage irradiation in heated samples, where some damage may be annealed out, would illuminate the impact of damage at higher temperatures. Even more intriguing would be experiments with simultaneous irradation during plasma exposure, where the sample temperature is elevated due to plasma ion bombardment. This would then allow D implantation and trapping to compete with vacancy annealing, and as a result, could potentially reduce the annealing rate due to vacancy pinning by trapped D atoms. The latter experiment would then be modeled with a time dependent trap density. Temperature is presently considered constant in the model; however, divertor and first wall tiles can encounter transient heat fluxes due to instabilities in the plasma. Controlled transient heat experiments using an infrared laser to irradiate samples during plasma exposure have been done to examine surface morphology effects [110], but not retention. Examining retention after trasient heat loading would be an interesting experiment because we expect that diffusion will be enhanced at elevated temperatures, and this may affect retention not only on the surface but also in the bulk. In a D-T fusion environment, the He plasma species is a significant proportion of the plasma bombarding PFCs. Thus examining the He and D retention profiles with NRA adds another parameter to the diffusion problem. NRA retention profiles of W samples doped with He before D plasma exposure, samples exposed to He plasma mixed with D plasma,

samples exposed sequentially with He and D plasma, and samples exposed to pure ^{3}He plasma (with NRA in that case using a D ion beam) would expand our understanding of how He affects atomic diffusion. It has already been observed that He acts as a diffusion barrier to D [42], but little work has been done to expose all of the physical processes at play.

There are some additions to the model that can be treated directly. In order to model thermal desorption data, temperature needs to be treated as a function of time. The model would then be able to be benchmarked against TDS data, and allow modeling of surface fluxes after the plasma has been turned off. Boundary conditions can be modified to account for surface morphology changes so that the model can predict retention after higher temperature plasma exposures. Molecular dynamic simulations are planned to more accurately predict the vacancy defect densities in W. With this information, D retention predictions in samples having displacement damage will improve. A numerical calculation of the H diffusion coefficient as the trapped concentration increases can provide a novel calculation of the rate of change of diffusivity, which can then give more accurate predictions of D permiation in PFCs. All of these experimental and modeling plans show how rich this research topic is and its importance to fusion technology.

Bibliography

[1] Bp statistical review of world energy, Tech. rep., BP plc (2015).

[2] M. Kikuchi, K. Lackner, M. Q. Tran, Fusion Physics, International Atomic Energy Agency, 2012.

[3] J. D. Strachan, Fusion power production from tftr plasmas fueled with deuterium and tritium, Phys. Rev. Lett. 72 (1994) 3526.

[4] JET, Fusion energy production from a deuterium-tritium plasma in the jet tokamak, Nucl. Fusion 32 (1992) 187.

[5] J. Wesson, Tokamaks, 2nd Edition, Oxford Engineering Science Series No 48, Clarendon Press, Oxford, 1997.

[6] J. D. Lawson, Some criteria for a power producing thermonuclear reactor, Proc. Phys. Soc. B 70 (1957) 6–10.

[7] EUROfusion, www.euro-fusion.org.

[8] F. F. Chen, An Indespensable Truth, Springer, 2011, Ch. The Remarkable Tokamak, pp. 219–238.

[9] P. C. Stangeby, The Plasma Boundary of Magnetic Fusion Devices, Institute of Physics Publishing, 2000.

[10] ITER, www.iter.org.

[11] G. Federici, C. H. Skinner, J. N. Brooks, J. P. Coad, C. Grisolia, A. A. Haasz, A. Hassanein, V. Philipps, C. S. Pitcher, J. Roth, W. R. Wampler, D. G. Whyte, Plasma-material interactions in current tokamaks and their implications for next step fusion reactors, Nucl. Fusion 41 (12) (2001) 1967–2137.

[12] F. F. Chen, Introduction to plasma physics and controlled fusion, 2nd Edition, Vol. 1: Plasma Physics, Springer, 2006.

[13] B. LaBombard, J. E. Rice, A. E. Hubbard, J. W. Hughes, M. Greenwald, J. Irby, Y. Lin, B. Lipschultz, E. S. Marmar, C. S. Pitchera, N. Smick, S. M. Wolfe, S. J. Wukitch, Transport-driven scrape-off-layer flows and the boundary conditions imposed at the magnetic separatrix in a tokamak plasma, Nucl. Fusion 44 (2004) 1047–1066.

[14] W. J. Nuttall, Fusion as an energy source: Challenges and opportunities, Tech. rep., Institute of Physics (2008).

[15] E. Dechaumphai, J. L. Barton, J. R. Tesmer, J. Moona, Y. Q. Wang, G. R. Tynan, R. P. Doerner, R. Chen, Near-surface thermal characterization of plasma facing components using the 3-omega method, J. Nucl. Mater. 455 (2014) 56–60.

[16] M. J. Baldwin, R. P. Doerner, Helium induced nanoscopic morphology on tungsten under fusion relevant plasma conditions, Nucl. Fusion 48 (035001).

[17] B. D. Wirth, K. Nordlund, D. G. Whyte, D. Xu, MRS Bulletin 36.

[18] R. A. Causey, Hydrogen isotope retention and recycling in fusion reactor plasma-facing components, J. Nucl. Mater. 300 (2002) 91–117.

[19] W. Eckstein, C. Garcia-Rosales, J. Roth., W. Ottenberger, Sputtering data, rep. ipp 9/82, Tech. rep., Max-Planck-Institute fur Plasmaphysik (1993).

[20] D. Naujoks, J. Roth, K. Krieger, G. Lieder, M. Laux, Erosion and redeposition in the asdex upgrade divertor, J. Nucl. Mater. 210 (1994) 43–50.

[21] D. G. Whyte, R. Bastasz, J. N. Brooks, W. R. Wampler, W. P. West, C. P. C. Wong, O. I. Buzhinskij, I. V. Opimach, Divertor erosion in diii-d, J. Nucl. Mater. 266-269 (1999) 67–74.

[22] S. Carpentier-Chouchana, T. Hirai, F. Escourbiac, A. Durocher, A. Fedosov, L. Ferrand, M. Firdaouss, M. Kocan, A. S. Kukushkin, T. Jokinen, V. Komarov, M. Lehnen, M. Merola, R. Mitteau, R. A. Pitts, P. C. Stangeby, M. Sugihara, Status of the iter full-tungsten divertor shaping and heat load distribution analysis, Phys. Scr. T159 (014002).

[23] M. Rubel, J. P. Coad, N. Bekris, S. K. Erents, D. Hole, G. F. Matthews, R. D. Penzhorn, C. to EFDA-JET work programme, Beryllium and carbon films in jet following d-t operation, J. Nucl. Mater. 313-316 (2003) 321–326.

[24] K. Sugiyama, J. Roth, A. Anghel, C. Porosnicu, M. Baldwin, R. Doerner, K. Krieger, C. P. Lungu, Consequences of deuterium retention and release from be-containing mixed materials for iter tritium inventory control, J. Nucl. Mater. 415 (2011) S731–S734.

[25] Y. Ueda, J. W. Coenen, G. D. Temmerman, R. P. Doerner, J. Linke, V. Philipps, E. Tsitrone, Research status and issues of tungsten plasma facing materials for iter and beyond, Fusion Eng. Des. 89 (2014) 901–906.

[26] K. Tokunaga, M. J. Baldwin, R. P. Doerner, N. Noda, Y. Kubota, N. Yoshida, T. Sogabe, T. Kato, B. Schedler, Blister formation and deuterium retention on tungsten exposed to low energy and high flux deuterium plasma, J. Nucl. Mater. 337-339 (2005) 887–891.

[27] V. N. Chernikov, V. K. Alimov, A. V. Markin, A. P. Zakharov, Gas swelling and related phenomena in beryllium implanted with deuterium ions, J. Nucl. Mater. 228 (1996) 47–60.

[28] C. J. Altstetter, R. Behrisch, B. M. U. Scherzer, Trapping of deuterium implanted into stainless steel at low temperatures, J. Vac. Sci. Technol., A 15 (1978) 706–709.

[29] R. A. Pitts, S. Carpentier, F. Escourbiac, T. Hirai, V. Komarov, S. Lisgo, A. S. Kukushkin, A. Loarte, M. Merola, A. S. Naik, R. Mitteau, M. Sugihara, B. Bazylev, P. C. Stangeby, A full tungsten divertor for iter: Physics issues and design status, J. Nucl. Mater. 438 (2013) S48–S56.

[30] T. J. Petty, M. J. Baldwin, M. I. Hasan, R. P. Doerner, J. W. Bradley, Tungsten fuzz growth re-examined: the dependence on ion fluence in non-erosive and erosive helium plasma, Nucl. Fusion 55 (2015) 093033.

[31] Y. Ueda, H. Y. Peng, H. T. Lee, N. Ohno, S. Kajita, N. Yoshida, R. Doerner, G. D. Temmerman, V. Alimov, G. Wright, Helium effects on tungsten surface morphology and deuterium retention, J. Nucl. Mater. 442 (2013) S267–S272.

[32] R. P. Doerner, M. J. Baldwin, D. Nishijima, Plasma-induced morphology of beryllium targets exposed in pisces-b, J. Nucl. Mater. 455 (2014) 1–4.

[33] M. J. Baldwin, R. P. Doerner, D. Nishijima, K. Tokunaga, Y. Ueda, The effects of high fluence mixed-species (deuterium, helium, beryllium) plasma interactions with tungsten, J. Nucl. Mater. 390-391 (2009) 886–890.

[34] J. Roth, E. Tsitrone, T. Loarer, V. Philipps, S. Brezinsek, A. Loarte, G. F. Counsell, R. P. Doerner, K. Schmid, O. V. Ogorodnikova, R. A. Causey, Tritium inventory in iter plasma-facing materials and tritium removal procedures, Plasma Phys. Control. Fusion 50 (103001) (2008) 20.

[35] Y. L. Liu, Y. Zhang, H. B. Zhou, G. H. Lu, F. Liu, G. N. Luo, Vacancy trapping mechanism for hydrogen bubble formation in metal, Phys. Rev. B: Condens. Matter Mater. Phys. 79 (2009) 172103.

[36] W. Xiao, W. T. Geng, Role of grain boundary and dislocation loop in h blistering in w: A density functional theory assessment, J. Nucl. Mater. 430 (2012) 132–136.

[37] H. B. Zhou, Y. L. Liu, S. Jin, Y. Zhang, G. N. Luo, G. H. Lu, Investigating behaviours of hydrogen in a tungsten grain boundary by first principles: from dissolution and diffusion to a trapping mechanism, Nucl. Fusion 50 (2010) 025016.

[38] B. Lipschultz, J. Roth, J. W. Davis, R. P. Doerner, A. A. Haasz, A. Kalenbach, A. Kirschner, R. D. Kolasinski, A. Loarte, V. Philipps, K. Schmid, W. R. Wampler, G. M. Wright, D. G. Whyte, An assessment of the current data affecting tritium retention and its use to project towards t retention in iter, Tech. rep., Plasma Science and Fusion Center, MIT (2010).

[39] Y. Zayachuk, M. H. J. t Hoen, I. Uytdenhouwen, G. V. Oost, Thermal desorption spectroscopy of w-ta alloys exposed to high-flux deuterium plasma, Phys. Scr. T145 (014041).

[40] A. Moeslang, Development of a reference test matrix for ifmif test modules, final report on the efda task tw4-ttmi-003d4, Tech. rep., International Fusion Materials Irradiation Facility (2006).

[41] B. Tyburska-Puschel, V. K. Alimov, On the reduction of deuterium retention in damaged re-doped w, Nucl. Fusion 53 (123021).

[42] M. J. Baldwin, R. P. Doerner, W. R. Wampler, D. Nishijima, T. Lynch, M. Miyamoto, Effect of he on d retention in w exposed to low-energy, high-fluence (d, he, ar) mixture plasmas, Nucl. Fusion 51 (103021).

[43] P. Andrew, P. D. Brennan, J. P. Coad, J. Ehrenberg, M. Gadeberg, A. Gibson, D. L. Hillis, J. How, O. Jarvis, H. Jensen, R. Lasser, F. Marcus, R. Monk, P. Morgan, J. Orchard, A. Peacock, R. Pearce, M. Pick, A. Rossi, P. Schild, B. Schunke, D. Stork, Tritium retention and clean-up in jet, Fusion Eng. Des. 47 (1999) 233–245.

[44] C. K. Tsui, A. A. Haasz, J. W. Davis, J. P. Coad, J. Likonen, Deuterium removal during thermo-oxidation of be-containing codeposits from jet divertor tiles, Nucl. Fusion 48 (035008).

[45] R. Causey, K. Wilson, T. Venhaus, W. R. Wampler, Tritium retention in tungsten exposed to intense fluxes of 100 ev tritons, J. Nucl. Mater. 266-269 (1999) 467–471.

[46] C. Grisolia, A. Semerok, J. M. Weulersse, F. L. Guern, S. Fomichev, F. Brygo, P. Fichet, P. Y. Thro, P. Coad, N. Bekris, M. Stamp, S. Rosanvallon, G. Piazza, In-situ tokamak laser applications for detritiation and co-deposited layers studies, J. Nucl. Mater. 363-365 (2007) 1138–1147.

[47] C. H. Skinner, N. Bekris, J. P. Coad, C. A. Gentile, M. Glugla, Tritium removal from jet and tftr tiles by a scanning laser, J. Nucl. Mater. 313-316 (2003) 496–500.

[48] A. Widdowson, J. P. Coad, N. Bekris, G. Counsell, M. J. Forrest, K. J. Gibson, D. Hole, J. Likonen, W. Parsons, T. Renvall, M. Rubel, JET-EFDA, Efficacy of photon cleaning of jet divertor tiles, J. Nucl. Mater. 363-365 (2007) 341–345.

[49] V. K. Alimov, B. Tyburska-Püschel, M. H. J. tHoen, J. Roth, Y. Hatano, K. Isobe, M. Matsuyama, T. Yamanishi, Hydrogen isotope exchange in tungsten irradiated sequentially with low-energy deuterium and protium ions, Phys. Scr. T145 (2011) 014037.

[50] J. Roth, T. Schwarz-Selinger, V. K. Alimov, E. Markina, Hydrogen isotope exchange in tungsten: Discussion as removal method for tritium, J. Nucl. Mater. 432 (2013) 341–347.

[51] Materials assessment report g 74 ma 10 01-07-11 w, chapter 2.2 tungsten, Tech. rep., ITER Documentation (2001).

[52] J. C. Moreno-Marin, U. Conrad, H. M. Urbassek, Fractal structure of collision cascades, Nucl. Instrum. Methods Phys. Res., Sect. B 48 (1990) 404–407.

[53] T. D. de la Rubia, R. S. Averback, R. Benedek, W. E. King, Role of thermal spikes in energetic displacement cascades, Phys. Rev. Lett. 59 (17).

[54] T. D. de la Rubia, G. H. Gilmer, Structural transformations and defect production in ion implanted silicon: A molecular dynamics simulation study, Phys. Rev. Lett. 74 (13).

[55] K. Nordlund, J. Keinonen, M. Ghaly, R. S. Averback, Coherent displacement of atoms during ion irradiation, Nature 398 (1998) 49–51.

[56] Y. Nemoto, A. Hasegawa, M. Satou, K. Abe, Microstructural development of neutron irradiated w-re alloys, J. Nucl. Mater. 283-287 (2000) 1144–1147.

[57] V. Barabash, G. Federici, M. Rodig, L. L. Snead, C. H. Wu, Neutron irradiation effects on plasma facing materials, J. Nucl. Mater. 283-287 (2000) 138–146.

[58] V. Barabash, G. Federici, J. Linke, C. H. Wu, Material/plasma surface interaction issues following neutron damage, J. Nucl. Mater. 313-316 (2003) 42–51.

[59] Y. Hatano, M. Shimada, T. Otsuka, Y. Oya, V. K. Alimov, M. Hara, J. Shi, M. Kobayashi, T. Oda, G. Cao, K. Okuno, T. Tanaka, K. Sugiyama, J. Roth,

B. Tyburska-Puschel, J. Dorner, N. Yoshida, N. Futagami, H. Watanabe, M. Hatakeyama, H. Kurishita, M. Sokolov, Y. Katoh, Deuterium trapping at defects created with neutron and ion irradiations in tungsten, Nucl. Fusion 53 (2013) 073006.

[60] M. H. J. tHoen, B. Tyburska-Puschel, K. Ertl, M. Mayer, J. Rapp, A. W. Kleyn, P. A. Z. van Emmichoven, Saturation of deuterium retention in self-damaged tungsten exposed to high-flux plasmas, Nucl. Fusion 52 (2012) 023008.

[61] D. E. J. Armstrong, A. J. Wilkinson, S. G. Roberts, Mechanical properties of ion-implanted tungsten-5 wt

[62] Y. Oya, M. Shimada, M. Kobayashi, T. Oda, M. Hara, H. Watanabe, Y. Hatano, P. Calderoni, K. Okuno, Comparison of deuterium retention for ion-irradiated and neutron-irradiated tungsten, Phys. Scr. T145 (2011) 014050.

[63] W. R. Wampler, R. P. Doerner, The influence of displacement damage on deuterium retention in tungsten exposed to plasma, Nucl. Fusion 49 (2009) 115023.

[64] G. R. Tynan, Tritium breeding ratio greater than one imposes a severe retention constraint, private communication, 2016.

[65] G. F. Counsell, The plasma-wall interaction region: a key low temperature plasma for controlled fusion, Plasma Sources Sci. Technol. 11 (2002) A80–A85.

[66] Plansee, A-6600 Reutte, Austria, Tungsten: material properties and applications, www.plansee.com (2000).

[67] Nuclear fusion: Only the best survive!, PLANSEE Composite Materials GmbH, www.plansee.com (September 2012).

[68] M. T. Robinson, I. M. Torrens, Computer simulation of atomic-displacement cascades in solids in the binary-collision approximation, Phys. Rev. B: Condens. Matter Mater. Phys. 9 (1974) 5008–5024.

[69] J. F. Ziegler, J. P. Biersack, M. D. Ziegler, SRIM: The stopping and range of ions in matter, Lulu press, Co., 2008.

[70] Srim-2012, http://srim.org.

[71] Annual Book of ASTM Standards, vol. 12.02, American Society for Testing and Materials, Philadelphia, 1996, Ch. Standard Practice for Neutron Radiation Damage Simulation by Charge-Particle Irradiation, E521-96, p. 1.

[72] R. S. Averback, T. D. de la Rubia, Solid State Physics, Vol. 51, Elsevier, 1997, Ch. Displacement Damage in Irradiated Metals and Semiconductors, pp. 281–402.

[73] P. Ehrhart, K. H. Robrock, H. R. Schober, Physics of radiation effects in crystals, Vol. 13, North-Holland, 1986, Ch. Basic defects in metals, pp. 3–115.

[74] D. M. Goebel, G. Campbell, R. W. Conn, Plasma surface interaction experimental facility (pisces) for materials and edge physics studies, J. Nucl. Mater. 121 (1984) 277–282.

[75] E. M. Hollmann, A. Y. Pigarov, Measurement and modeling of molecular ion concentrations in a hydrogen reflex-arc discharge, Phys. Plasmas 9 (10) (2002) 4330–4339.

[76] G. R. Tynan, A. D. B. III, G. A. Campbell, R. Charatan, A. de Chambrier, G. Gibson, D. J. Hemker, K. Jones, A. Kuthi, C. Lee, T. Shoji, M. Wilcoxson, Characterization of an azimuthally symmetric helicon wave high density plasma source, J. Vac. Sci. Technol., A 15 (6) (1997) 2885–2892.

[77] Y. Wang, M. Nastasi (Eds.), Handbook of modern ion beam materials analysis, 2nd Edition, Materials Research Society, 2010.

[78] O. Benka, Surface and thin film Analysis: a compendium of principles, instrumentation, and applications, Wiley-VCH, 2002, Ch. Nuclear reaction analysis (NRA), pp. 170–176.

[79] H. R. Verma, Atomic and nuclear analytical methods: XRF, Mossbauer, XPS, NAA, and ion-beam spectroscopic techniques, Springer, 2007, Ch. Nuclear reaction analysis and particle-induced gamma-ray emission, pp. 269–293.

[80] V. K. Alimov, M. Mayer, J. Roth, Differential cross-section of the d(3he, p)4he nuclear reaction and depth profiling of deuterium up to large depths, Nucl. Instrum. Methods Phys. Res., Sect. B 234 (2005) 169–175.

[81] M. Mayer, E. Gauthier, K. Sugiyama, U. von Toussaint, Quantitative depth profiling of deuterium up to very large depths, Nucl. Instrum. Methods Phys. Res., Sect. B 267 (2009) 506–512.

[82] M. Mayer, Tech. rep. ipp 9/113, Tech. rep., IPP Garching (1997).

[83] P. A. Redhead, Thermal desorption of gases, Vacuum 12 (1962) 203–211.

[84] K. Tobita, S. Nishio, M. Enoeda, M. Sato, T. Isono, S. Sakurai, H. Nakamura, S. Sato, S. Suzuki, M. Ando, K. Ezato, T. Hayashi, T. Hayashi, T. Hirose,

T. Inoue, Y. Kawamura, N. Koizumi, Y. Kudo, R. Kurihara, T. Kuroda, M. Matsukawa, K. Mouri, Y. Nakamura, M. Nishi, Y. Nomoto, J. Ohmori, N. Oyama, K. Sakamoto, T. Suzuki, M. Takechi, H. Tanigawa, K. Tsuchiya, D. Tsuru, Design study of fusion demo plant at jaeri, Fusion Eng. Des. 81 (2006) 1151–1158.

[85] H. Bolt, V. Barabash, G. Federici, J. Linke, A. Loarte, J. Roth, K. Sato, Plasma facing and high heat flux materials - needs for iter and beyond, J. Nucl. Mater. 307-311 (2002) 43–52.

[86] K. Koizlik, J. Linke, H. Nickel, Neutron irradiation test matrix for carbon-based materials for the first wall of fusion reactors, J. Nucl. Mater. 179-181 (1991) 1100–1103.

[87] J. Sanz, R. de la Fuente, J. M. Perlado, Impact of the neutron flux on transmutation products at fusion reactor first-walls, J. Nucl. Mater. 155-157 (1988) 592–596.

[88] Y. Ueda, H. T. Lee, N. Ohno, S. Kajita, A. Kimura, R. Kasada, T. Nagasaka, Y. Hatano, A. Hasegawa, H. Kurishita, Y. Oya, Recent progress of tungsten r&d for fusion application in japan, Phys. Scr. T145 (2011) 014029.

[89] O. V. Ogorodnikova, B. Tyburska, V. K. Alimov, K. Ertl, The influence of radiation damage on the plasma-induced deuterium retention in self-implanted tungsten, J. Nucl. Mater. 415 (2011) S661–S666.

[90] W. R. Wampler, R. P. Doerner, Deuterium retention in tungsten from exposure to plasma, Phys. Scr. T138 (2009) 014037.

[91] J. Roth, K. Schmid, Hydrogen in tungsten as plasma-facing material, Phys. Scr. T145 (2011) 014031.

[92] V. K. Alimov, J. Roth, M. Mayer, Depth distribution of deuterium in single- and polycrystalline tungsten up to depths of several micrometers, J. Nucl. Mater. 337-339 (2005) 619–623.

[93] J. L. Barton, Y. Q. Wang, T. Schwarz-Selinger, R. P. Doerner, G. R. Tynan, Isotope exchange experiments in tungsten with sequential deuterium and protium plasmas in pisces, J. Nucl. Mater. 438 (2013) S1183–S1186.

[94] J. W. Mayer, E. Rimini, Ion Beam Handbook for Material Analysis, Academic Press, Inc., Pergamon, NY, 1978.

[95] M. Kobayashi, M. Shimada, Y. Hatano, T. Oda, B. Merrill, Y. Oya, K. Okuno, Deuterium trapping by irradiation damage in tungsten induced by different displacement processes, Fusion Eng. Des. 88 (2013) 1749–1752.

[96] G. R. Longhurst, TMAP7: Tritium Migration Analysis Program, Idaho National Laboratory, ineel/ext-04-02352, rev. 2 Edition (2008).

[97] J. L. Barton, Y. Q. Wang, T. Dittmar, R. P. Doerner, G. R. Tynan, Deuterium retention in tungsten after heavy ion damage and hydrogen isotope exchange in pisces, Nucl. Instrum. Methods Phys. Res., Sect. B 332 (2014) 275–279.

[98] B. L. Doyle, W. R. Wampler, D. K. Brice, S. T. Picraux, Saturation and isotopic replacement of deuterium in low-z materials, J. Nucl. Mater. 93-94 (1980) 551–557.

[99] R. Frauenfelder, Solution and diffusion of hydrogen in tungsten, J. Vac. Sci. Technol., A 6 (3) (1969) 388–397.

[100] M. Shimada, G. Cao, Y. Hatano, T. Oda, Y. Oya, M. Hara, P. Calderoni, The deuterium depth profile in neutron-irradiated tungsten exposed to plasma, Phys. Scr. T145 (2011) 014051.

[101] J. L. Barton, Y. Q. Wang, R. P. Doerner, G. R. Tynan, Development of an analytical diffusion model for modeling hydrogen isotope exchange, J. Nucl. Mater. 463 (2015) 1129–1133.

[102] H. Schultz, Atomic Defects in Metals, Vol. 25 of Landolt-Börnstein Database - Group III Condensed Matter, SpringerMaterials, 1991, Ch. W, section 2.2.3, doi: 10.1007/10011948 54.

[103] Midwest tungsten services, inc., private communication, 2016.

[104] K. Schmid, U. von Toussaint, Statistically sound evaluation of trace element depth profiles by ion beam analysis, Nucl. Instrum. Methods Phys. Res., Sect. B 281 (2012) 64–71.

[105] G. H. Vineyard, Frequency factors and isotope effects in solid state rate processes, J. Phys. Chem. Solids 3 (1957) 121–127.

[106] R. E. Stoller, Comprehensive Nuclear Materials, Vol. 1, Elsevier, 2012, Ch. Primary radiation damage formation, pp. 293–332.

[107] M. Shimada, G. Cao, T. Otsuka, M. Hara, M. Kobayashi, Y. Oya, Y. Hatano, Irradiation effect on deuterium behaviour in low-dose hfir neutron-irradiated tungsten, Nucl. Fusion 55 (2015) 013008.

[108] R. Bisson, S. Markelj, O. Mourey, F. Ghiorghiu, K. Achkasov, J.-M. Layet, P. Roubin, G. Cartry, C. Grisolia, T. Angot, Dynamic fuel retention in tokamak wall materials: An in situ laboratory study of deuterium release from polycrystalline tungsten at room temperature, J. Nucl. Mater. 467 (2015) 432–438.

[109] R. E. Stoller, M. B. Toloczko, G. S. Was, A. G. Certain, S. Dwaraknath, F. A. Garner, On the use of srim for computing radiation damage exposure, Nucl. Instrum. Methods Phys. Res., Sect. B 310 (2013) 75–80.

[110] J. H. Yu, R. P. Doerner, T. Dittmar, T. Höschen, T. Schwarz-Selinger, M. J. Baldwin, Iter-relevant transient heat loads on tungsten exposed to plasma and beryllium, Phys. Scr. T159 (014036).